

**High- $T_c$  Bi oxides by crystallization  
of an amorphous precursor**

by

**Pascal Tessier**

**Department of Physics, McGill University**

**Montréal, Québec**

**Canada**

**A Thesis submitted to the  
Faculty of Graduate Studies and Research  
in partial fulfillment of the requirements for the degree of  
Master of Science**

**© Pascal Tessier, 1991**

To the memory of Emilienne and Adéline.

## Acknowledgements

I thank Professor John O. Strom-Olsen who has guided and encouraged me since I first came to his office as an undecided first year graduate student. I also thank Robert Schulz who took the risk to have me working in his laboratory and who communicated to me part of his great enthusiasm.

I also thank all the people at McGill University: Leszek Zaluski, Professor Zavin Altounian, Diane Koziol, Eugenia Corvera, Martin Lacasse and all the others. I thank the people at the Institut de Recherche d'Hydro-Québec: Michel Trudeau who has been very helpful, François Lavallée who inspired me with his courage, the skilled technicians René Dubuc, Reynald Rioux, and Alain Joly, and Julian Cave for his help concerning magnetic characterization, and all those I forget.

I thank all the professors who, in the past, interested me in studying, some of them in the physics department at the Université de Montréal.

I have been supported during my master by the Fonds FCAR (Government of Québec) who provided me with a scholarship and by the National Science and Engineering Research Council of Canada. Some support has also come from McGill University and Hydro-Québec.

Finally, I wish to thank those in my family who encouraged and supported me, especially my parents, who struggled through life to make this place a better world, by their work and by the work of those they cherish.

## Abstract

The amorphization of the Bi-Sr-Ca-Cu-O system by mechanical alloying starting from the individual oxides is examined. Several reactions concur to finally yield an amorphous matrix containing nanocrystalline copper oxide precipitates. Annealing the amorphous material leads, in a first step, to a crystalline solid solution, and, in a second step, to a low-T<sub>c</sub> superconducting phase. Long term annealing allows the formation of the 85K superconducting phase.

## Sommaire

Le broyage des oxydes individuels du système Bi-Sr-Ca-Cu-O est analysé dans le présent mémoire. Plusieurs réactions concourent à former une phase amorphe contenant des précipités nanométriques d'oxyde de cuivre. Lors de recuits subséquents, ce matériau amorphe se transforme d'abord en une solution solide cristalline, puis en la phase supraconductrice à basse température. Un recuit prolongé permet ensuite de former la phase supraconductrice à 85K.

## Table of Contents.

Acknowledgements.	111
Abstract.	1V
Sommaire.	v
Table of contents.	v1
List of figures.	1x
List of tables.	xi
Chapter 1.	
Introduction.	1
Chapter 2.	
A brief survey of superconductivity.	4
2.1. Conventional superconductors.	4
2.2. The phenomenon of superconductivity.	4
2.3. Critical field.	5
2.4. The London equations.	6
2.5. Pippard's coherence length.	7
2.6. The BCS theory.	8
2.7. The Ginzburg-Landau theory.	9
2.8. Type I and Type II superconductors.	10
2.9. Critical currents and flux pinning.	12
2.10. General structures of the high-T <sub>c</sub> superconducting oxides.	13
2.11. The problems involved with the new materials.	13
Chapter 3.	
The B <sub>1</sub> -Sr-Ca-Cu-O series of high-T <sub>c</sub> superconductors.	18
3.1. The different bismuth-based superconducting phases.	18
3.2. The structure of the bismuth compounds.	19

3.3. Bismuth oxides made by the technique of rapid solidification. 22

Chapter 4.

Amorphization by ball milling. 26

4.1. The historical development. 26

4.2. The process of ball milling. 27

4.3. The thermodynamics of the process. 29

4.4. The glass-forming range. 34

4.5. An analysis of the physics of ball milling. 35

4.6. The question of the temperature. 35

4.7. Ball milling of high-T<sub>c</sub> superconducting systems. 36

Chapter 5.

Experimental method. 38

5.1. Experimental procedure used. 38

5.2. DSC measurements. 40

5.3. TGA measurements. 41

5.4. Procedure for thermal treatments, 43

5.5. X-ray diffractometry. 43

5.5.1. Instrument. 43

5.5.2. Measurement of the crystallite size. 44

5.6. Magnetic measurements. 45

5.7. Transmission electron microscopy (TEM). 45

5.8. Scanning electron microscopy (SEM). 47

5.9. Contamination of strontium oxide. 47

Chapter 6.	
Results and discussion.	48
6.1. Amorphization by ball milling.	48
6.2. Thermal treatments.	62
6.2.1. Annealing in argon.	62
6.2.2. Annealing in oxygen.	73
6.2.3. High-Tc phase formation.	76
6.3. Comparison with materials prepared by rapid solidification.	76
Chapter 7.	
Conclusion.	79
Appendix.	81
Bibliography.	105

## List of Figures.

2-1. Critical field versus temperature.	6
2-2. Type I superconductors in a magnetic field.	10
2-3. $\text{La}_2\text{CuO}_4$ .	14
2-4. $\text{Tl}_2\text{Ba}_2\text{Ca}_2\text{Cu}_3\text{O}_{10}$	14
3-1. Idealized representation of the structure of superconducting phases in the Bi-Sr-Ca-Cu-O system.	20
3-2. Unit cell of the 2201 phase.	21
4-1. X-ray diffraction patterns of $\text{NiZr}_2$ as a function of milling time.	30-31
4-2. The mixing of two components.	32
4-3. Free energy diagram.	33
5-1. Motion of the vial in the SPEX 8000 mixer/mill.	39
5-2. Differential scanning calorimeter.	41
5-3. Thermogravimetric analyser.	42
5-4. SQUID magnetometer.	46
6-1. Scanning micrographs of powder milled 1 hour.	49
6-2. Scanning micrographs of powder milled 3 hours.	52
6-3. X-ray diffraction patterns of ball-milled samples.	54-55
6-4. X-ray patterns of $\text{Bi}_2\text{O}_3+2\text{CaO}$ for various milling times.	58
6-5. X-ray pattern of $(\text{Bi}_2\text{O}_3+2\text{CaO})+2\text{SrO}$ milled 20 hours.	59
6-6. X-ray patterns of the milled mixture: bcc solid solution $(\text{Bi-Ca-O}) + \text{CuO}$ .	60
6-7. TEM picture of a sample milled 90 hours.	61
6-8. DSC scan of a sample milled 48 hours.	63
6-9. TGA scan of a sample milled 48 hours.	63
6-10. DSC scan of a sample annealed 1 hour at 700K in argon.	64
6-11. TGA scan of a sample annealed 1 hour at 700K in argon.	64
6-12. Kissinger plot for the second transformation.	65

6-13. X-ray diffraction pattern of a sample heated to 800K in argon at 20K/min.	66
6-14. X-ray diffraction pattern of a sample heated to 1000K in argon at 20K/min.	66
6-15. DSC scan of the $\text{Bi}_2\text{O}_3+2\text{CaO}$ sample milled 20 hours.	67
6-16. Kissinger plot for the second transformation in the $\text{Bi-Ca-O}$ subsystem.	68
6-17. X-ray diffraction pattern of $\text{Bi}_2\text{O}_3+2\text{CaO}$ milled 20 hours and of samples subsequently heated to 800 and 1000K in argon at 20K/min.	69
6-18. X-ray pattern of $\text{Bi-Ca-Cu-O}$ milled 20 hours and heated to 800K at 20K/min in argon.	70
6-19. X-ray pattern of $\text{Bi-Sr-Ca-O}$ milled 20 hours and heated to 700K at 20K/min in argon.	70
6-20. DSC scan, in oxygen at 20K/min, of a sample milled 48 hours.	74
6-21. X-ray patterns of samples treated in an oxygen atmosphere.	75
6-22. Diffraction pattern of the 85K (2212) phase.	77
6-23. Magnetization curve of a superconducting sample.	77
6-24. Magnetization curve of a superconducting sample.	78

## List of Tables.

3-1. Composition of the superconducting phases in the Bi-Sr-Ca-Cu-O system.	18
5-1. Powders used in milling experiments.	38
6-1. Size and chemical composition of the large agglomerated particles after 1 hour of milling.	50
6-2. Composition and size of the smaller particles after 1 hour of milling.	51
6-3. Enthalpies of formation and melting points of the metallic oxides.	53
6-4. Crystallite size of copper oxide during milling.	56
6-5. X-ray peak intensities and lattice parameters for the bcc solid solution formed in various samples.	71
Appendix	
1. Space groups and lattice parameters.	82
2. Density.	82
3. Atom locations.	83
4. Diffraction data for the 2201 phase.	84
5. Diffraction data for the 2212 phase.	85
6. Diffraction data for the 2223 phase.	86
Summary of rapid solidification studies.	
7. Composition, techniques, and resulting amorphous samples.	88
8. Thermal analysis.	90
9. Resistivity measurements.	92
10. Diffraction data for a sample milled 48 hours and heated to 800K at 20K/min in argon.	94
11. Diffraction data for a sample milled 48 hours and heated to 1000K at 20K/min in argon.	95

12. Diffraction data for a sample milled 48 hours and heated to 800K at 20K/min in oxygen. 97
13. Diffraction data for a sample milled 48 hours and heated to 1000K at 20K/min in oxygen. 98
14. Diffraction data for a sample milled 48 hours and annealed 20 hours at 1125K in oxygen. 101
15. Calculated X-ray intensities from a bcc structure for various chemical compositions. 104

## Chapter 1

### Introduction.

The discovery of superconducting materials based on oxides of combined rare earths and copper in 1986-1987 [5,83] caused renewed interest in the field of superconductivity. The obstacle of low critical temperatures (30K) having been cleared, the possibility of using superconductors at the temperature of liquid nitrogen has triggered an unprecedented research effort by scientists around the world.

Such work has rapidly given results in few years. New superconducting oxides have been discovered with higher critical temperatures. Optimal treatments have been determined for many synthesis processes. The steps of formation for the different materials are better understood. Research groups in the industry are already looking for improvement of transport critical currents.

Critical currents in the new superconducting materials are limited by many factors. Although granularity is detrimental to critical currents, it may be necessary if one wants to have flexible superconducting wires. Insufficient pinning of magnetic flux lines and poor alignment of grains are problems that have to be addressed.

Directional solidification using a temperature gradient is an efficient method for the fabrication of superconducting wires with a high degree of texture (alignment of grains). Another method to get a strong alignment of the crystalline grains is to start from an amorphous mixture of the constituent elements of a superconducting oxide and try to control the crystallization, for example through the introduction of crystalline seeds in the amorphous matrix. Various methods of rapid solidification

have been tried by many groups. All these methods produce large quantities but usually in the form of flakes or small lengths of wires. There is also the problem of chemical control due to the vaporization of some chemical elements.

One process that avoids some of these problems is high energy ball milling, a process in which a certain quantity of powder is submitted to shocks caused by collisions between steel balls moving rapidly in a steel container placed in a vibrating or rotating frame. Ball milling has already been successfully used to produce amorphous alloys of transition metals. Therefore it was natural to use ball milling for the preparation of amorphous precursors to superconducting oxides.

This work is the first known detailed report on the use of ball milling in the case of the bismuth-based superconducting oxides. Similar work has been carried out recently by F. Lavallée [37] for the Y-Ba-Cu-O compound. We will describe the structural transformations taking place during the milling processes. Calorimetric measurements and systematic X-ray diffractometry will provide us with information about the crystallization of the amorphous phase and the kinetics of the reactions. Transmission electron microscopy will give us complementary information to be used for phase identification and morphological observations. Furthermore, magnetic measurements will assess the quality of the resulting superconducting samples. No final conclusions shall be derived from the results thus obtained since this study does not include the search for optimal thermal treatments. Our purpose here is mainly to investigate the feasibility of the synthesis method and to give a description of the phase transformations during its application.

The next chapter will be devoted to the review of superconductivity. Since superconductivity has been reviewed by many authors and discussed

in many books and articles we will not give a full introduction to the subject but rather a brief account of the important results.

The third chapter is a description of the Bi-Sr-Ca-Cu-O system and a review of previous work. The process of ball milling used to make amorphous materials will be discussed in the fourth chapter. This part will probably be the most unfamiliar to the reader and so receives a careful treatment.

Finally the experimental procedure will be detailed in chapter 5 and the results presented and discussed in chapter 6. The appendix at the end gives a mass of important numerical data including X-ray diffraction standards for the superconducting phases, a detailed review of experimental data from previous work in rapidly-quenched Bi-based materials, and some of the diffraction data gathered during our experiments.

## Chapter 2

### A Brief Survey of Superconductivity.

#### 2.1. Conventional Superconductors.

A Dutch physicist, Kamerlingh Onnes [31], first discovered superconductivity in mercury in 1911. At a critical temperature of 4.2K he observed that the electrical resistivity vanished. Since then, many elements have been found to be superconductors but all at temperatures below 10K. Many alloys and intermetallic compounds turned out to be superconductors as well, and some have critical temperatures above 10K. The highest  $T_c$  prior to 1986 (23K) was found in  $Nb_3Ge$  doped with oxygen impurities [53]. Then, at the end of 1986, Bednorz and Muller announced [5] the discovery of superconductivity at 30K in  $La(Ba)-Cu-O$ . This progress was shortly followed by that of  $Y-Ba-Cu-O$  [83] in 1987.

In 1987, Michel et al. [48] found a new superconducting oxide in the  $Bi-Sr-Cu-O$  system with a maximum  $T_c$  of 22K (hereafter referred to as the 10K phase). Then, in January 1988, Maeda et al. [41] reported that the addition of calcium produces two high- $T_c$  phases with onsets at 83K and 105K (the 85 and 110K phases). It was found later [23] that the addition of lead increases the amount of the 110K phase sufficiently for the sample to show zero resistivity at 107K.

Before discussing these novel materials it is important to discuss what was known about conventional superconductors before 1986.

#### 2.2. The Phenomenon of Superconductivity.

One of the two most striking properties of superconductors is the

fact that below the critical temperature there is no electrical resistance. Such a property allows one to excite a current in a superconducting loop that will persist forever. An experiment [16] has determined that the decay time of supercurrents was not less than 100 000 years. Magnetic fields of 10T can be achieved with an initial power input to a superconducting coil and maintained as long as one can provide liquid helium, whereas a magnet made of copper coils may require 2 megawatts or more of continuous power to produce the same field [75].

The other interesting property is that, in the superconducting state, the material is perfectly diamagnetic. The effect was reported by Meissner and Ochsenfeld [47] in 1933 but is now simply called "the Meissner effect". It allows a magnet to be levitated above a superconductor, thus giving the possibility of developing frictionless transport devices.

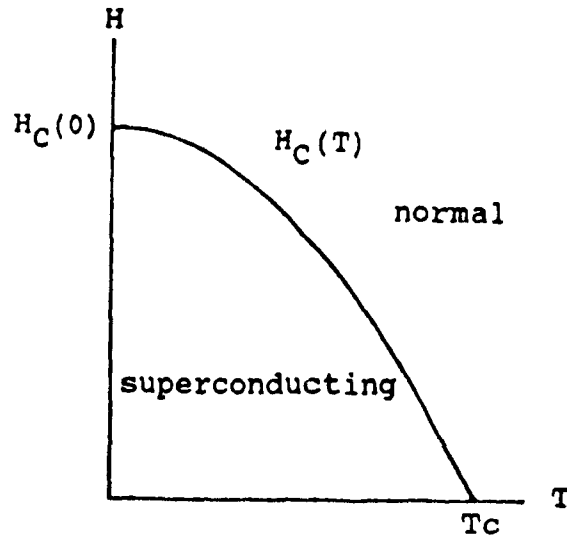
### 2.3. Critical Field.

A sufficiently strong magnetic field destroys superconductivity. This critical field may be expressed as a function of the difference in free energy between the normal and superconducting states:

$$\frac{\mu_0 [H_C(T)]^2}{2} = f_N(T) - f_S(T) \quad (2-1)$$

The condensation energy of the superconducting state will vary as a function of temperature, hence  $H_C$  will also vary as shown on the next figure.

Figure 2-1. Critical field versus temperature.



#### 2.4. The London equations.

The London equations describe the electromagnetic properties of superconductors:

$$\mathbf{E} = \frac{\partial}{\partial t} (\Lambda \mathbf{J}_S) \quad (2-2)$$

$$\mathbf{B} = -\text{rot}(\Lambda \mathbf{J}_S) \quad (2-3)$$

where  $\Lambda = \mu_0 \lambda_L^2$  or  $\Lambda = m / (n_S e^2)$ .

$n_S$  is the density of superconducting electrons and  $\lambda_L$  is the penetration depth, a typical distance over which the field penetrates at the surface of a sample. Equation 2-3 leads to an exponential decrease of the field from the surface to the interior of the superconductor:

$$\text{rot}(\text{rot}(\mathbf{B})) = \mathbf{B}/\lambda_L^2 \quad (2-4).$$

## 2.5. Pippard's Coherence Length.

Ohm's law for normal metals may be expressed in a nonlocal form [93]:

$$\mathbf{J}(\mathbf{r}) = \frac{3\sigma}{4\pi} \int \frac{\mathbf{R}[\mathbf{R} \cdot \mathbf{E}(\mathbf{r}')] e^{-R/l}}{R^4} d\mathbf{r}' \quad (2-5)$$

$$(\mathbf{R} = \mathbf{r} - \mathbf{r}'),$$

where the current depends on the field over a finite region in the vicinity of the point considered.  $l$ , the mean free path of the electron, is the characteristic size of that region.

Pippard found a similar modification to the London equation for superconductors:

$$\mathbf{J}_S(\mathbf{r}) = \frac{-3}{4\pi \xi_0 \Lambda} \int \frac{\mathbf{R}[\mathbf{R} \cdot \mathbf{A}(\mathbf{r}')] e^{-R/\xi}}{R^4} d\mathbf{r}' \quad (2-6)$$

where  $\xi$ , the coherence length in the presence of scattering is related to that of the pure material  $\xi_0$  by the relation

$$\frac{1}{\xi} = \frac{1}{\xi_0} + \frac{1}{l} \quad (2-7).$$

$\xi_0$  may be deduced by applying Heisenberg's uncertainty principle and knowing that the electrons involved in superconductivity occupy a range

within  $kT_C$  of the Fermi level. We obtain the following expression:

$$\xi_0 = a \frac{\hbar v_f}{k T_C} \quad (2-8),$$

where  $a$  is a constant to be determined.

## 2.6. The BCS Theory.

The simplest theory of superconductivity was presented by Bardeen, Cooper, and Schrieffer in 1957 [3]. It has first been shown by Cooper [12] that a weak attraction can lead to the formation of bound pairs of electrons, the so-called Cooper pairs. Frohlich had already suggested the importance of the electron-lattice interaction [17] in mediating this attraction. It is the phonon-mediated part of the interaction between the electrons that gives rise to the pairing in conventional superconductors. When the electrons are bound in pairs, they behave coherently and such a coherence leads to the well known effects under the influence of an electromagnetic field. Confirmation of the role of phonons came from experiments verifying the isotope effect. This effect occurs when an element is substituted by one of its isotopes (which has a different mass). Since the frequency of phonons depends on the mass of the atoms, the  $T_C$  of a system where superconductivity arises from the electron-phonon interaction is expected to be changed by such a substitution.

In the BCS theory, the origin of the interaction is not considered, rather an idealized pairing interaction is proposed. An important parameter in the BCS theory is the energy gap:

$$\Delta(T=0) = 1,764 k_B T_C \quad (2-9).$$

This gap is the minimum energy necessary to break a pair of electrons. Its existence leads to a characteristic exponential temperature dependence in the electronic specific heat of conventional superconductors.

We have now defined the basic ideas we will need in the following discussion of critical currents. The reader will find a detailed discussion of the BCS theory in the book by Tinkham [75] from which much of this chapter is taken. We will now discuss the phenomenological Ginzburg-Landau theory.

### 2.7. The Ginzburg-Landau Theory.

Ginzburg and Landau [20] have introduced a pseudowave function representing the local density of superconducting electrons. They derived phenomenologically the Ginzburg-Landau equations describing the behavior of this wave function in a magnetic field

$$\alpha \psi + \beta |\psi|^2 \psi + \frac{1}{2m^*} \left( -\frac{\hbar}{i} \nabla - e^* \mathbf{A} \right)^2 \psi = 0 \quad (2-10).$$

The electric current is related to the field and the wave function by:

$$\mathbf{J} = \frac{e^* \hbar}{2m^* i} (\psi^* \nabla \psi - \psi \nabla \psi^*) - \frac{e^{*2}}{m^*} \psi^* \psi \mathbf{A} \quad (2-11),$$

where  $e^* = 2e$  and  $m^* = 2m_e$ . The characteristic length over which  $\psi$  varies is:

$$\xi^2(T) = \frac{\hbar^2}{2m^* |\alpha(T)|} \quad (2-12).$$

In a pure superconductor far from  $T_c$  this Ginzburg-Landau coherence length

is roughly equal to Pippard's coherence length  $\xi_0$ . Close to  $T_c$ ,  $\xi(T)$  diverges as  $(T_c - T)^{-1/2}$ . An important parameter of this theory is the ratio

$$\kappa = \lambda / \xi \propto \beta^{1/2} \quad (2-13)$$

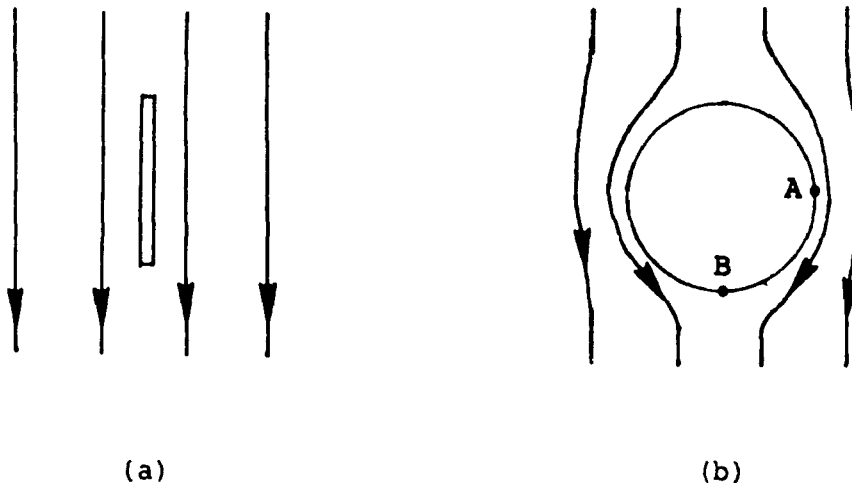
where  $\lambda$  is the penetration depth discussed previously. This ratio, which is independent of the temperature, will determine whether the superconductor is of Type I or Type II, these categories will be defined in the next section.

### 2.8. Type I and Type II Superconductors.

The Ginzburg-Landau theory allows to calculate the energy associated with the interface between a superconducting and a normal region within a superconductor. Two possibilities arise: the surface energy may be negative or positive.

We analyze what happens when the surface energy is positive. Figure 2-2 below shows two samples submitted to a magnetic field.

Figure 2-2. Type I superconductors in a magnetic field.



In (a) there is a thin sample parallel to the applied field. If we increase the field above the thermodynamic critical field the sample becomes normal. The situation is different in the case of a bulk sample like the spherical one shown in (b). The distortion in the field introduced by the presence of the perfectly diamagnetic sample makes the field at point A greater than that at point B. Therefore as we increase the applied field, a point is reached where the field at point B is equal to the critical field. If we increase the applied field a bit further, some parts of the superconductor will turn normal, this is called the intermediate state. Since the interface energy between the superconducting and normal domains is positive, there cannot be an arbitrary amount of normal regions in the sample, rather a compromise will exist between the total free energy and the energy of the interfaces.

If the interface energy is negative, the problem is totally different. The minimization of energy would require a large number of small normal regions about the size of the coherence length. However another condition will dictate the form of that "mixed" state: the continuity of the Ginzburg-Landau wave function. This condition leads to the fact that the flux threading a closed loop inside a Type II superconductor can vary only by discrete steps of value

$$\Phi_0 = h/(2e) \quad (2-14),$$

this quantity is called the fluxoid. Above a lower critical field  $H_{c1}$  the sample is threaded by flux vortices or flux lines. The number of flux lines increases as the field increases, until an upper critical field  $H_{c2}$  is reached. At this point the sample is saturated. The addition of flux lines making the distance between them shorter than the coherence length

would raise the free energy above that of the normal state and consequently superconductivity is destroyed. If the sample is free from impurities and defects the flux lines will form an hexagonal lattice.

The Ginzburg-Landau theory gives a criterion to differentiate Type I from Type II:

$$\text{Type I:} \quad K < 1/\sqrt{2} \quad (2-15a)$$

$$\text{Type II:} \quad K > 1/\sqrt{2} \quad (2-15b).$$

The high- $T_c$  superconductors are of Type II. This justifies our description of the magnetic properties of Type II superconductors. Since our final objective is to make superconductors to carry high currents, we shall now describe the properties of Type II superconductors carrying electrical currents.

## 2.9. Critical Currents and Flux Pinning.

A current passing through a superconductor will create a magnetic field and therefore for a certain value, called the critical current, the wire will become normal and a resistance will appear. In a Type II superconducting wire the situation is more complicated than in Type I materials. If a Type II superconducting wire operates in a strong magnetic field (this is the case of most interesting applications), the wire will be penetrated by flux lines, these flux lines will interact with the electric field and will tend to move. Such a movement will cause energy dissipation. In order to have true zero resistance wires, the flux lines must be prevented from moving. In common terms the flux lines must be pinned. Such a pinning may be achieved through the addition of structural defects or impurities. Such inhomogeneities may act as potential wells for

flux lines and so pin them.

Such difficulties have been dealt with in conventional Type II materials. Weak pinning is one of several problems encountered in the new superconducting oxides. We shall discuss these.

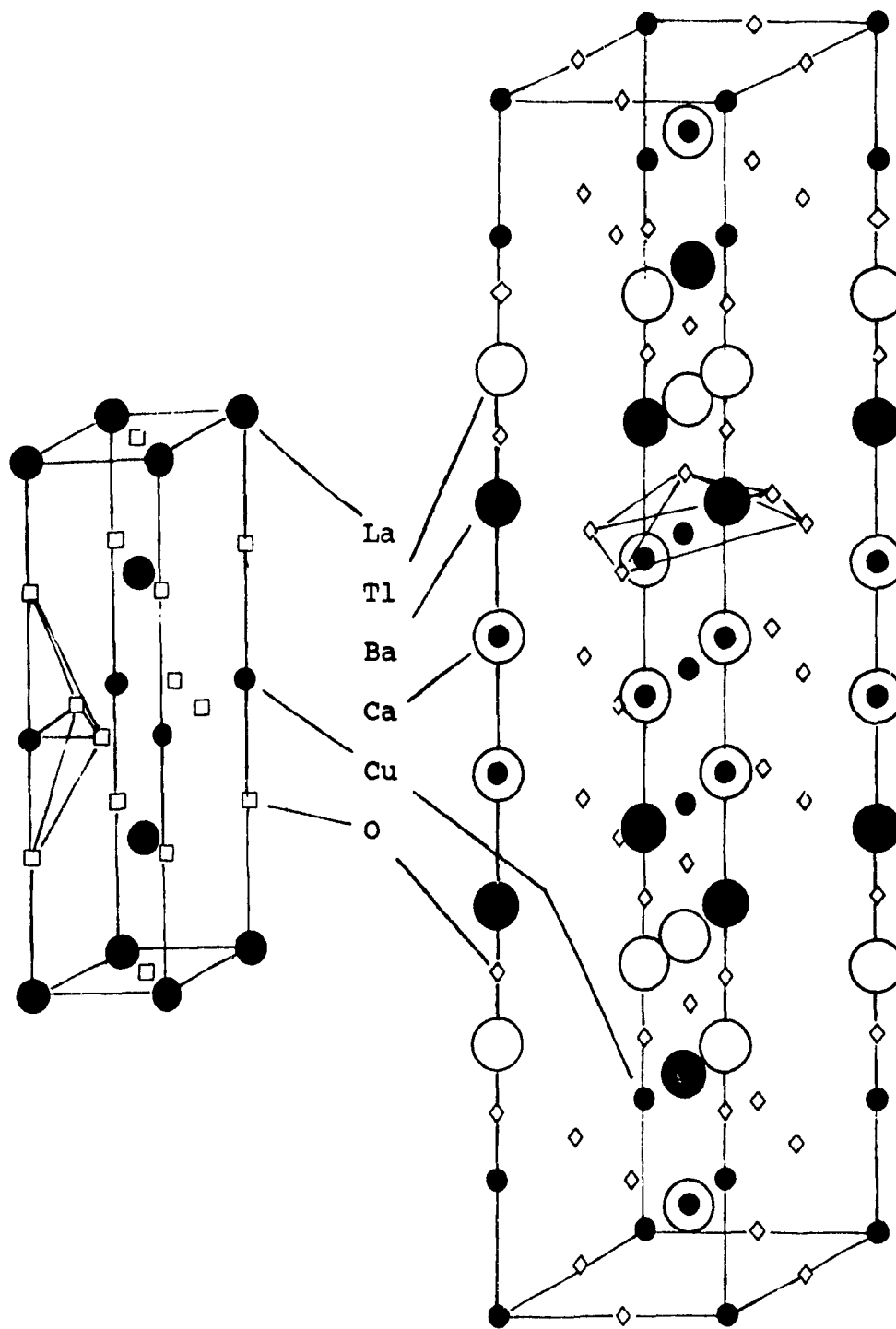
#### 2.10. General Structure of High-Tc Superconducting Oxides.

All high temperature superconducting oxides have a similar structure. The common characteristic is an octahedron with oxygen atoms at the angles and a copper atom at the center (the so-called perovskite block). These perovskite blocks are sandwiched between one or more layers of rare earths or metallic elements with additional oxygen atoms. Figure 2-3 below shows the simplest structure:  $\text{La}_2\text{CuO}_4$  (lanthanum has to be partially substituted by barium, calcium or strontium for the material to be superconducting) and figure 2-4 shows  $\text{Tl}_2\text{Ba}_2\text{Ca}_2\text{Cu}_3\text{O}_{10}$  ( $T_c=125\text{K}$ ). It is believed that the copper oxide planes are responsible for the interaction giving rise to superconductivity because they are a common feature of the structures.

#### 2.11. The Problems Involved with the New Materials.

The most serious difficulty with high temperature superconducting oxides is that the materials are extremely brittle. Conventional sintering techniques yield polycrystalline materials which have much lower critical currents than what is found in thin films or single crystals.

A polycrystalline ceramic material is likely to be porous and this lowers the volume available for electrical transport in the material. The polycrystalline materials produced are granular and this has an effect on superconductivity. In conventional superconductors the coherence length

Figure 2-3.  $\text{La}_2\text{CuO}_4$ .Figure 2-4.  $\text{Tl}_2\text{Ba}_2\text{Ca}_2\text{Cu}_3\text{O}_{10}$ 

is much larger than the thickness of grain boundaries, but in high-Tc superconductors, the coherence length is of the order of a few interatomic distances (about 1nm). The supercurrents pass from one grain to another through regions of non-superconducting material called weak links. Electrons pass through these weak links by tunneling, but the critical current of the weak links is less than the critical current of the crystallites. This problem of weak links is partly due to the bad physical connectivity between the grains of these very brittle materials. Also it seems that compositional variations occur at grain boundaries [29]. Since high-Tc superconductors are particularly sensitive to stoichiometry [58], it increases the problems of weak links. They are also especially sensitive to oxygen content [55] probably because of the crucial equilibrium between oxidation states of the metallic atoms which is believed to be at the origin of the phenomenon of high-Tc superconductivity (the reader is referred to the discussion by Robert J. Cava [8]). The thermal treatment used in synthesis is therefore of paramount importance.

The structural and superconducting properties of high-Tc oxides are highly anisotropic. For example, the critical current of Y-Ba-Cu-O single crystals at 4.5K is  $3,2 \times 10^6 \text{A/cm}^2$  in the ab-plane but only  $1,6 \times 10^5 \text{A/cm}^2$  along the c-axis [82]. In normal polycrystalline material the crystallites are randomly oriented. Because of this random orientation, the critical current is further reduced from its potentially maximum value it has normal to the c-axis, since current will have to pass in the direction of the c-axis in certain grains. Another difficulty is that flux pinning is very poor in these materials. In the first years critical currents in bulk samples were in the range  $100\text{-}1000 \text{A/cm}^2$  and were very field dependent, falling to zero by about 1T, whereas in single crystals the  $J_c$  could be as high as  $10^6 \text{A/cm}^2$ .

In order to achieve higher critical currents, one has to obtain a dense structure, to align crystalline grains along the ab-plane (have a textured material), and to improve connectivity between grains through proper thermal treatment and impurity control.

Certain methods have been attempted to achieve these goals. Jin et al. [30] achieved a current density of  $7400\text{A}/\text{cm}^2$  at 77K and 0T and  $1000\text{A}/\text{cm}^2$  at 1T, by making samples using melt-textured growth, a process in which a melted composition is solidified in a temperature gradient. Grains tend to grow with the c-axis normal to the gradient. Using the same process, Hitachi [27], in Japan, made thallium-based superconducting tapes with a  $J_c$  in excess of  $10^4\text{A}/\text{cm}^2$  at 77K and 0T.

An alternate approach is to start from the amorphous state, rather than the liquid state, and try to crystallize the sample in such a way that grains are aligned in a specific direction. Crystallization of an amorphous phase can produce a quite different microstructure than the one obtained by conventional cooling from a melted material. Rapid solidification (the usual method for making amorphous materials) has in fact been applied to Y-Ba-Cu-O but it was found that the quenched samples were always partially crystalline [46]. An alternative approach for making the amorphous phase, high-energy ball milling, was recently used by Lavallée [37] on the above system but he too was unable to achieve complete amorphization. Some crystalline peaks are still present after 96 hours of milling in a SPEX 8000 mixer/mill. Nevertheless, his material was superconducting after proper thermal treatment. Completely amorphous materials have been obtained in the Bi-Sr-Ca-Cu-O system with rapid solidification but the  $J_c$  values are not yet as high as those reached by melt-textured growth processes.

The purpose of this work was to apply the method of ball milling to

the Bi-Sr-Ca-Cu-O system to make an amorphous precursor, and then crystallize the system into the high-T<sub>c</sub> phase. Once this is realized, it may be possible in the future to control crystallization in order to obtain a textured material.

In the next chapter we will review the results of rapid solidification on the bismuth compounds. This will provide us with an opportunity to compare our results obtained by high-energy ball milling.

## Chapter 3

## The Bi-Sr-Ca-Cu-O Series of High-Tc Superconductors.

## 3.1. The Different Bismuth-based Superconducting Phases.

It is now established that the ratios of the elements in the three known superconducting phases are:

Table 3-1. Composition of the superconducting phases in the Bi-Sr-Ca-Cu-O system.

Bi	Sr	Ca	Cu	O	Tc(K)
2	2	0	1	6	10
2	2	1	2	8	85
2	2	2	3	10	110.

The ratio for strontium in the 10K phase is only approximative, it is in fact somewhat lower than the ideal number given above. There exists a phase with exact 2:2:0:1 composition [57] but it has a slightly different structure. Moreover, in the 85K phase, bismuth has been found on calcium sites [71]. In this study however, the different phases shall be identified by the coefficients given above. For example the 10K phase will be called the 2201 phase. The critical temperatures given are not carefully determined values but rather those generally used in the nomenclature. Critical temperatures may also vary greatly depending on the thermal treatment and oxygen pressure used during synthesis.

An excellent analysis of the various structural models has been

carried out by Matheis and Snyder [43]. They determined and optimized the best models and we shall use these as standards.

### 3.2. The Structure of the Bismuth Compounds.

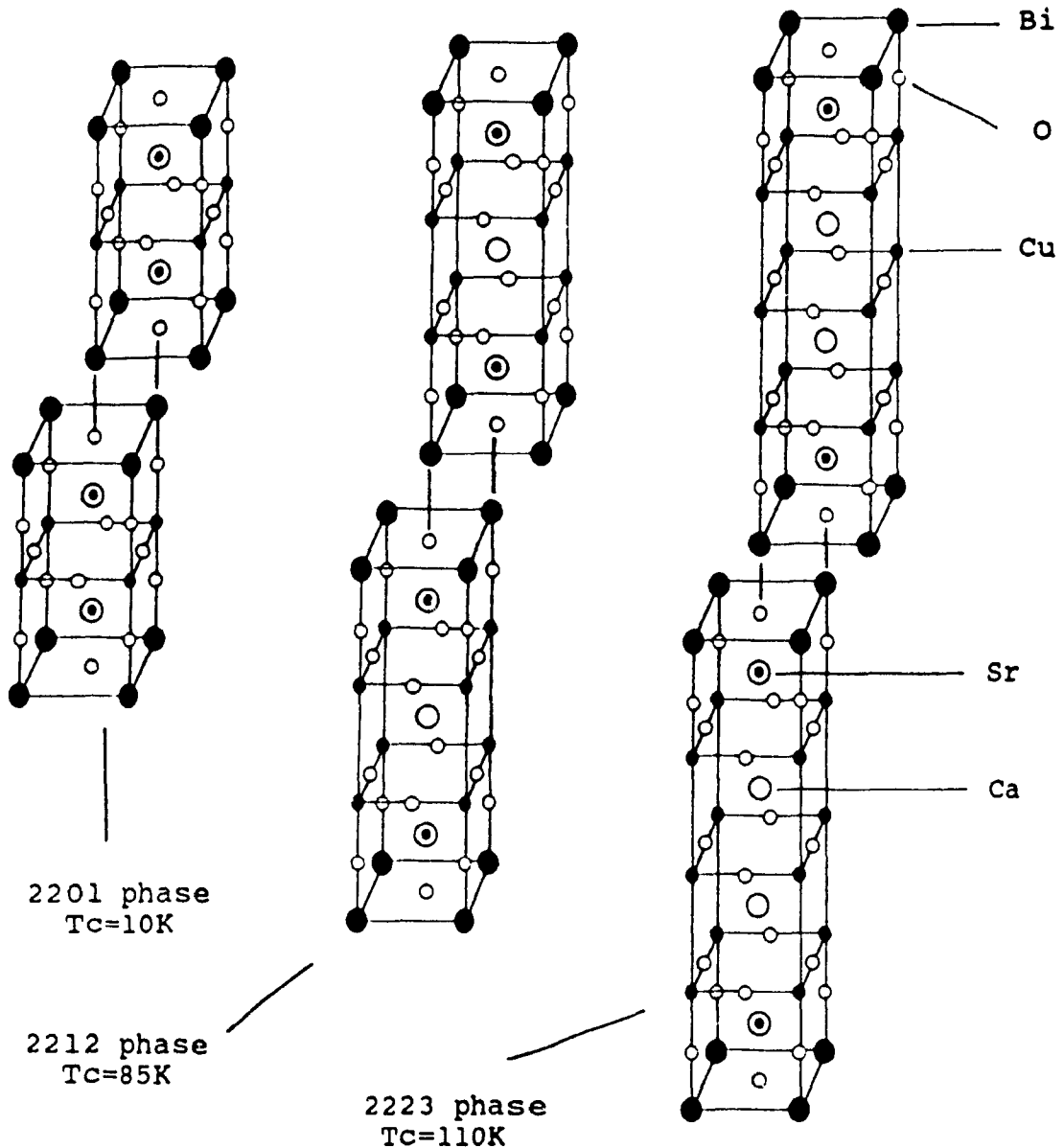
The superconducting phases in the bismuth system may be described as a stacking of calcium and copper oxide planes alternating with double Bi-O layers. Figure 3-1 shows the three structures. The copper oxide layers are believed to be responsible for the superconductivity of the compound as it is the case with the other copper oxide superconductors. The critical temperature of the different phases is related to the number of copper oxide planes. As the number of copper planes is increased, the critical temperature also increases.

The low-Tc phase has only one copper oxide plane. It has an orthorhombic unit cell with parameters  $a = 0.5362$  nm,  $b = 0.5374$  nm, and  $c = 2.4622$  nm. In fact the structure is complicated by the tilting of atoms from one block to another, reducing the number of crystal symmetries (figure 3-1). The unit cell is shown on figure 3-2. It also has an incommensurate modulation due to the periodic displacement of bismuth atoms from their average position. The modulation is described by the wave vector  $q^* = 0.213a^* + 0.61c^*$  [43]. Figure 3-1 shows that the structure consists of a basic block stacked with one corner placed over the center of the following block. Each block has a 1.23nm length. Owing to the crystallographic shear described above, the unit cell has twice this length (2.46nm). Each block has a copper oxide plane between two strontium planes, and the whole is sandwiched between two bismuth oxide layers.

The 2212 phase is derived from the 2201 phase by adding a calcium plane and another copper oxide plane (see figure 3-1). The proportions of strontium and calcium may vary. Grader et al. [22] obtained the 2212 phase

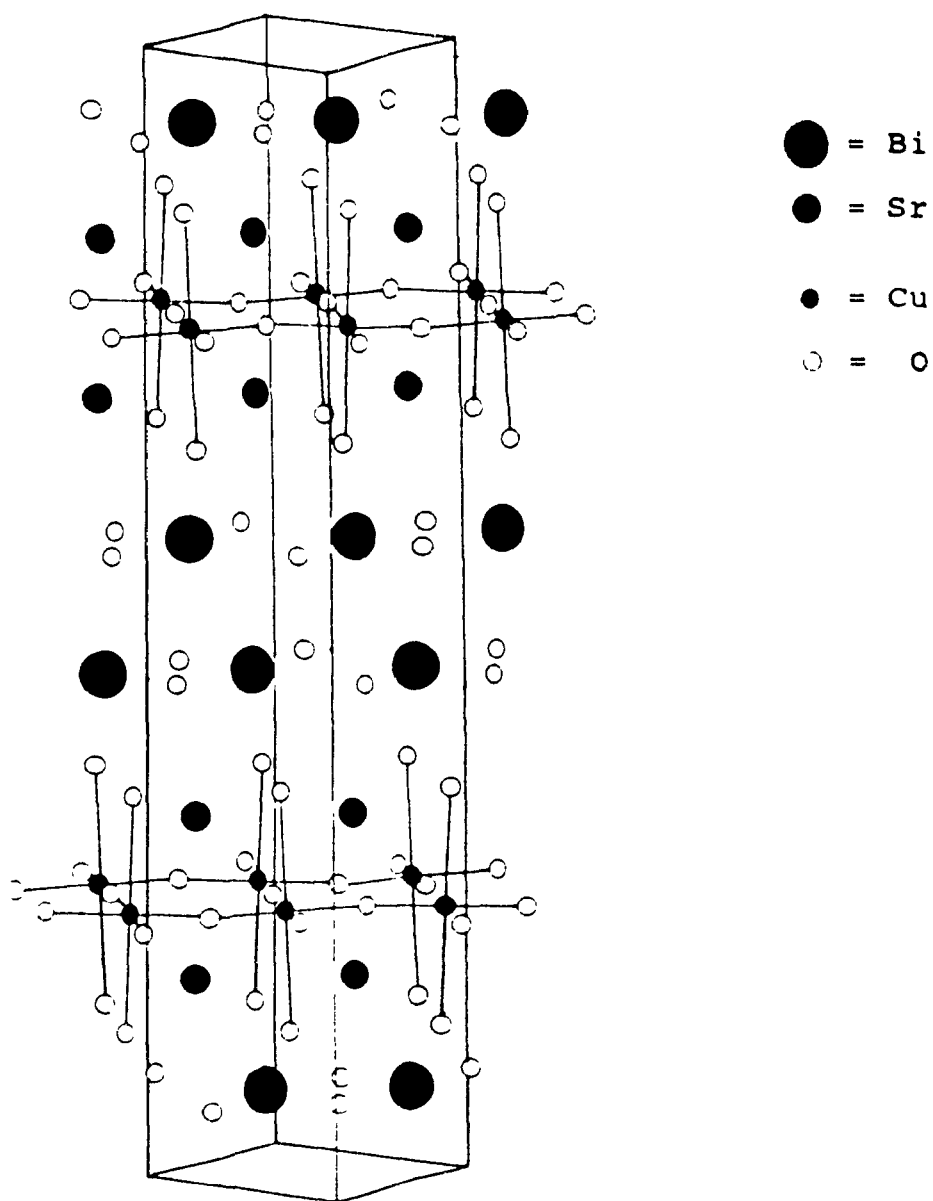
with Sr:Ca ratios of  $3-x:x$  where  $x$  is in the range  $0.8 < x < 2.2$ . Some bismuth is found on calcium sites (see Sunshine et al. [71]). The modulation in the 2212 phase is described by  $q^* = 0.210a^*$  [43]. Again the building of the structure is shown on figure 3-1. In the case of the 2212 phase, a light shear deformation of the building blocks leads to a unit cell with  $a$  and  $b$  approximately equal to  $\sqrt{2} \times 0,38\text{nm}$ .

Figure 3-1. Idealized representation of the structure of superconducting phases in the Bi-Sr-Ca-Cu-O system.



Adding another calcium-copper oxide block leads to the 2223 phase. Although this phase has been known since the discovery of the Bi-Sr-Ca-Cu-O, it has hitherto not been possible to obtain single-phase materials, which has made the precise determination of its structure difficult.

Figure 3-2. Unit cell of the 2201 phase (based on the model of ref.[76]).



In fact, only the lattice parameters have been determined with good precision [88]. The diffraction data given on table 6 in the appendix is calculated [43] assuming a structure similar to that of  $Tl_2Ba_2Ca_2Cu_3O_x$ . In the case of the 2223 structure, the building blocks of figure 3-1 actually form the basis of the crystal structure and the a and b parameters are both equal to 0,38nm.

Tables 1 to 6 in the appendix give structural data for the three superconducting phases described. Also given are the experimental diffraction intensities and those calculated by Matheis and Snyder [43] who published these tables.

### 3.3. Bismuth Oxides Made by the Technique of Rapid Solidification.

Rapid solidification has been used to make amorphous precursors for the bismuth-based superconductors. Komatsu et al. [35] were among the first to try this idea. They used a rather simple technique: the melt was poured onto an iron plate and pressed (this is called splat quenching). The sample thickness was 3mm. Their composition was  $BiSrCaCu_2O_x$ . No X-ray pattern was given. They obtained  $T_c(\text{onset})=102K$  and  $T_c(\text{zero})=92K$  for a sample crystallized by annealing in oxygen at  $820^{\circ}C$  for 24 hours and quenched in liquid nitrogen. The values for another sample treated in the same way but at a temperature of  $800^{\circ}C$  were  $T_c(\text{onset})=102K$  and  $T_c(\text{zero})=86K$ . This last sample had a  $J_c$  of  $102A/cm^2$ . They also found that rapid cooling in liquid nitrogen, rather than slow furnace cooling, was essential to get a sharp transition. They concluded that this was because the 110K phase was stable only above  $820^{\circ}C$ . In a subsequent paper [36] they presented an X-ray diffraction pattern for amorphous  $Bi_{1.5}SrCaCu_2O_x$  displaying a halo at  $2\theta=30^{\circ}$ . They claimed this as evidence for the first production of an amorphous phase in the bismuth system. They found a glass transition (the transition from an amorphous phase to a viscous liquid)

at 700K and a crystallization peak at 765K for a heating rate of 5K/min. Their DTA (differential thermal analysis) curve shows another exothermic peak at 904K and two endothermic events at 1041K and 1056K. For the composition  $B_{1.5}SrCa_{1.5}Cu_2O_x$ , the glass transition is at 696K and the crystallization at 766K.

Since then, many articles have been published about rapid quenching of bismuth-based oxides and the references are given in tables 7-9 in the appendix. Rather than enumerating all the results summarized in these tables, we shall stress the common features of the different papers.

Most groups employing the twin roller technique claim the highest quenching rates ( $10^6$ K/s); the as-quenched material however, is not found to be of significantly better quality than those obtained by splat quenching or conventional single roller melt-spinning. All groups reporting the presence of an amorphous phase find a broad peak at 30 degrees ( $d=0,3$ nm for CuK $\alpha$  radiation) in the X-ray diffraction pattern. Some groups also report broad peaks at 20 and 50 degrees. Calcium oxide is the most common impurity. Moderate variations in composition do not have a significant effect on the resulting phases after quenching.

If we now look at the transformations as seen by thermal analysis either by DTA or DSC (differential scanning calorimetry), there are differences between the results of the various groups. The glass transition temperature is approximately 680K. The crystallization temperature is around 725K. A second exothermic peak is often seen but at a temperature much more variable than that of the first peak. There are a few values in the range 750-775K and the others are above 800K. The melting point is generally close to 1125K. Again, it must be noted that these are major features of thermal studies and that many experiments reveal details not reproduced by others.

The resistive measurements of the annealed samples are similar to those obtained with samples prepared by solid state reaction, with one or two transitions, at 85 and 110K. The best critical current at the temperature of liquid nitrogen is 100A/cm<sup>2</sup>.

Some groups have attempted to describe the structural transformations leading to the formation of superconducting phases. Here we shall explain the qualitative information found by different workers.

Shi et al. [67] state that the 85K phase crystallizes first, and that calcium and copper rich regions are created. As annealing is continued, the calcium and copper diffuses in the 2212 structure leading to the formation of 2223 regions at the interfaces between zones of 2212 phase and calcium-copper oxide. This is clearly seen by transmission electron microscopy [66]. Excess calcium and copper in the starting mixture (compared to the 2223 stoichiometry) enhances the formation of the 110K phase. They have shown [66] that lead additives ease the diffusion of calcium and copper into the 2212 structure. Their results show that lead substantially reduces the time necessary for the formation of the 2223 phase.

Similar results were found by Takei et al. [72]. In their experiments, the 2201 phase crystallizes first, then this phase reacts with the rest of the material to form the 2212 phase.

The most detailed paper is the one by Nassau et al. [51] where they report that the first crystallization peak in the DTA scans is due to the formation of an ordered phase with broad X-ray peaks for a 4:3:3:4 starting composition. It is still not clear what this phase may be. When the initial composition is 2:2:2:3 the sample exhibits well defined

crystalline peaks after the first exotherm. Nassau et al. claim that the  $\text{CuBi}_2\text{O}_4$  phase is formed but the main diffraction peak of this phase is missing and they give no explanation for this absence. At higher temperature this phase transforms into the 2201 phase which is replaced later by the 2212 phase.

In summary, the generally accepted picture is that the 2201 phase is the first to crystallize. At the same time calcium and copper-rich regions are formed. As annealing continues, the diffusion of calcium and copper into the 2201 phase produces the 2212 phase. Further diffusion leads to the formation of the 2223 (110K) phase in certain cases. The crystallization of intermediate phases before the formation of the 2201 phase is reported only by Nassau et al. [51].

To conclude this section we may say that we have a good understanding of how the 10K phase transforms into the 85K phase and subsequently into the 110K phase. More work has to be done, however, to explain the earliest stages of crystallization and to identify the phases that may form just before the 2201 phase.

## Chapter 4

### Amorphization by High-energy Ball Milling.

#### 4.1. The Historical Development.

Since their initial discovery by Duwez et al. [15] in 1960, amorphous alloys of metallic elements have been mostly synthesized by rapid quenching from the melt, usually by the technique known as melt-spinning. The quenching process imposes a limit on the size of the samples because of the cooling rate requirements. Today it is possible to manufacture wide sheets of amorphous metallic alloys. However, thickness is limited to the order of 50 microns. An alternative process, called mechanical alloying, is now widely used in laboratories to make these new alloys and offers the prospect of manufacturing amorphous alloys in bulk form.

Mechanical alloying is a process in which an alloy is formed by direct reaction in the solid state between elemental components, which are subjected to intense mechanical deformations. The apparatus usually consists of a container placed in a rotating (e.g. attritor, planetary ball mill) or vibrating frame (shaker mill). Inside the container is placed a certain number of balls made of hard steel or tungsten carbide and the material to be alloyed, called the charge. Non metallic ball mills (e.g. agate) also exist but these are usually used for mixing and not for alloying. In the present work we have used only metallic balls and vials.

We may define high-energy ball milling as a ball milling process in which the energy transfer to the charge is such that it provokes structural modifications at the atomic level. In typical high-energy ball mills the speed of the balls is above 1 m/s, the collision time and peak

stress at impact around 0,01 microsecond and 50kbar (500kPa) respectively.

In the past mechanical alloying by ball milling has been extensively used to produce dispersion strengthened alloys [19]. In these alloys a small quantity of oxides is dispersed in a metallic matrix. Following the work of Yermakov et al. on Y-Co and Gd-Co [84,85] which was not widely known, an article by Koch et al. [34] published in 1983 attracted the attention of materials scientists to the possibility that amorphous alloys could be synthesized by ball milling. After a little more than 10 hours of milling in a SPEX 8000 mixer/mill they obtained amorphous  $Ni_{60}Nb_{40}$ , as seen by X-ray diffraction, from a mixture of pure elements. Schwarz and Koch [64] subsequently produced amorphous alloys in the Ni-Ti system.

These results were since confirmed by many other groups and at the time of writing many different amorphous alloys have been produced by this technique. Comparison between amorphous alloys produced by ball milling and rapid quenching [7] shows only minor differences in some physical properties and it is concluded that both processes lead to the same atomic structure.

Almost all of the research has been concerned with ball milling metallic ductile materials. In brittle materials, the situation is somewhat different. Two articles on Si-Ge [13,14] have shown that in this system amorphization is not achieved but rather a solid solution is formed.

#### 4.2. The Process of Ball Milling.

The mechanics of ball milling has been first described by Benjamin and Volin [6]. It involves repeated fracture and cold welding of the powders. As far as ductile elements are concerned, repeated fracture and

cold welding of particles lead to the formation of a layered structure made from the two starting elements (in the case where we start with two elemental powders) as shown by scanning electron microscopy. It is believed that a solid state amorphization reaction is taking place at the interfaces, similar to the one described by Schwarz et al. [63] for Au-La multilayers. The layered structure present in ball milled powder particles provides clean interfaces for a diffusive reaction between the two elements. Continuous homogenization of the powder leads to a complete reaction. We will describe the present state of knowledge regarding the microstructural processes later.

When we start with an intermetallic compound instead of elemental components to form an amorphous alloy, the mechanism is different. In this case, the introduction of a large quantity of defects during the milling process is such that the structure collapses into the amorphous state. The process is also different when brittle materials are considered. The system under study, a mixture of oxides, is extremely brittle and may also be expected to behave in a different way than ductile materials.

In a review on ball milling, Weeber and Bakker [79] have identified three types of reactions occurring when ball milling elemental powders:

- Type I: continuous decrease of the crystallite size (as shown by peak broadening in the X-ray diffraction pattern) finally resulting in an amorphous alloy from gradual interdiffusion and particle refinement
- Type II: decrease of the crystalline peak intensities together with an increase of a broad amorphous peak, the amorphization follows from an interdiffusion process similar to that found in multilayered systems
- Type III: formation of one or more intermetallic compounds followed by further transformation into an amorphous alloy

In Type II reactions, there is no important decrease in the crystallite size after some time, but the reaction occurs and the peak intensities do diminish, whereas in Type I, the decrease in the crystallite size goes on until the amorphous alloy is formed. Here are some examples of each reaction type:

Type I:  $\text{Nb}_{75}\text{Ge}_{25}$  [56]

Type II: Ni-Ti [65],  $\text{Ni}_{62}\text{Zr}_{38}$  [80]

Type III:  $\text{Ni}_{62}\text{Zr}_{38}$  [81].

We note that an amorphous alloy can be formed by two types of reaction depending on the equipment used. Collision energies and temperatures may significantly vary from one type of mill to another, thereby affecting the dynamics of reaction. A series of X-ray patterns for different milling times is given in figure 4-1; the system is Ni-Zr and the equipment a SPEX 8000 mixer/mill. The reaction is of Type II.

#### 4.3. The Thermodynamics of the Process.

There are two conditions to the formation of an amorphous binary alloy starting from pure elements [63]:

- 1) The two elements must be an asymmetric diffusion couple.
- 2) The heat of mixing must be negative.

An asymmetric diffusion couple is a binary system in which one element diffuses into the lattice of the other when in contact. The heat of mixing is defined as the difference in free energy between a state in which the two components are in separate crystalline states and one in which the two components are mixed in a solid solution. In what is called the quasi-

Figure 4-1a. X-ray diffraction patterns of  $\text{NiZr}_2$  as a function of milling time (taken from [61]).

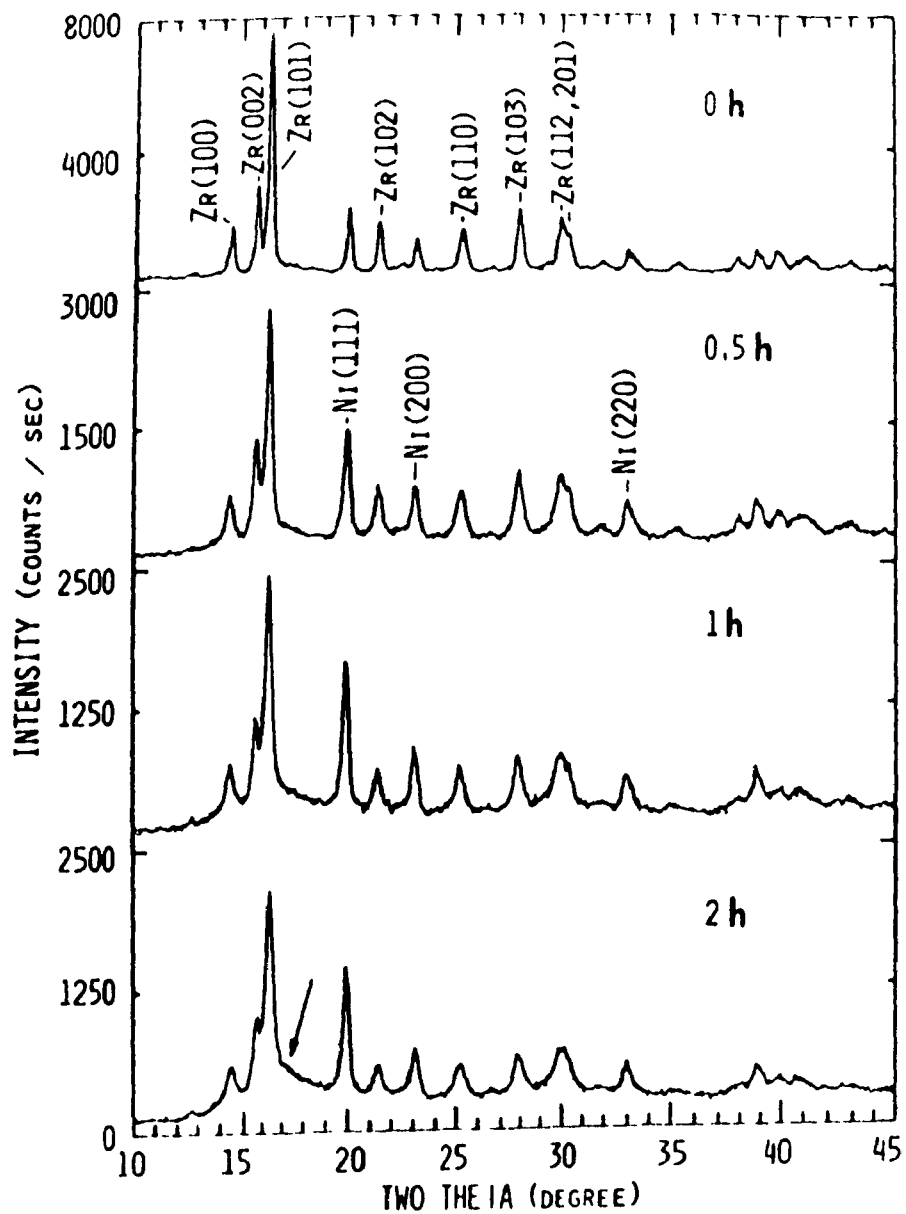
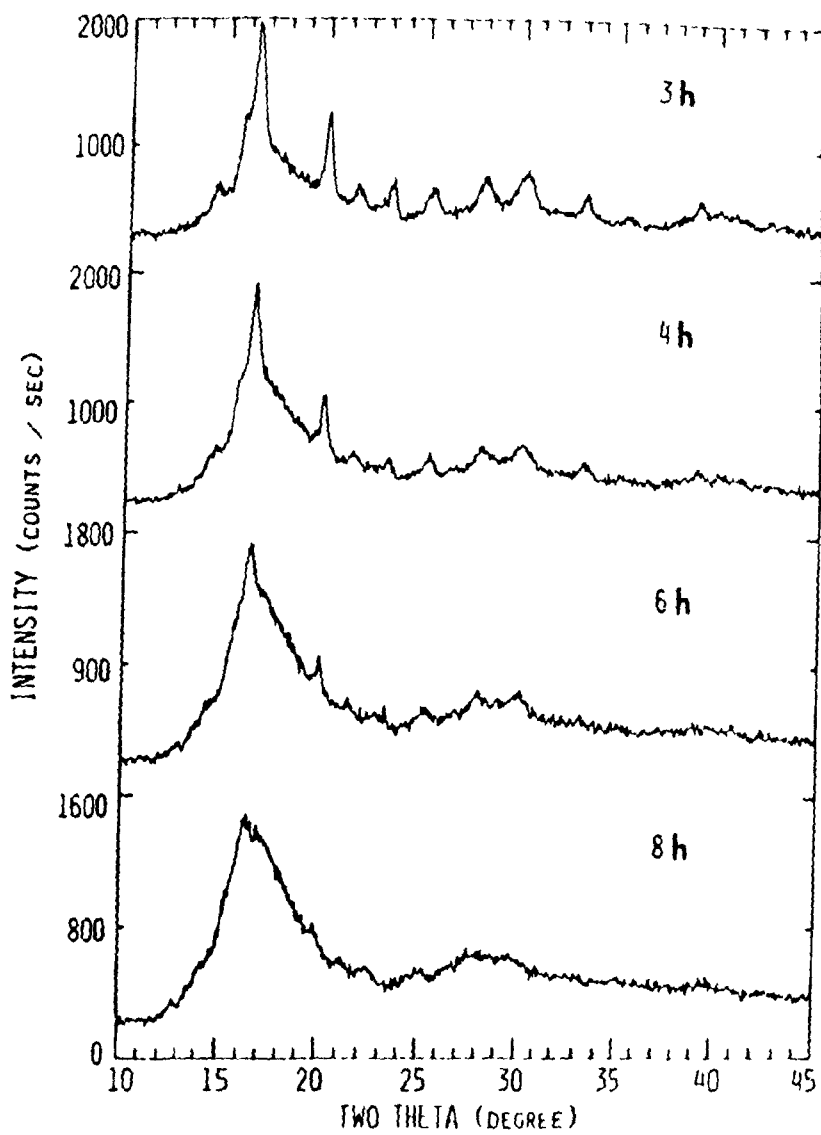


Figure 4-1b.

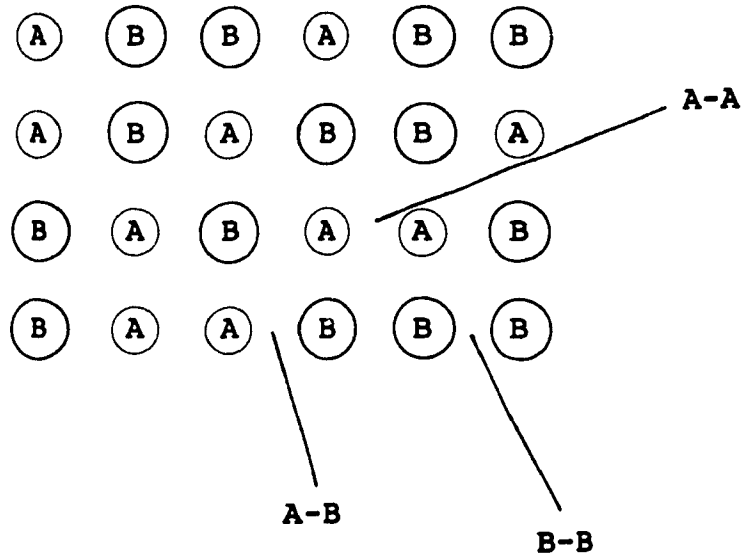


chemical model [42] we assume that the heat of mixing of two components A and B arises from the difference in the energy of chemical bonds A-A and B-B, and of mixed bonds A-B. In such a case the heat of mixing may be expressed by the equation:

$$G_{MIX} = \Omega X_A X_B + RT(X_A \ln X_A + X_B \ln X_B) \quad (3-1),$$

where  $\Omega = N_a z \epsilon$ , and  $X_A, X_B$  are the molar fractions of each component while  $N_a$  is the number of atoms per mole,  $z$  is the coordination number (the number of nearest-neighbours of an atom in the structure), and  $\epsilon$  is the difference in bond energy.  $\epsilon = (H_{AA} + H_{BB}) - 2H_{AB}$ . Figure 4-2 illustrates the situation.

Figure 4-2. The mixing of two components.



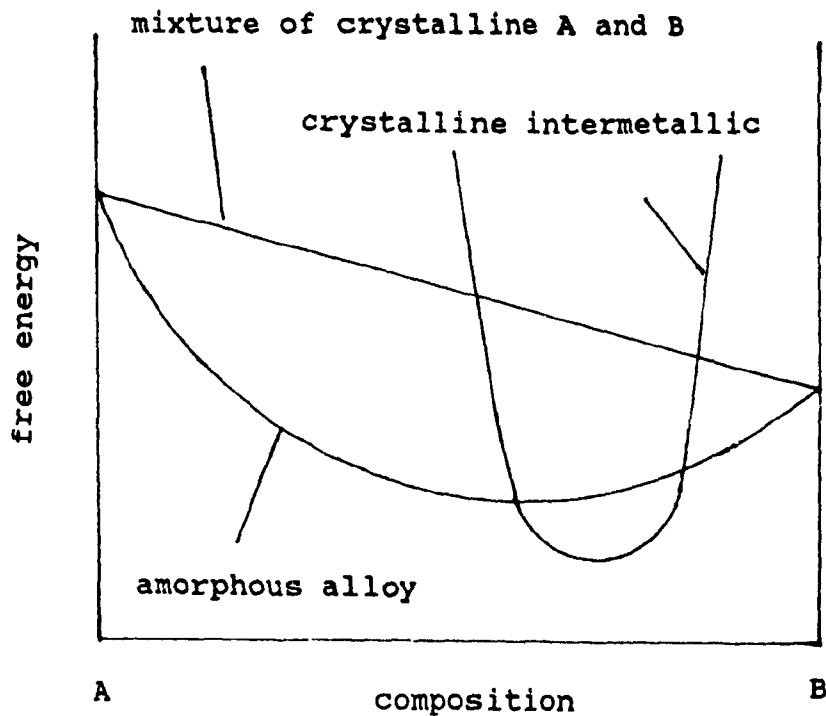
The heat of mixing is large and negative when  $\epsilon \ll 0$  or  $2H_{AB} \gg H_{AA} + H_{BB}$ .

The condition of having an asymmetric diffusion couple can be expressed in a more quantitative way. For example, it is found empirically [79] that in a transition metal-zirconium system the ratio of the atomic

radius of the transition metal to that of zirconium must be less than 0.58. For a different host (the bigger atom) the maximum ratio is different.

The diffusion of one element into the other occurs at the interfaces formed between the two components. The system is driven by the negative heat of mixing into a state of lower free energy (the metastable amorphous state) while the transformation into the most stable crystalline state is kinetically suppressed, either because the temperature does not rise above that of the glass transition or because the material cools too rapidly after each impact for crystallization to take place. The following free energy diagram illustrates the situation.

Figure 4-3. Free energy diagram.



The amorphization from intermetallic compounds occurs when a sufficient amount of defects increases the free energy of the system above that of the amorphous alloy. The system then lowers its free energy by transforming into the amorphous state. It is also probable that the mechanically induced defects also play a role in the case of the amorphization from the elemental components. This hypothesis is currently under investigation [62].

It must be noted that not all intermetallics can be amorphized by ball milling and that the result of these experiments may strongly depend upon particular parameters related to the equipment used. The inverse reaction is possible: some amorphous alloys become crystalline when submitted to ball milling [60].

#### 4.4. The Glass-forming Range.

The glass-forming range associated with a given manufacturing technique is the concentration range over which a single amorphous phase can be made. X-ray diffraction is an insufficient test to determine whether the material is single phase since around 1 weight % of a phase must be present to be detected and it gives no information about composition variations. The best way is to measure a physical property such as the superconducting critical temperature of the amorphous phase [25]. Usually, the critical temperature continuously varies as a function of composition of the amorphous phase. When a composition limit has been reached and a crystalline phase is formed, the critical temperature remains constant and takes the value it has at the limit, whatever the amount of crystalline phase formed. This behavior can also be seen with other physical properties such as the crystallization temperature or enthalpy.

It has been shown that the glass-forming range for rapidly solidified alloys is centered around deep eutectics whereas the amorphization range for ball milling is usually wider and comprises some regions of intermetallic compounds. Ball milling has therefore made possible certain alloys that could not be synthesized otherwise. The difficulty to make amorphous alloys by rapid solidification with composition far from an eutectic is due to the difficulty of avoiding the formation of crystalline intermetallic compounds.

#### 4.5. An Analysis of the Physics of Ball Milling.

In the early days of amorphization by ball milling there was no quantitative understanding of the physical processes occurring. Such problems as the movement of the balls, the amount of powder crushed during collisions, the distribution of angles of collision, and the transfer of energy during collisions ..., were still to be addressed. Recently however, a model has been put forward by Maurice and Courtney [44]. They use Hertz's impact theory [40]. They assume that ball on ball and ball on wall collisions (without powder) are elastic (the compression energy is restored after impact). They then suppose that the powder between colliding surfaces does not substantially alter the collisions. Calculations show that for a SPEX mill, the amount of energy transferred to the powder is of the order of a few percents of the energy of compression. Their model has not yet been applied to the understanding of a particular alloy but it gives some information about the temperatures encountered during ball milling, as we shall see in the next section.

#### 4.6. The Question of the Temperature.

A very important question yet to be resolved in any analysis of ball milling is a precise evaluation of the temperatures that the powders

attain during the process. Two temperatures have to be considered: the average ambient temperature in the vial and the maximum local temperature during collisions.

The ambient temperature is slightly higher than room temperature (a fact easily observed by directly measuring the temperature of the container) but this has little effect on the process since it is much less than the maximum local temperature during the collisions. Maurice and Courtney [44] showed that in a SPEX mill, powder grains had enough time to cool to ambient temperature between the collisions. They give temperature rises for several materials and mill configurations. Values are generally below 200K. However we should be cautious. Miller et al. [49] determined that crystalline solids submitted to a rapid deformation show local temperature rises far greater than those one would get assuming that the heat is distributed over all the material. Davis et al. [14], using a computer model, found that temperature rises were no more than 350K and confirmed this in an experiment where they monitored the martensitic transformation of a certain type of steel. They concluded that no transformation involving temperature rises higher than 300K occurred. However, ball milling is very different from a thermal process and usually structural transformations cannot be explained as being caused solely by heating, a fact that has been clearly demonstrated recently [77].

In conclusion, thermal phenomena in the ball milling processes are not clearly understood: the temperatures encountered during collisions are not precisely known, furthermore, brittle materials may have different temperature rises than metals.

#### 4.7. Ball Milling of High-Tc Superconducting Systems.

Batalla and Zwartz [4] tried ball milling the metallic precursors

of the Y-Ba-Cu-O system. They report complete amorphization for certain compositions and superconductivity at liquid nitrogen temperature after proper oxidation of their metallic glass. Lavallée [37] worked on the Y-Ba-Cu-O oxide system (Lavallée has milled a mixture of oxides of yttrium, barium, and copper while Batalla and Zwartz milled pure yttrium, barium, and copper, without oxygen) but he did not obtain a completely amorphous material for the 123 composition. This work is very close to ours. The milling of a  $Y_2O_3+4BaO_2+6CuO$  mixture results in a product containing  $BaCuO_2$ , a new disordered  $(Y_{0,33}Ba_{0,67})CuO_2$  cubic phase related to the superconducting phase, and possibly other phases. Milling the superconducting phase yields the disordered phase. Lavallée has shown in his work that brittle materials may possibly form a lamellar microstructure similar to that observed with ductile materials.

There are two articles on the grinding and subsequent annealing of crystalline Bi(Pb)-Sr-Ca-Cu-O [2,33]. These papers show that the crystallite size decreases as a function of milling time and partial amorphization of the 2223 high- $T_c$  phase occurs. Subsequent annealing of the amorphous phase leads to the formation of the 2212 phase. No details were given about the crystallization process. In this work we start from a mixture of oxides of each metallic component and give a detailed description of the various phase transformations occurring.

It must be noted that the synthesis of ceramic materials by ball milling is a new field and that this work on the ball milling of superconducting ceramics is one of the very first reports on such researches.

## Chapter 5

## Experimental Method.

## 5.1. Experimental Procedure for Ball Milling.

Listed below are the four oxide powders used in the experiments, together with relevant information concerning the purity claimed by the manufacturers and the average particle diameter.

Table 5-1. Powders used in milling experiments.

Oxide	Supplier	purity	size
$\text{Bi}_2\text{O}_3$	Johnson Matthey Aesar Group	99,9998%	600 $\mu\text{m}$
SrO	Johnson Matthey Aesar Group	99,9%	140 $\mu\text{m}$
CaO	Johnson Matthey Aesar Group	99,95%	4 $\mu\text{m}$
CuO	Fisher Scientific Company	99,8%	43 $\mu\text{m}$

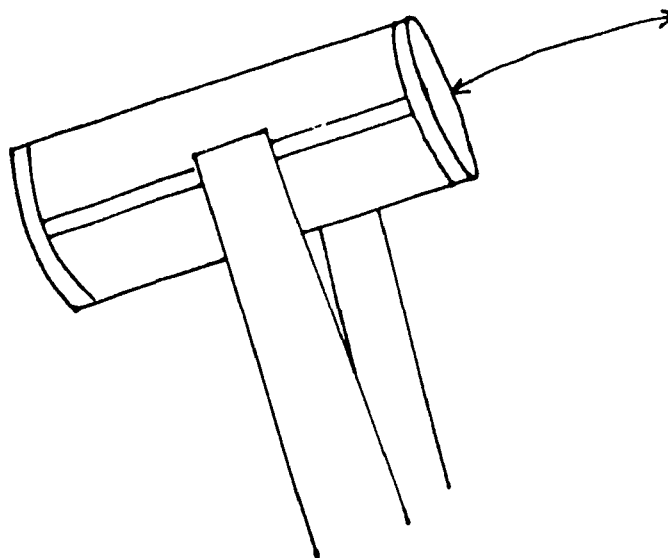
The vial used was made of steel with measured Rockwell C hardness not less than 60. Its diameter was 38,5 mm and its height 57,5 mm. The four stainless steel balls (measured hardness: 55 Rockwell C) used had a mass equal to 5,63 g. The measured fluctuations in mass between balls were around 0,01 g. The diameter of the balls was 7/16 of an inch (11,1 mm). The vial was placed in a SPEX 8000 mixer/mill, a laboratory mixer with a vibrating frame.

The ratios of the elements to enter the composition (other than oxygen) were chosen to be  $\text{Bi}_2\text{Sr}_2\text{Ca}_2\text{Cu}_3$ , which are the generally accepted stoichiometric coefficients of the 110 K phase. The oxides used for mixing

were  $\text{Bi}_2\text{O}_3$ ,  $\text{SrO}$ ,  $\text{CaO}$ , and  $\text{CuO}$ , a choice which gives ten atoms of oxygen for the Bi-Sr-Ca-Cu-O system, the correct concentration of oxygen in the 110K phase. The powders were weighed with a precision of  $\pm 1\text{mg}$  for each oxide in the case of milling times greater than or equal to an hour, and  $\pm 10\text{mg}$  when milling times were under one hour. The total mass of powder put in the vial was 7g in all cases.

After introducing the powders and the steel balls, the vial was sealed in an argon atmosphere (purity: 99.996%) with a steel cover together with a rubber ring lubricated with silicon grease. Had the vial been sealed in air the quantity of oxygen would have been about 25mg compared to a sample mass of 7g, therefore sealing in argon was not a crucial precaution but we preferred to control this condition in our experiments. The movement of the vial consists of a  $2\frac{1}{4}$ " swing at the end of a  $3\frac{1}{2}$ " arm as shown on the figure below. This swing is along the symmetry axis of the vial. There is also a horizontal motion of  $\frac{9}{16}$ " and a vertical motion of  $\frac{3}{16}$ ". The cycle is repeated 1200 times per minute.

Figure 5-1. Motion of the vial in the SPEX 8000 mixer/mill.



## 5.2. DSC Measurements.

DSC (differential scanning calorimetry) is basically a measurement of the heat capacity of a material. It also measures the exchange of heat during phase transformations. We use it to obtain the change in enthalpy during structural transitions and activation energies [10] of exothermic reactions. The crystallization peak observed allows us to characterize the amorphous phase present in a material.

As shown on figure 5-1 there are two containers, one is left empty and used as a reference and the other contains the sample under investigation. A ramping curve is programmed to give a linear variation of temperature as a function of time. A purging gas flows through both chambers at all times. The apparatus has a feedback system that adjusts heating power in order to keep the temperature in the sample chamber equal to that in the reference chamber. The variation in power output, whether positive or negative, is converted into numerical data. DSC measurements require calibration for the baseline, the temperature, and the energy. The baseline calibration is carried out with no sample; the objective is to obtain a baseline as flat as possible (i.e. when one only puts sample holders in both chambers, the heat capacity measured is supposed to be zero). The calibration for temperature and energy output is done with the help of a known standard. The transition temperature and the corresponding enthalpy variation of the standard are measured with the DSC and the necessary adjustments are made to the computer program to calibrate the instrument.

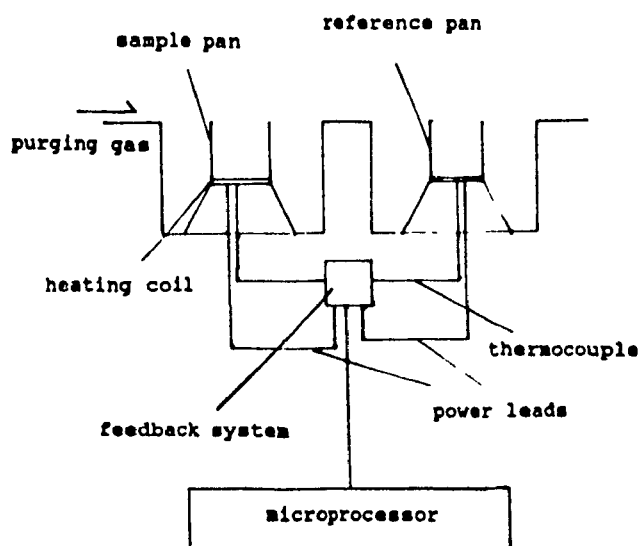
It is also possible to use the DSC to cool a sample rather than to heat it, or to operate at a fixed temperature and take measurements as a function of time.

In our case, DSC experiments were performed with a Perkin-Elmer DSC-2 differential calorimeter. The purging gas used was argon (purity: 99.996%). Scans ranging from 350 to 999K were done at rates of 10, 20, 40, 80, and 160K/min. The mass of our samples was between 2 and 6 mg, allowing us to use the calorimeter without the need of additional mass in the reference pan to balance the signal. The samples used consisted of the powder obtained after milling for 48 hours. Copper sample holders were used in all experiments.

### 5.3. TGA Measurements.

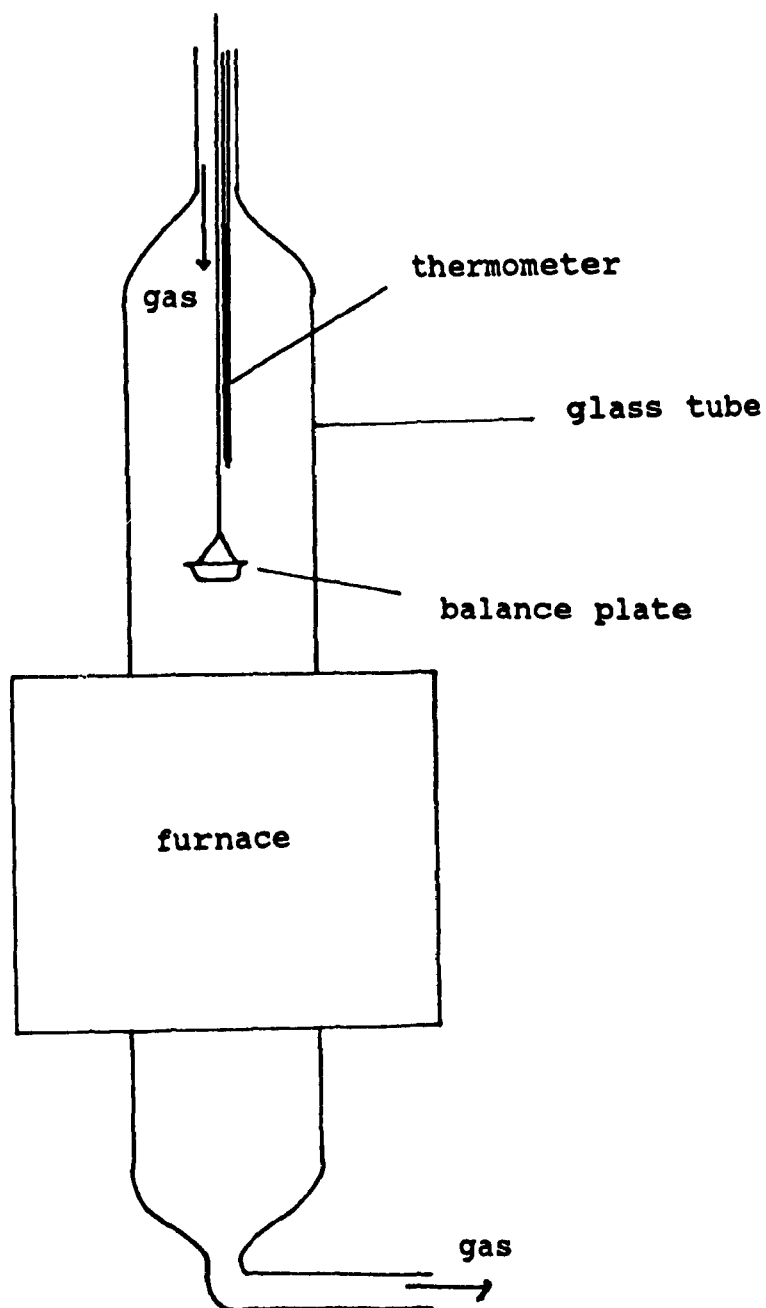
TGA (thermogravimetric analysis) is a type of experiment in which the weight of a sample is measured while the sample is subjected to a thermal treatment. It consists of a balance put in a closed environment, a heating device below the balance plate and a thermometer close to the sample (see figure 5-2). It is especially useful in the study of high- $T_c$  superconductors for the detection of oxygen exchanges between the material and the atmosphere used in the thermal treatments.

Figure 5-2. Differential scanning calorimeter (DSC).



Our TGA was a Perkin-Elmer TGA7 with a balance sensitivity of 10 micrograms and a precision of 1%. A certain background is produced upon heating, this background has to be subtracted from the experimental curve.

Figure 5-3. Thermogravimetric analyser (TGA).



#### 5.4. Procedure for Thermal Treatments.

Thermal treatments were done in a microprocessor-controlled tubular furnace with a thermometer close to the sample's location. Variations in the 2K range could be expected due to the temperature gradient in the furnace. When the thermal treatments consisted of a ramp between two temperatures an additional 3K uncertainty had to be expected because of the time necessary to take the sample out of the furnace. Samples were put in alumina boats. No excessive reaction was observed. Argon and oxygen (both 99,996%) were used as purging gases. All treatments consisted of a ramp at a constant heating rate followed by a quench in air except for one sample annealed in oxygen at 1125K for 20 hours and a Bi-Ca-O sample annealed at 800K for 1 hour.

#### 5.5. X-ray Diffractometry.

##### 5.5.1. Instrument.

X-ray diffraction patterns were taken on a Siemens D500 diffractometer controlled by a Digital PDP-11 computer equipped with the software necessary for data retrieval and analysis. CuK $\alpha$  radiation was used. The wavelength is 0,1541 nm. The diffractometer was used in the following configuration:

collimating tube mounted

slits I-II-III: 1 degree (divergence and collimating slits)

slits IV: 0,05 degree (receiving slit for the monochromator)

monochromator: curved graphite (in the diffracted beam)

slit V: 0,15 degree. (receiving slit for the detector)

The precision of the alignment was 0,0015 degrees for 2 $\theta$ .

### 5.5.2. Measurement of the Crystallite Size.

The position and width at half maximum of each peak were converted in  $k$ -space after subtraction of the  $\text{CuK}\alpha_2$  part:

$$k = \frac{4\pi\sin(\Theta)}{\lambda} \quad (5-1),$$

$$\Delta(k) = \frac{2\pi\cos(\Theta)\Delta(2\Theta)}{\lambda} \quad (5-2),$$

where  $\lambda$  is the wavelength and  $\Delta(2\Theta)$  is the width at half maximum. The instrumental broadening is assumed to be of the form:

$$\Delta(k_0) = ak + b \quad (5-3),$$

where  $a$  and  $b$  are constants calculated from least square fit using a standard material. The instrumental broadening is subtracted from the experimentally measured width using the formula:

$$\Delta(k')^2 = \Delta(k)^2 - \Delta(k_0)^2 \quad (5-4).$$

Neglecting the effect of strain the crystallite size is calculated from the average broadening:

$$L = \frac{0,9 \times 2\pi}{\langle \Delta(k') \rangle} \quad (5-5),$$

this is equivalent to the Scherrer formula [59]. To consider the effect of strain, which gives a linear contribution as a function of  $k$ , the width  $\Delta(k')$  is plotted as a function of  $k$ . The linear contribution of strain and the constant contribution due to the crystallite size can be separated. The crystal size  $L$  is given by (5-5) using the intercept of the

linear fit instead of the average width. The procedure is described in detail by Warren [78].

#### 5.6. Magnetic Measurements.

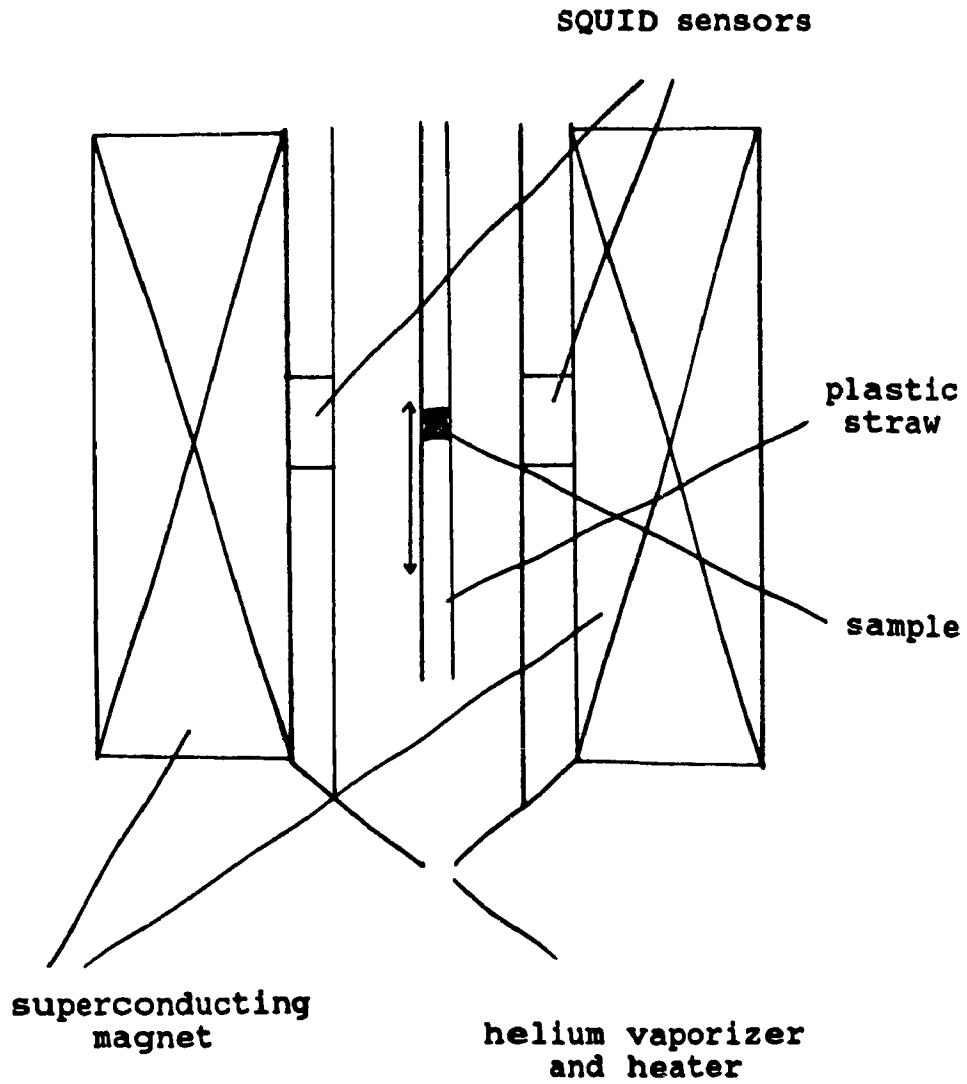
Magnetic measurements were taken using a Quantum Design SQUID magnetometer. In our experiments, the sample was cooled in zero field down to very low (4,2K) temperatures, a field was applied and the magnetic moment was measured as the sample was heated up to 150K (zero field cool or ZFC curve). The moment was measured as the sample was taken back to low temperatures (field cool or FC curve), then the field was put back to zero and the moment measured while the sample was heated (remanent field or REM curve).

The SQUID device is very sensitive to variations in the magnetic field. The sample is moved vertically while the squids beside the sample measure the variations in the magnetic field. The magnetic moment of the sample is calculated from these values. The sample is enclosed in a long plastic straw. Since the straw can be considered infinite with respect to the region where the measurements take place, its movement does not induce a modification of the magnetic field. The following figure illustrates the situation.

#### 5.7. Transmission Electron Microscopy (TEM).

The microscopic observations were done using a Hitachi H-9000NAR transmission electronic microscope having an acceleration voltage of 300kV and a point-to-point resolution of 0,2nm. The minimum beam size is 4nm (used for X-ray spectroscopy). The maximum magnification is 1 000 000X. We will present microscopic observations only for the amorphous phase obtained after milling. The structural characterization for crystalline

Figure 5-4. SQUID magnetometer.



samples was done by means of X-ray diffractometry. Energy dispersive X-ray analysis was used for chemical analysis. We did not use standard materials for calibration, therefore the precision was limited probably to the order of a few percents.

#### 5.8. Scanning Electron Microscopy (SEM).

A Hitachi S-570 microscope with an acceleration voltage of 20kV was used. EDX was used for chemical analysis. The same comments made for the TEM observations concerning calibration apply here.

#### 5.9. Contamination of Strontium Oxide.

Unfortunately, we could not keep strontium oxide from being in contact with the atmosphere at all times. This caused some of the strontium oxide to react and form  $\text{Sr}(\text{OH})_2$ . The maximum error in the amount of strontium measured is 15%. We expect the actual error to be in the range of 5 to 10%. The most intense X-ray peaks belonging to both of these phases are very close from each other and, because of noise in the X-ray patterns and peak broadening, it has been impossible to follow the evolution of strontium oxide by means of X-ray diffraction during the milling process. We expect, however, that it will have a behavior similar to that of calcium oxide. Strontium oxide will also be observed by EDX measurements. The hydrogen present in the sample because of  $\text{Sr}(\text{OH})_2$  will be released during heating.

## Chapter 6

### Results and Discussion.

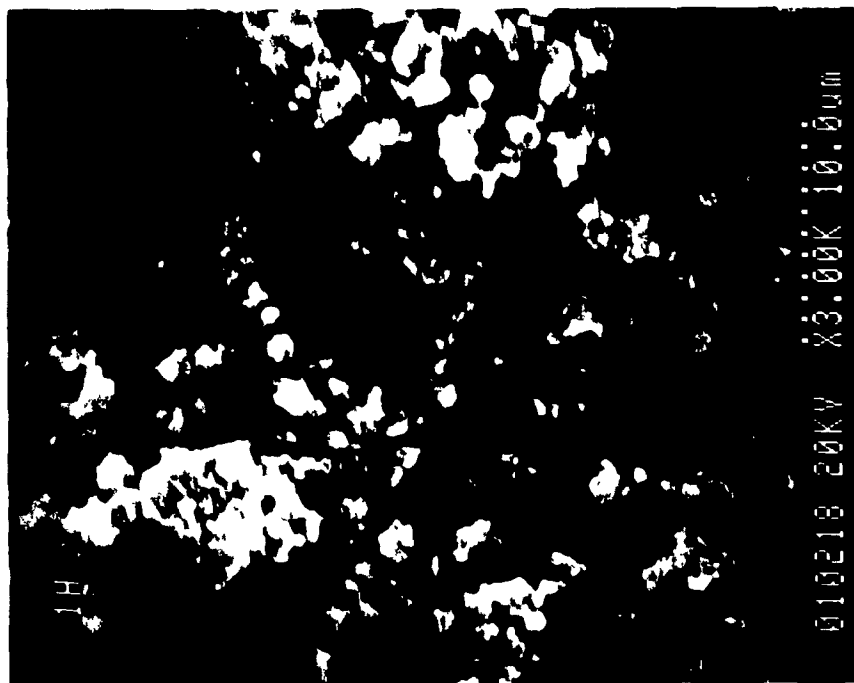
#### 6.1. Amorphization by Ball Milling.

The amorphization process in the Bi-Sr-Ca-Cu-O system, starting from a mixture of the four oxides, may proceed in two steps. A first reaction transforms  $\text{Bi}_2\text{O}_3$ , SrO, and CaO into a body-centered cubic solid solution. In a second step two reactions concur to destabilize the cubic phase: the addition of more and more Sr and Ca to the cubic solid solution raises its free energy above that of the amorphous Bi-Sr-Ca-O phase and the reaction between the crystalline solid solution and copper oxide also result in the amorphization of the material.

Evidence for the rapid initial reaction between the elemental oxides is given by scanning electron microscopy. After 1 hour of milling the powder consists of large agglomerates ( $>10$  microns), containing the four oxides, and smaller particles ( $\ll 10$  microns) which are essentially made of copper oxide (see tables 6-1 and 6-2). Figures 6-1a and 6-1b are scanning electron micrographs of the powder showing the small Cu-rich particles and the large agglomerates respectively. The micrographs of the powder milled 3 hours are shown on figure 6-2. We see that the agglomerates have become large dense particles. 6-2b shows one of these large particles while 6-2a gives a general view of the powder after this period of time.

Figure 6-1. Scanning electron micrographs of the powder milled 1 hour

a)



b)

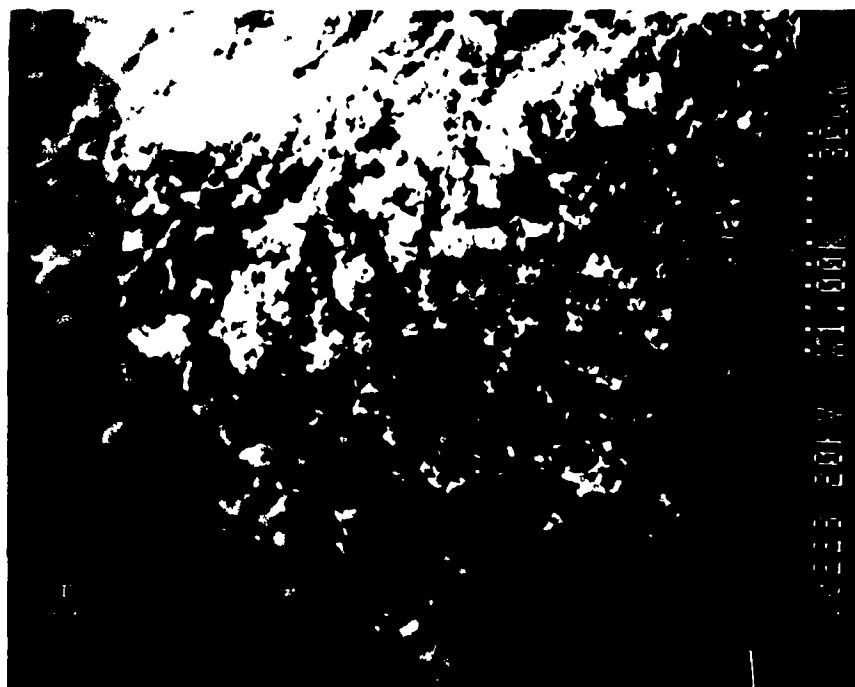


Table 6-1. Size and chemical composition of the large agglomerated particles after 1 hour of milling.

size (microns)	EDX analysis atomic % <sup>1</sup>			
	Bi	Sr	Ca	Cu
10	30	21	25	24
	24	16	19	42
	23	41	15	21
	27	21	19	33
25	26	27	21	26
	24	21	23	32
	25	19	32	24
	16	9	41	34
50	16	9	34	40
	16	10	56	17
	21	11	19	49
average value	22,6	18,6	27,6	31,2

<sup>1</sup> Not including oxygen.

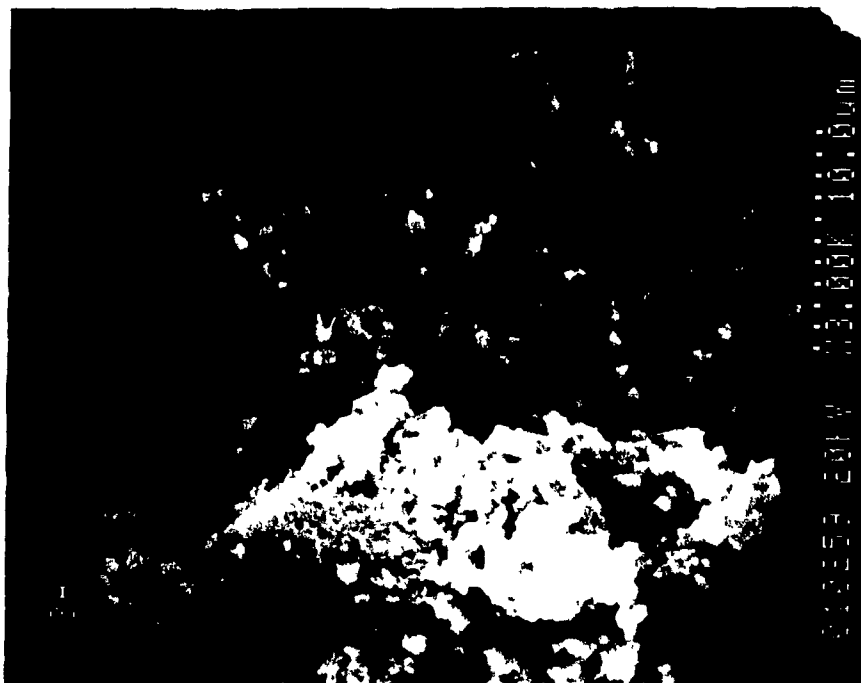
Table 6-2. Composition and size of the smaller particles after 1 hour of milling.

size (microns)	EDX analysis			
	atomic %			
	Bi	Sr	Ca	Cu
2	14	12	11	63
1	18	11	21	49
1	12	14	11	64
2	15	12	12	61
1	10	10	9	72
1	21	12	28	38
1,5	17	10	16	57
1	13	10	13	64
average value	15,0	11,4	15,1	58,5

From the presence of a large quantity of Cu-rich particles, it appears that copper oxide reacts much less than the three other oxides. This is what leads us to conclude that the first major reaction is one in which a Bi-(Sr,Ca)-O phase is formed. Of course, as we will see in the next pages, reaction of this phase with the remaining oxides will proceed at the same time it is formed and therefore it will not be observed by X-ray diffraction. It is also possible that other processes play a minor role. It is difficult to know if there is any effect due to the initial differences in powder sizes. We might think that since reactions occur at interfaces, small sizes would favor increased reaction rates. However we expect that the continuous process of cold welding and fracture of powder particles will rapidly reduce these differences.

Figure 6-2. Scanning electron micrograph of the powder milled 3 hours.

a)



b)



The fact that  $\text{Bi}_2\text{O}_3$ ,  $\text{SrO}$ , and  $\text{CaO}$  react more readily than  $\text{CuO}$  is to be expected if one looks at the formation enthalpies of the four oxides (table 6-3 below). In these oxides, the negative oxygen ions act as a bond between positive metallic ions. We see that copper oxide has the lowest enthalpy of formation and, therefore, the least effective metal-oxygen bond. This is consistent with our observations in scanning microscopy where copper oxide seems to react less than other oxides.

Table 6-3. Enthalpies of formation and melting points of the metallic oxides.

oxide	enthalpy of formation	melting point
$\text{Bi}_2\text{O}_3$	-574,26 kJ/mol	825 K
$\text{SrO}$	-592,4 kJ/mol	2430 K
$\text{CaO}$	-635,51 kJ/mol	2614 K
$\text{CuO}$	-157,4 kJ/mol	1326 K

The reaction between the elemental oxides is also observed by X-ray diffraction (figures 6-3a and 6-3b). Again, the slow decrease in the intensities of the  $\text{CuO}$  peaks indicates that  $\text{CuO}$  reacts less than the other oxides during the first few hours of the process.  $\text{Bi}_2\text{O}_3$  seems to react rapidly. There is no significant peak shifting during milling. After 48 hours of milling we are left with an amorphous matrix and copper oxide nanocrystals. The sample has two amorphous haloes in its X-ray diffraction pattern close to 30 and 50 degrees. This is comparable with materials made by rapid solidification. In the X-ray pattern of the sample milled 3 hours, there seems to be a peak at  $30^\circ$  superposed to the amorphous halo. This would be the most intense peak of the bcc solid solution, described later in the text. The crystallite size of copper oxide evaluated from the

6-3a. X-ray diffraction patterns of ball-milled samples.

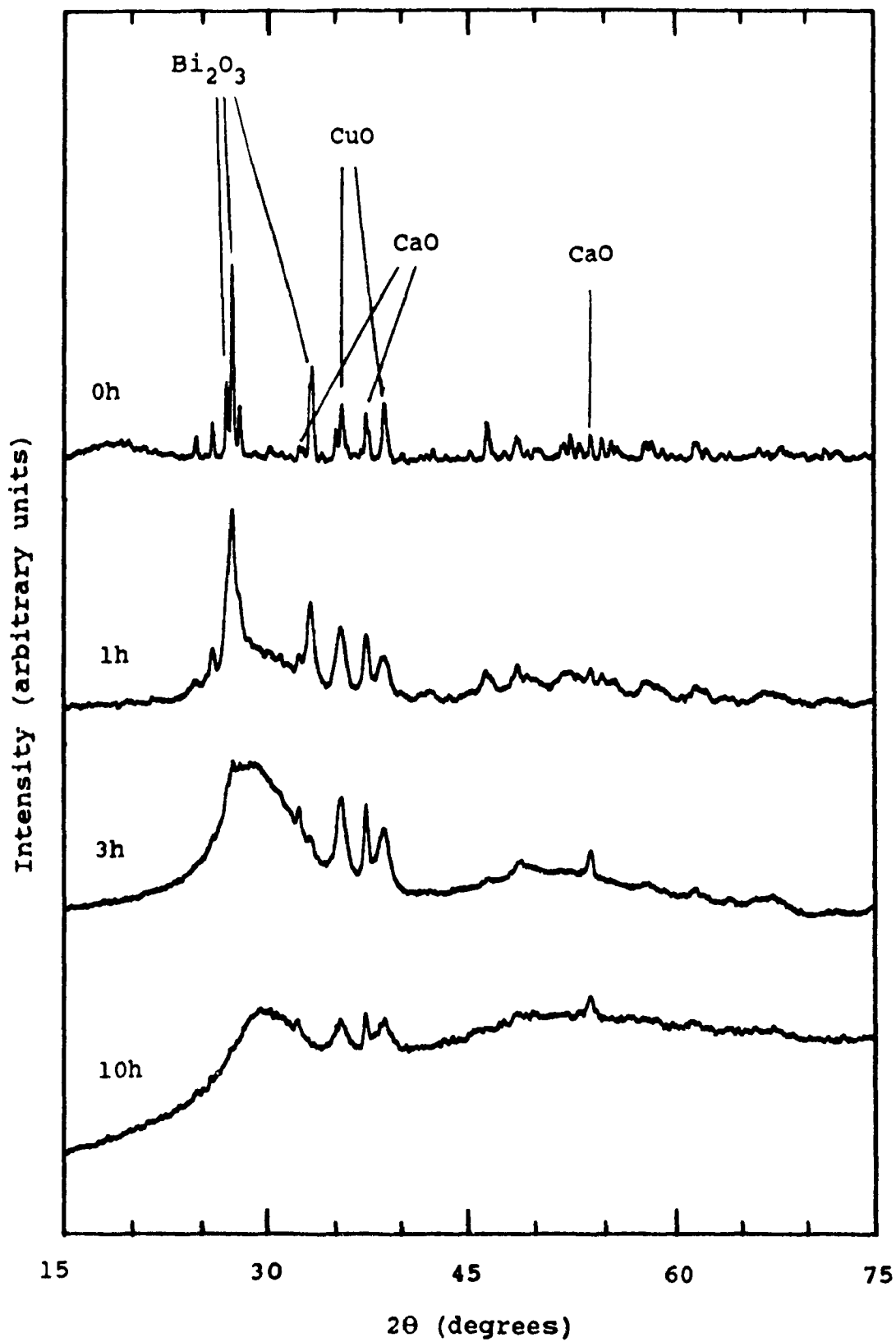


Figure 6-3b. X-ray diffraction patterns of ball-milled samples.

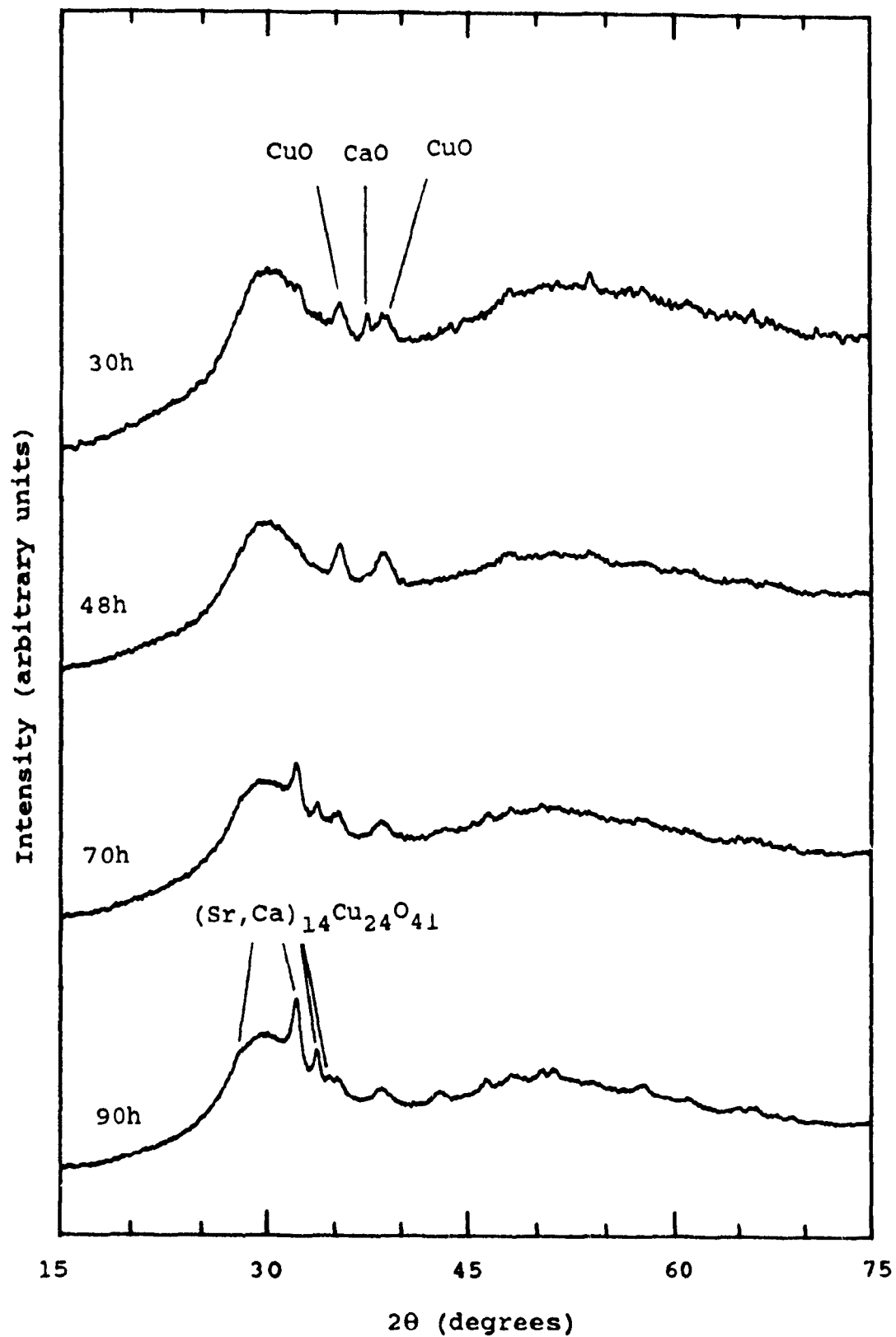


Table 6-4. Crystallite size of copper oxide during milling  
(not corrected for the contribution of strain).

milling time (hours)	crystallite size (nm)
0	36
1	10
3	11
10	6,1 <sup>1</sup>
30	5,3 <sup>1</sup>
48	8,5
70	5,2
90	4,9

<sup>1</sup> underestimated because of strain

broadening of the X-ray peaks is 8,5nm after 48 hours of milling. In table 6-4 we see that there is an apparent increase in the crystallite size of copper oxide. This is because without a sufficient number of peaks, we could not take into account the broadening due to the strain. Below a critical crystallite size, the strain is released, the peaks become sharper and this causes an apparent size increase. This is what is observed for copper oxide. There is an initial size refinement during the first hours of milling. Between 30 and 48 hours the strain is released when the crystal size is around 10nm. Beyond this point the CuO crystallites are strain free and this lowers its tendency to react with the rest of the matrix since it is known that strain is an important factor in solid state reactions caused by mechanical deformations [62]. Upon further milling (70 and 90 hours), the precipitation of a complex phase which could be identified as  $(\text{Sr,Ca})_{14}\text{Cu}_{24}\text{O}_{41}$  is observed. The structure is described in detail in references [45,71]. The precipitation

of a crystalline phase in the latter stage of the process was to be expected since the 2223 composition lies outside of the glass-forming range of the Bi-Sr-Ca-Cu-O system [91]. As copper oxide is forced to dissolve into the amorphous matrix, its composition gradually moves out of the glass-forming range.

The rapid reaction between  $\text{Bi}_2\text{O}_3$  and  $\text{CaO}$  at the beginning of the process can be observed by milling the Bi-Ca-O subsystem (figure 6-4). We used a starting mixture of  $\text{Bi}_2\text{O}_3+2\text{CaO}$ . After an initial size refinement (as seen from peak broadening) a new peak appears at 30 degrees after 1 hour of milling. As milling continues, all the bismuth and calcium oxide reacts to form the new phase. This phase is a body-centered cubic solid solution of the metallic atoms. This phase is a high-temperature phase present in the phase diagram of the Bi-Ca-O pseudo-binary system [11]. The measured lattice parameter is 0,423nm. The Bi and Ca atoms are randomly distributed on the (0,0,0) and (1/2,1/2,1/2) sites. The location of the oxygen atoms is still unknown.

Since we know from scanning microscopy that  $\text{Bi}_2\text{O}_3$ ,  $\text{SrO}$ , and  $\text{CaO}$  react together in the first few hours of milling we also expect Sr to be in solution with the Bi and the Ca in this cubic phase. In fact, a bcc solid solution has also been observed close to the melting point in the Bi-Sr-O subsystem [24]. We have milled a mixture  $(\text{Bi}_2\text{O}_3+2\text{CaO})+2\text{SrO}$  for 20 hours (figure 6-5). The resulting X-ray pattern indicates that we get an amorphous phase with the main broad halo located just below  $30^\circ$ . In the phase diagram of the Bi-Ca-O system, the bcc solid solution coexists with a second phase for the compositions with a Ca/Bi ratio above one. Treating Sr and Ca as roughly equivalent, we have therefore an excess Sr or Ca at the  $\text{Bi}_2\text{Sr}_2\text{Ca}_2$  composition. The cubic solid solution would be oversaturated and unstable. The difference in ionic radius between Sr and Ca adds to the instability of the crystalline solid solution. At some point, the addition

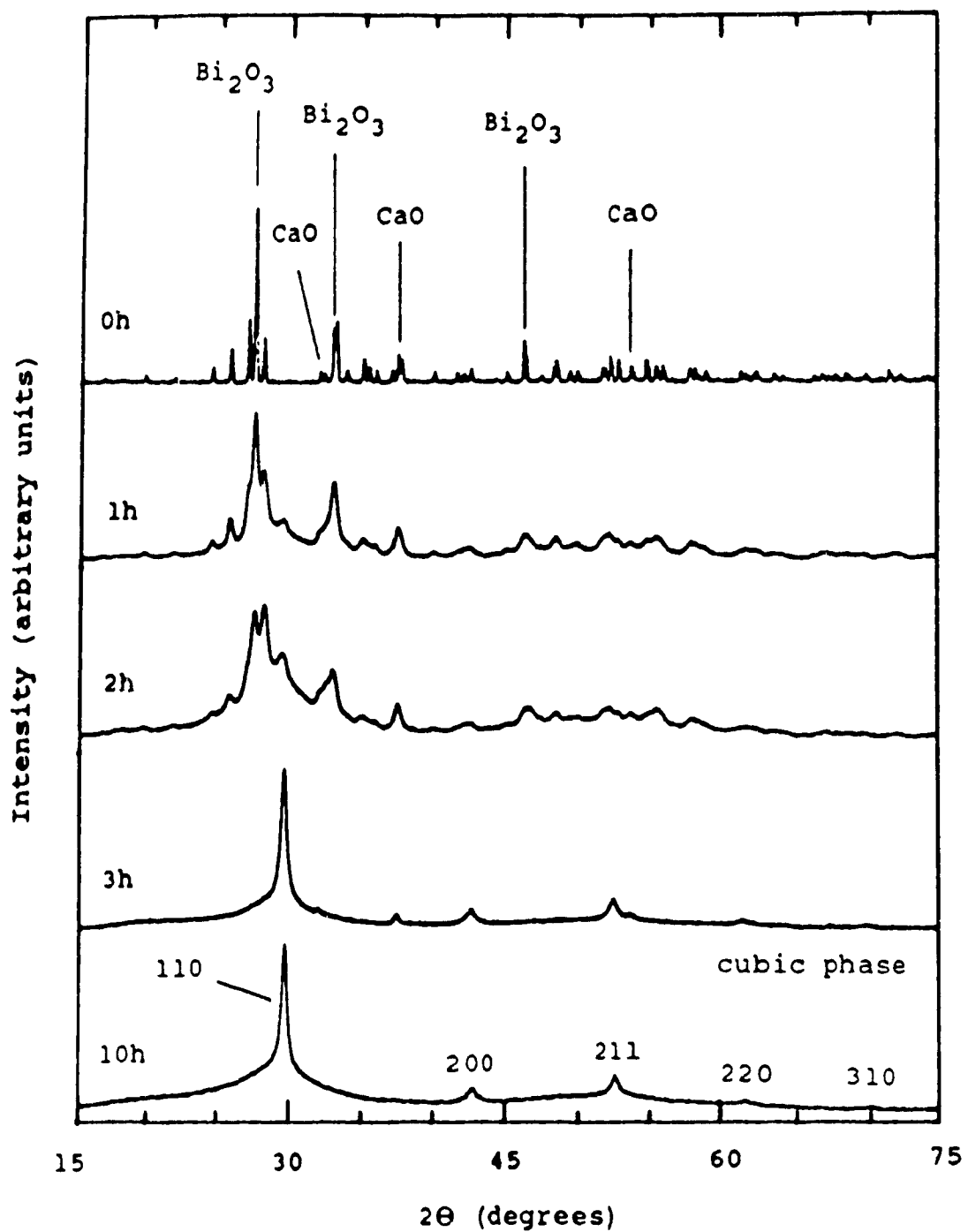
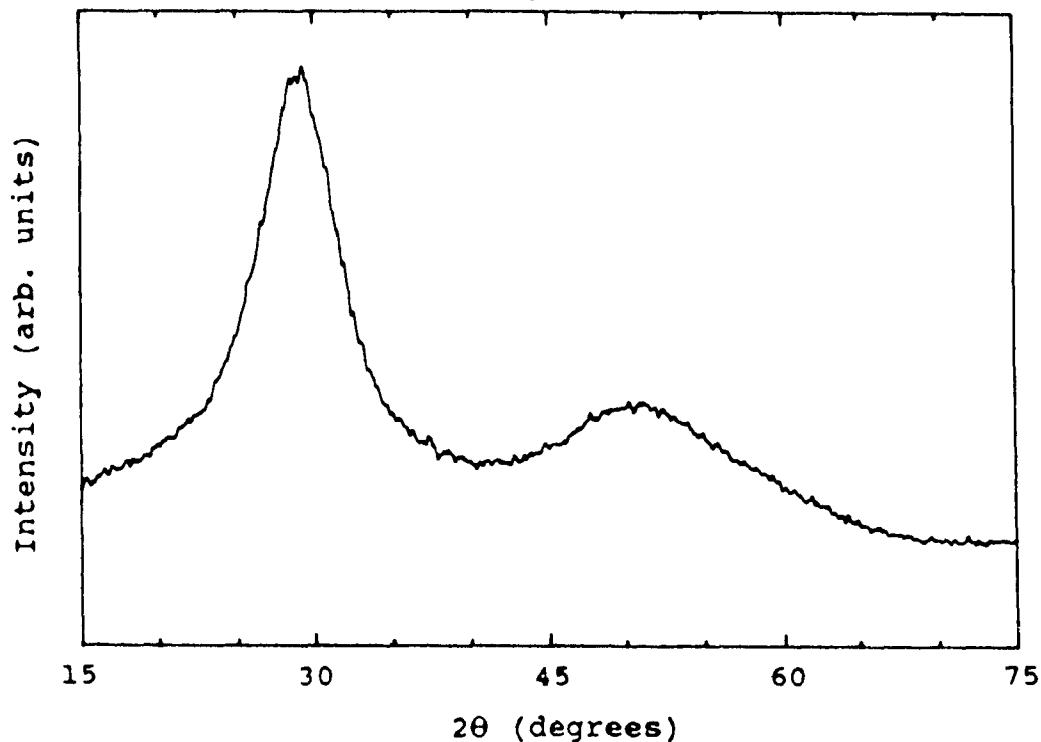
Figure 6-4. X-ray patterns of  $\text{Bi}_2\text{O}_3+2\text{CaO}$  for various milling times.

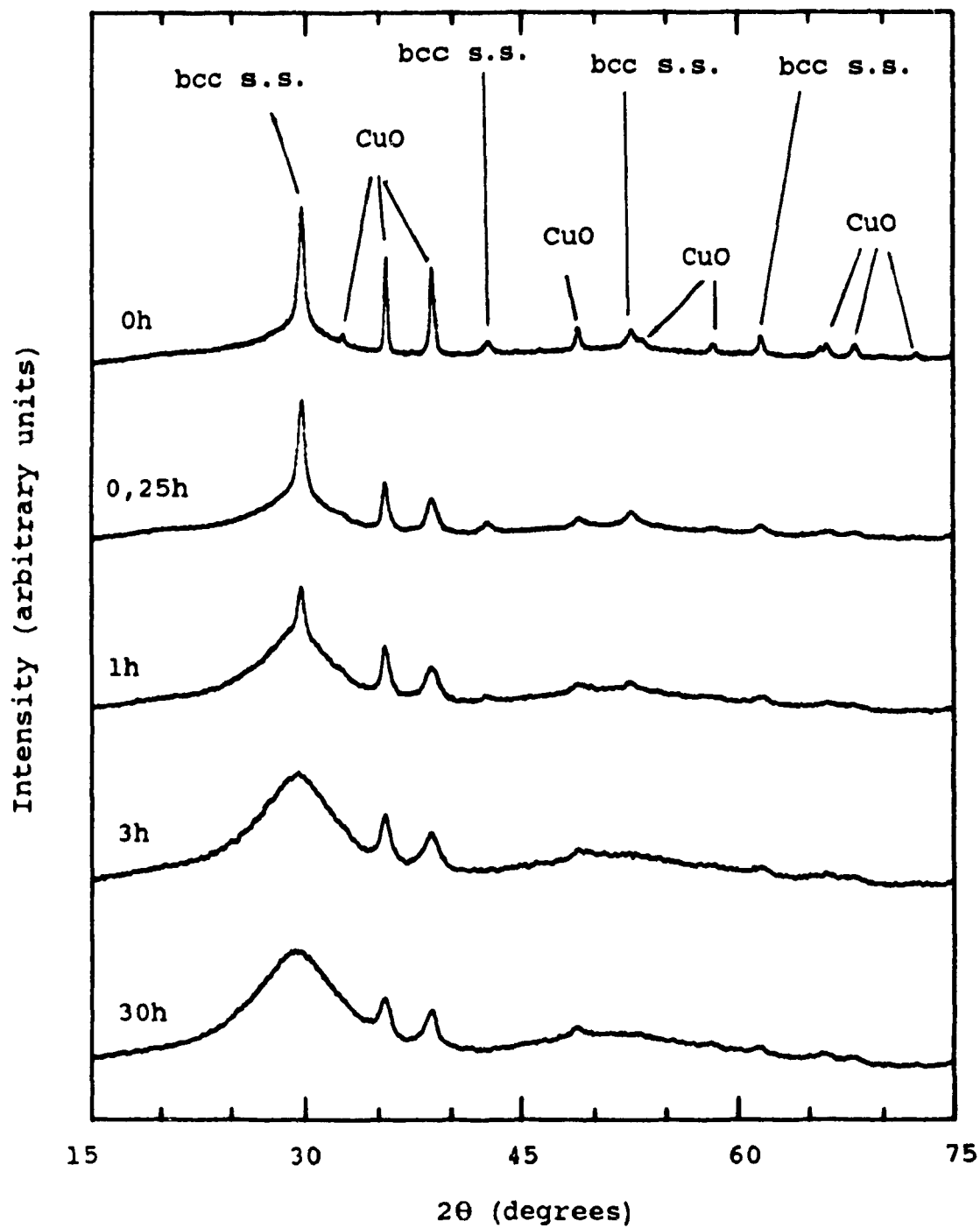
Figure 6-5. X-ray patterns of  $(\text{Bi}_2\text{O}_3+2\text{CaO})+2\text{SrO}$  milled 20 hours.



of more Sr (probably together with the presence of defects caused by mechanical deformation) seems to drive the free energy of the solid solution above that of the amorphous Bi-Sr-Ca-O phase.

The other reaction which may occur during the milling process is one in which the cubic solid solution reacts with copper oxide, leading to the amorphous phase. This is supported by another experiment in which we have used a mixture of the cubic phase and copper oxide (figure 6-6). For the cubic phase we have used the sample milled 10 hours in the Bi-Ca-O subsystem. The ratio for Bi-Ca-Cu was 1:1:1. The X-ray diffraction of the samples milled for various periods of time shows that the reaction is very fast. After 15 minutes of milling a substantial amount of amorphous phase is formed. After 3 hours the peaks corresponding to the bcc solid solution are no longer visible. In this case also, copper oxide remains present after 30 hours of milling. The X-ray spectrum is then very similar to the one observed in Bi-Sr-Ca-Cu-O after 48 hours of milling.

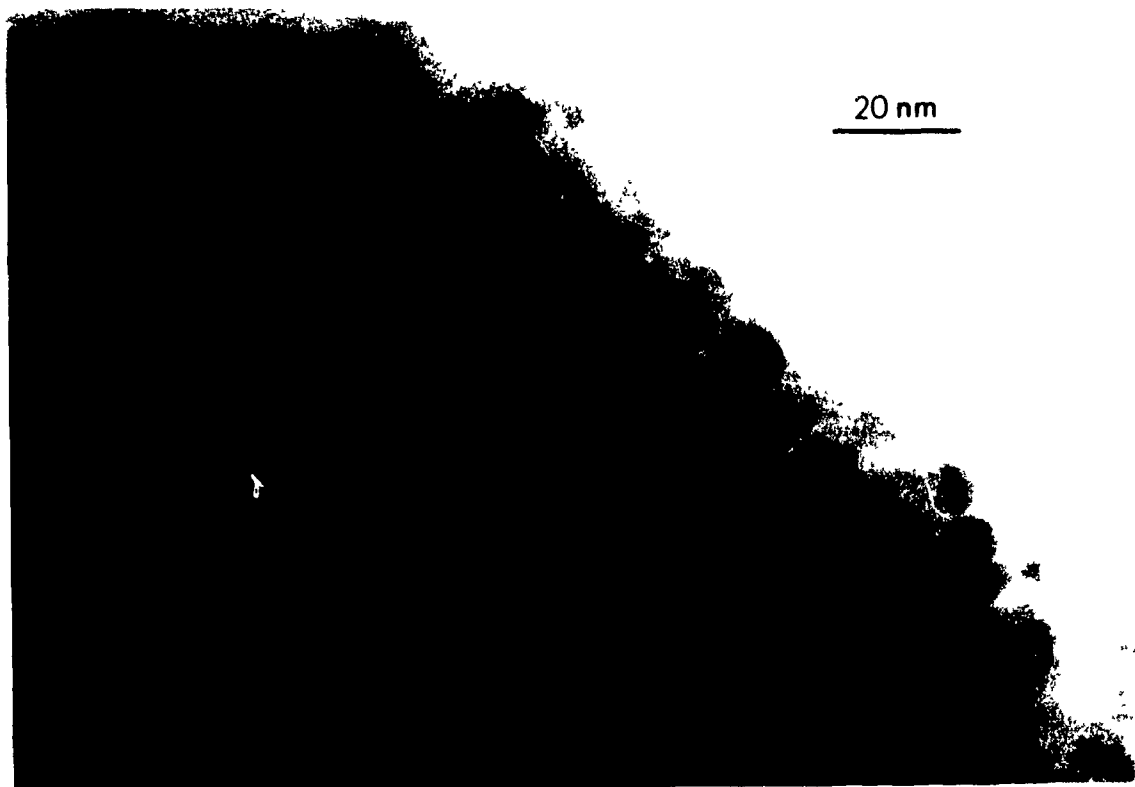
Figure 6-6. X-ray patterns for the ball milling of the mixture:  
bcc solid solution (B1-Ca-O) + CuO.



Direct observation in TEM (transmission electron microscopy) of the four oxides mixture reveals small precipitates (5-10nm) embedded in an amorphous matrix (see figure 6-7 below). When the electron beam is focused for EDX analysis, no composition difference is observed between the amorphous matrix and the precipitates, most likely because of their small size. These precipitates are also too small to allow structural identification by means of electron diffraction. According to the X ray diffraction, however, they should be CuO and  $(\text{Sr,Ca})_{14}\text{Cu}_{24}\text{O}_{41}$  crystallites.

The ball milling experiments described previously were repeated with tungsten carbide balls and vials to rule out any effect from iron impurities. The results were the same as those obtained with steel equipment.

Figure 6-7. TEM picture of four oxides mixture milled 90 hours.



## 6.2. Thermal Treatments.

### 6.2.1. Annealing in Argon.

DSC (figure 6-8) experiments performed in an argon atmosphere on samples milled 48 hours in an argon atmosphere reveal two exothermic reactions at 748K and 868K and a sharp endothermic peak immediately following the first exotherm. They are superposed on a large endothermic background. The enthalpies corresponding to the exotherms are 5,2J/g and 16,2J/g. The first peak corresponds to the crystallization of the bcc solid solution. The second peak corresponds to the transformation of the above-mentioned phase into the 2201 phase, necessarily involving the diffusion of copper into the cubic phase as it transforms. TGA (figure 6-9) reveals a weight loss from 475K to the crystallization temperature. This weight loss corresponds to the large endothermic background apparent on the DSC scan. This is most likely related to the loss of oxygen. The average weight loss just before crystallization amounts to 1,4% which corresponds to the loss of one oxygen for the  $B_{12}Sr_2Ca_2Cu_3O_{10}$  composition. Between the two exothermic transformations however there is an increase in weight due to an oxygen uptake (probably because of some oxygen impurities in the sample chamber). As the temperature is raised to the melting point (around 1075K) further weight loss occurs.

The crystallization temperature and transformation enthalpies of both phase transitions (especially the first one) were poorly reproducible. Better reproducibility was obtained by annealing the samples at 700K for 1 hour. In those cases, the TGA curve shows no significant loss of weight prior to crystallization (see figure 6-11). In the DSC curve (see figure 6-10) the wide endotherm is largely reduced. The crystallization temperature is now 772K (maximum). The enthalpy is 3.0J/g. The sharp endothermic peak at 763K seems to be related to the first

Figure 6-8. DSC scan of sample milled 48 hours  
(rate: 20K/min).

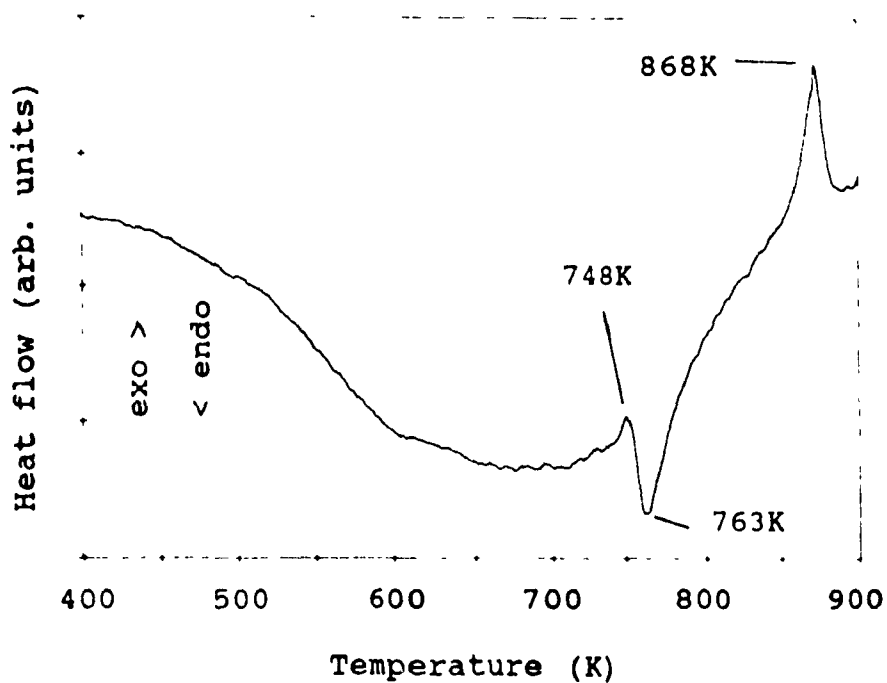


Figure 6-9. TGA scan of sample milled 48 hours  
(rate: 20K/min).

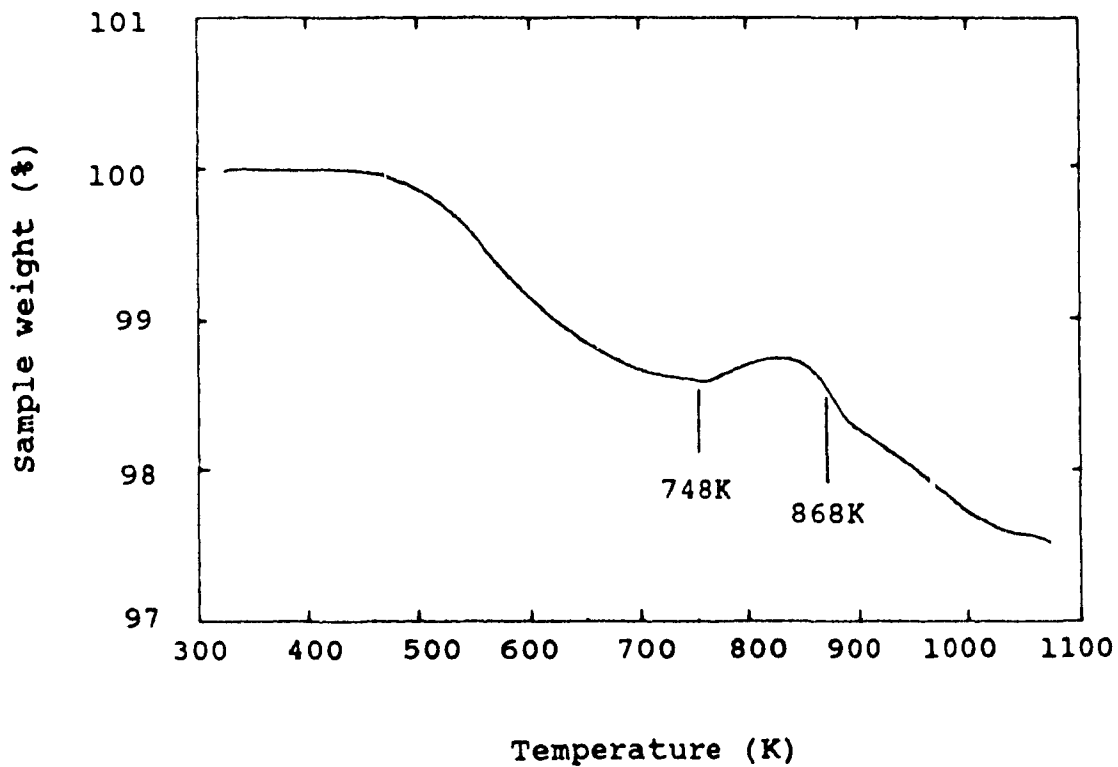


Figure 6-10. DSC scan of sample annealed 1 hour at 700K in argon (rate: 20K/min).

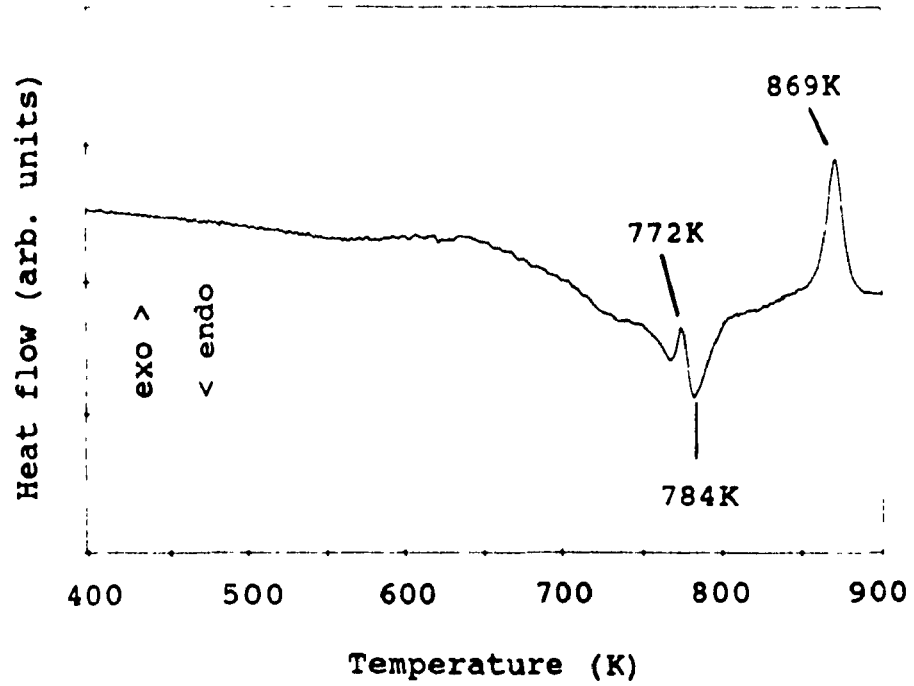
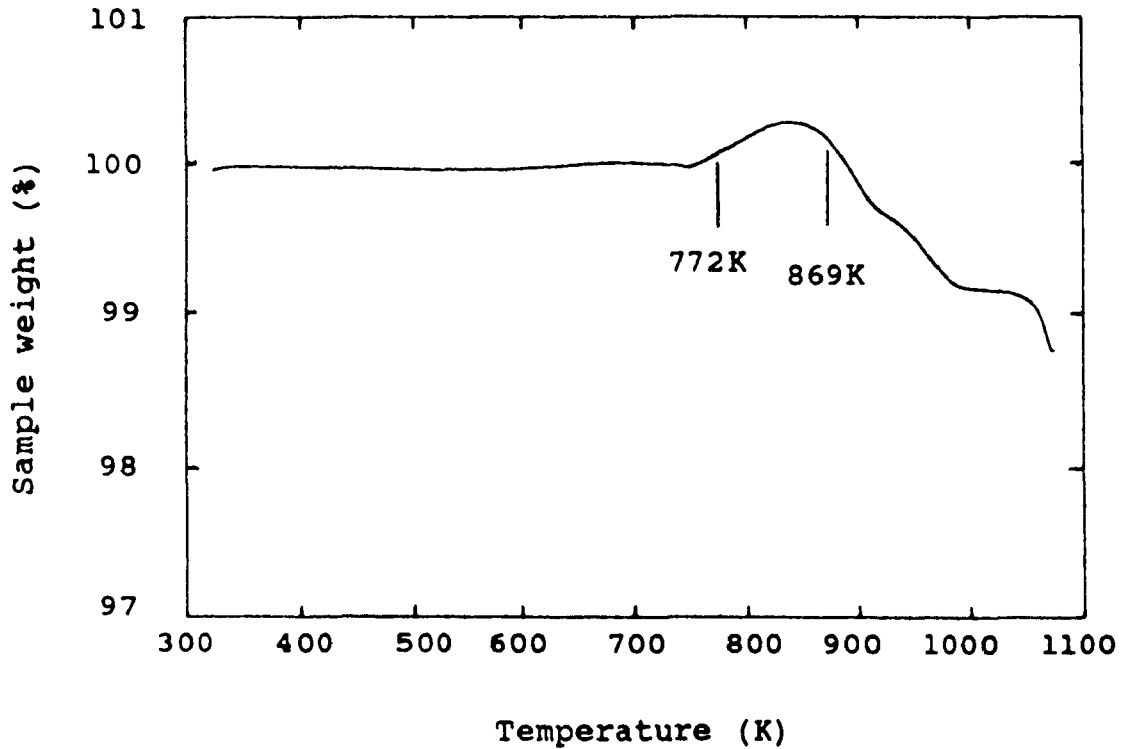


Figure 6-11. TGA scan of sample annealed 1 hour at 700K (rate: 20K/min).



crystallization event since they shift by nearly the same temperature after thermal treatment. This endotherm may be related to an increase in the heat capacity of the sample after crystallization. The second transformation for the pre-annealed sample occurs at 869K, approximately the same temperature as for the as-milled sample. We have also obtained a Kissinger plot [10] for the second exothermic peak (figure 6-12). The activation energy is 730kJ/mol or 7,6eV. This is comparable to activation energies encountered in these oxide systems [52]. Samples heated to 800 and 1000K (after the first and second exotherms) are shown on figures 6-13 and 6-14.

Figure 6-12. Kissinger plot for the second transformation.

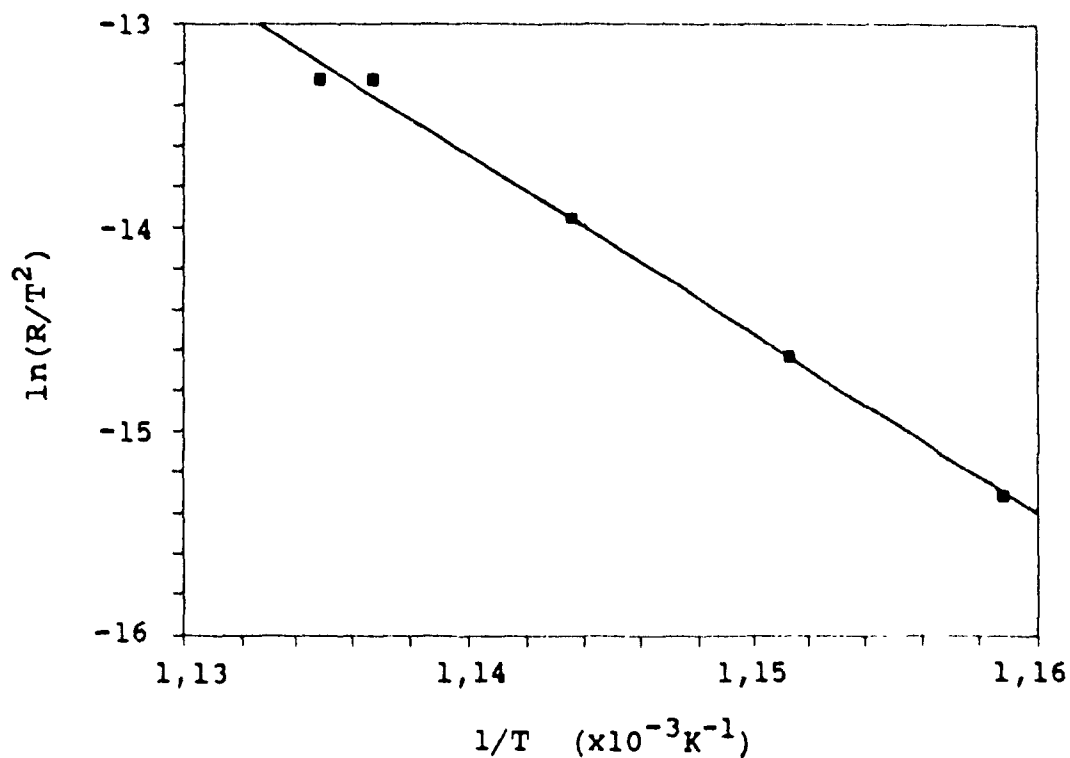


Figure 6-13. X-ray diffraction pattern of a 48h milled sample heated to 800K in argon at 20K/min.

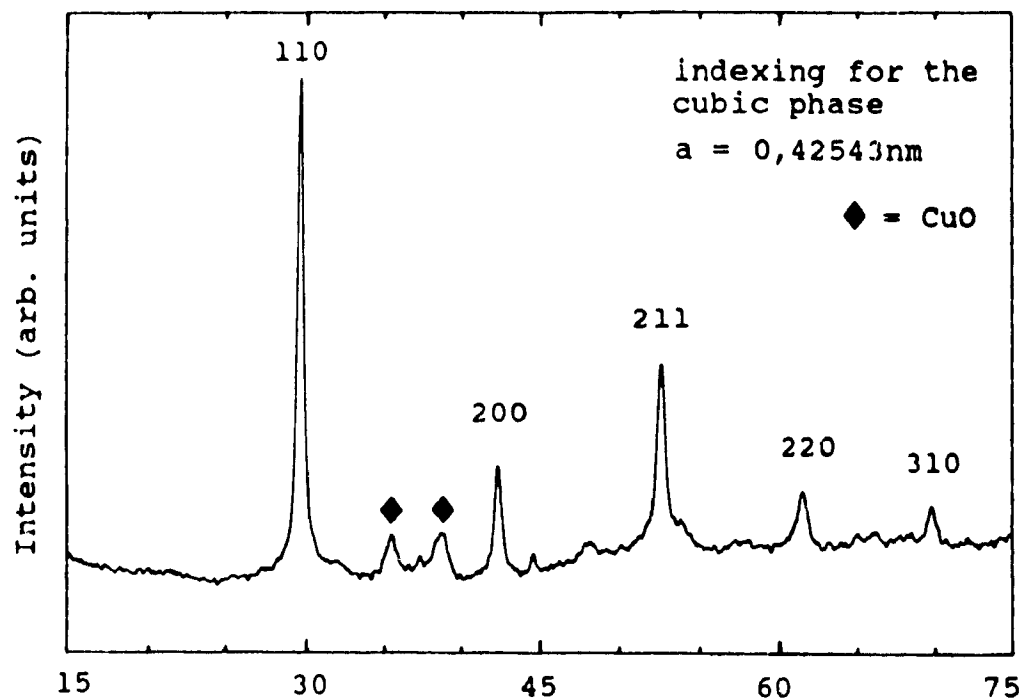
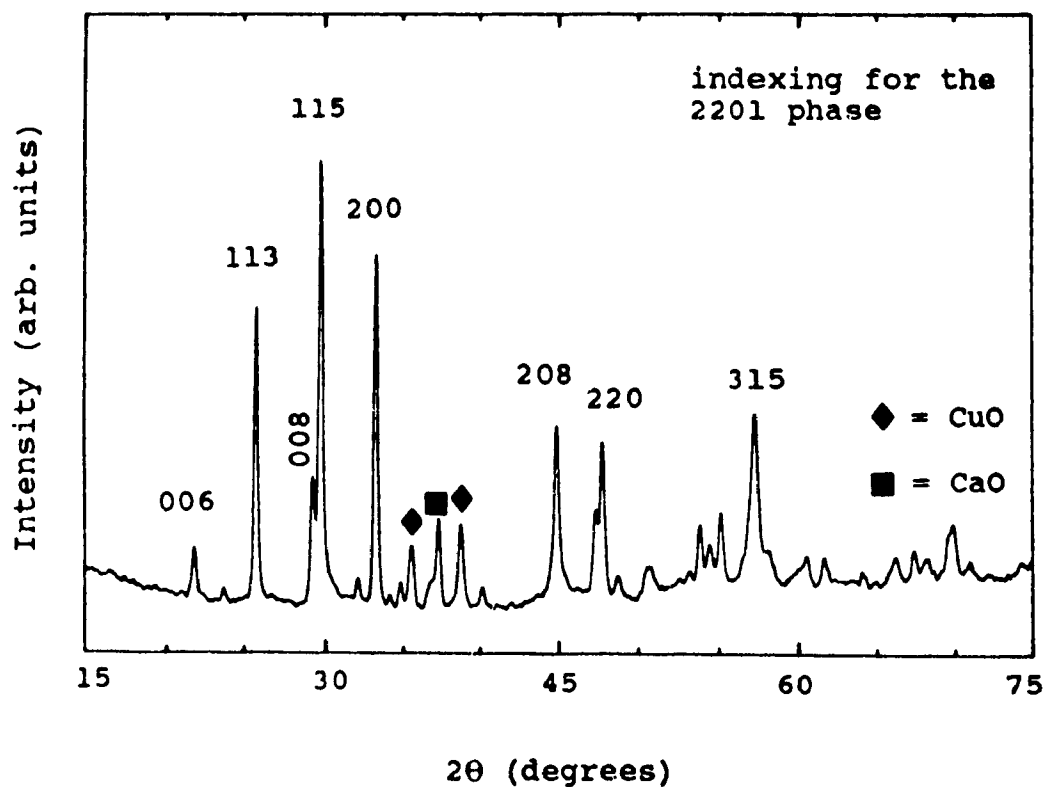


Figure 6-14. X-ray diffraction pattern of a sample heated to 1000K in argon at 20K/min.



We have also performed DSC scans on the  $\text{Bi}_2\text{O}_3+2\text{CaO}$  sample milled 20 hours. The first exotherm is at 743K and the enthalpy is 5,0J/g (figure 6-15). These values are very close to those of the first exotherm in the Bi-Sr-Ca-Cu-O system. This transition is associated to the recrystallization or the grain growth of the cubic phase. During recrystallization, the crystallite size increases from 20 to 40nm. The second DSC peak corresponds to a transition to an ordered phase, probably isostructural to the rhombohedral  $\text{Sr}_3\text{Bi}_2\text{O}_6$  [38]. The transition temperature is 863K, the enthalpy 23J/g, and the activation energy 560kJ/mol or 5,8 eV (figure 6-16). This last value is smaller than the corresponding one in the quaternary Bi-Sr-Ca-Cu-O system. The X-ray patterns of these samples heated to 800 and 1000K are shown on figure 6-17. We see, in the second pattern, the peaks corresponding to the bcc solid solution, and in the

Figure 6-15. DSC scan of the  $\text{Bi}_2\text{O}_3+2\text{CaO}$  sample milled 20 hours (rate: 20K/min).

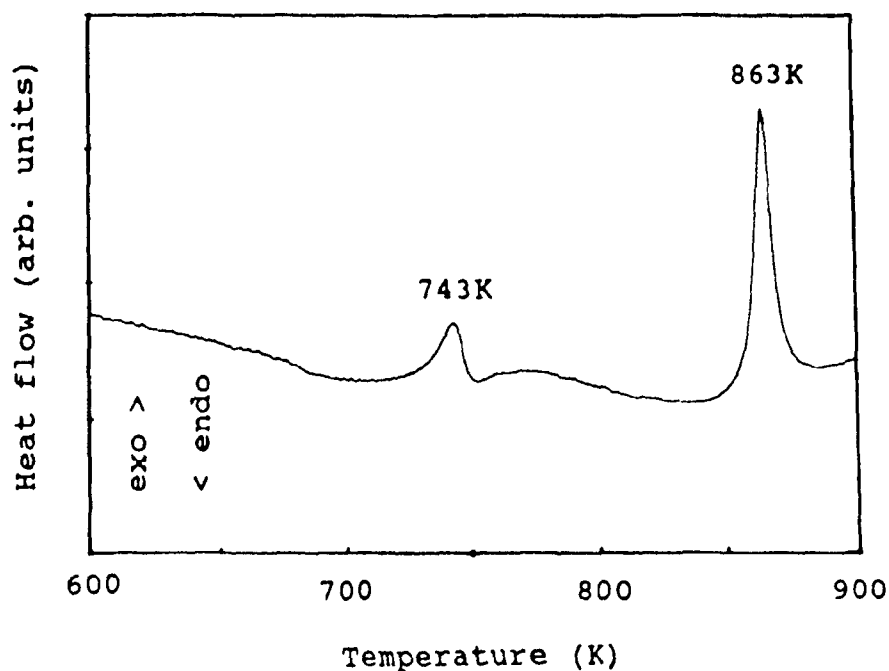
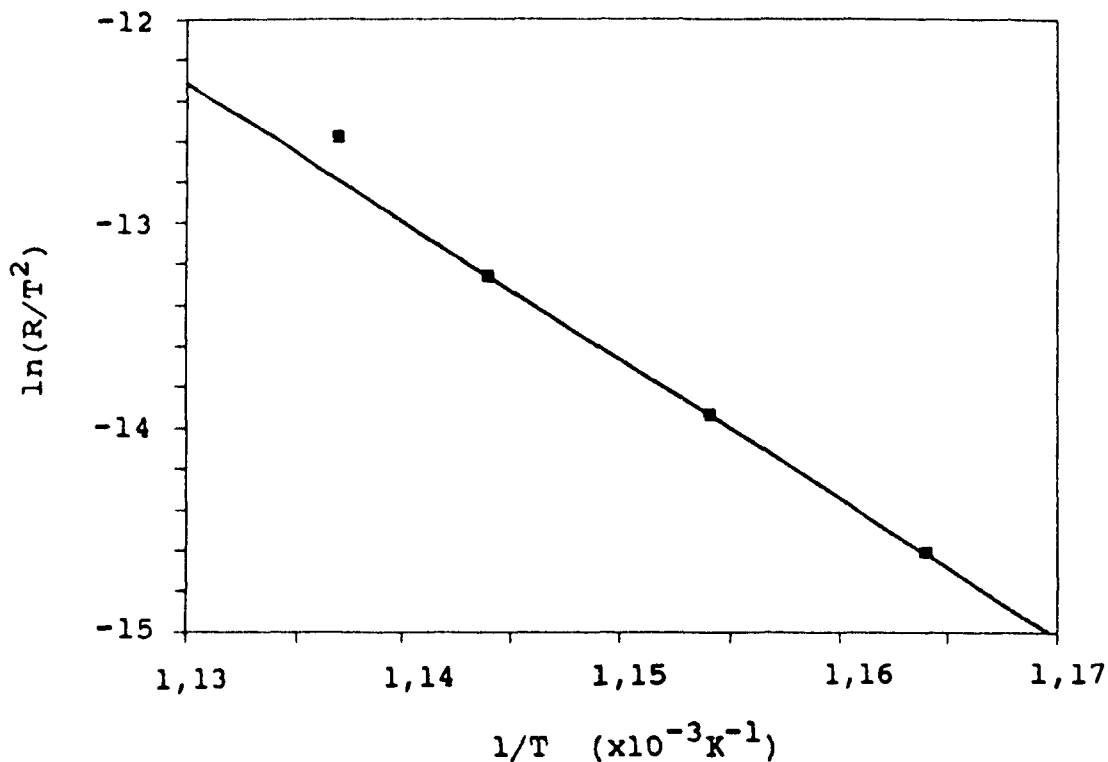


Figure 6-16. Kissinger plot for the second transformation in the Bi-Ca-O subsystem.



third one, the peaks of the more complex rhombohedral structure. From these experiments, we conclude that the first peak present in the DSC curves of both the Bi-Sr-Ca-Cu-O and the Bi-Ca-O systems corresponds to a transition into a similar microstructure. Also in the Bi-Sr-Ca-Cu-O system, the cubic phase transforms into the 2201 structure nearly at the same temperature that the Bi-Ca-O cubic phase undergoes a transition to the rhombohedral structure. In order to verify whether some copper is in solution with the three other elements in the cubic phase, we have used our  $(\text{Bi}_2\text{O}_3+2\text{CaO})+2\text{CuO}$  sample milled 30 hours and crystallized by heating to 800K in argon. We have also heated the Bi-Sr-Ca-O sample milled 20 hours to 700K. The corresponding X-ray patterns are shown on figures 6-18 and 6-19 respectively. Both give rise to the formation of the cubic phase.

In the Bi-Ca-Cu-O system however there is, apart from CuO, a small amount of an unidentified second phase. Table 6-5 summarizes the results for the metastable cubic phases.

Figure 6-17. X-ray diffraction patterns of  $\text{Bi}_2\text{O}_3+2\text{CaO}$  milled 20 hours and of samples subsequently heated to 800 and 1000K in argon at 20K/min.

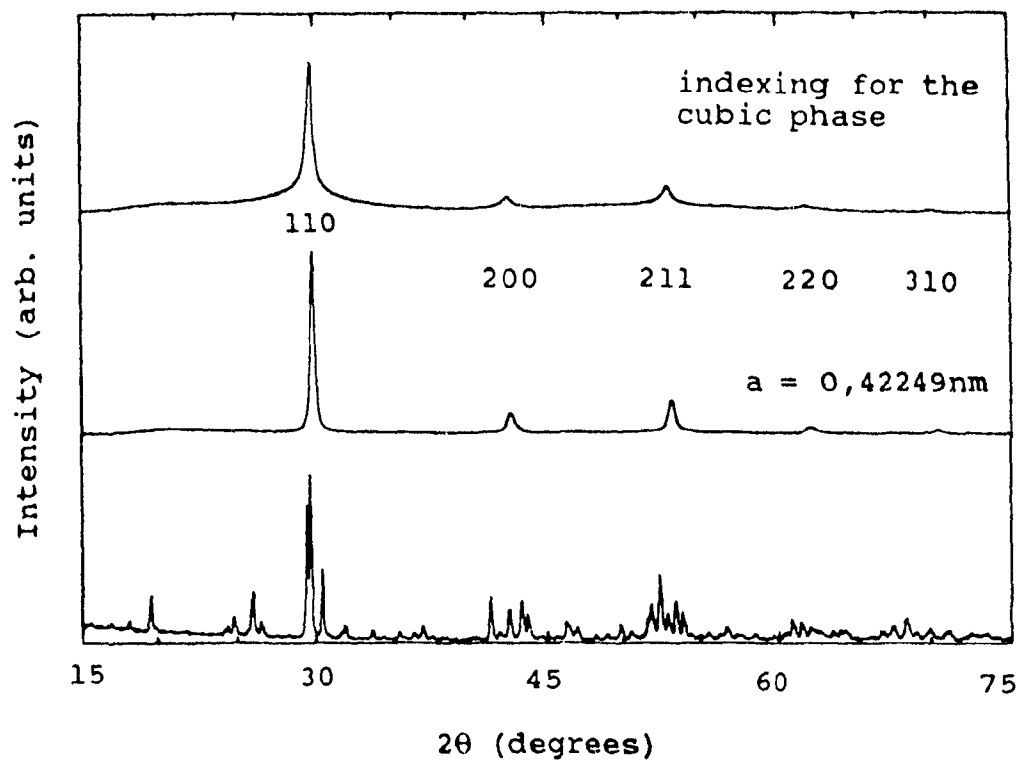


Figure 6-18. X-ray pattern of Bi-Ca-Cu-O milled 30 hours and heated to 800K at 20K/min in argon.

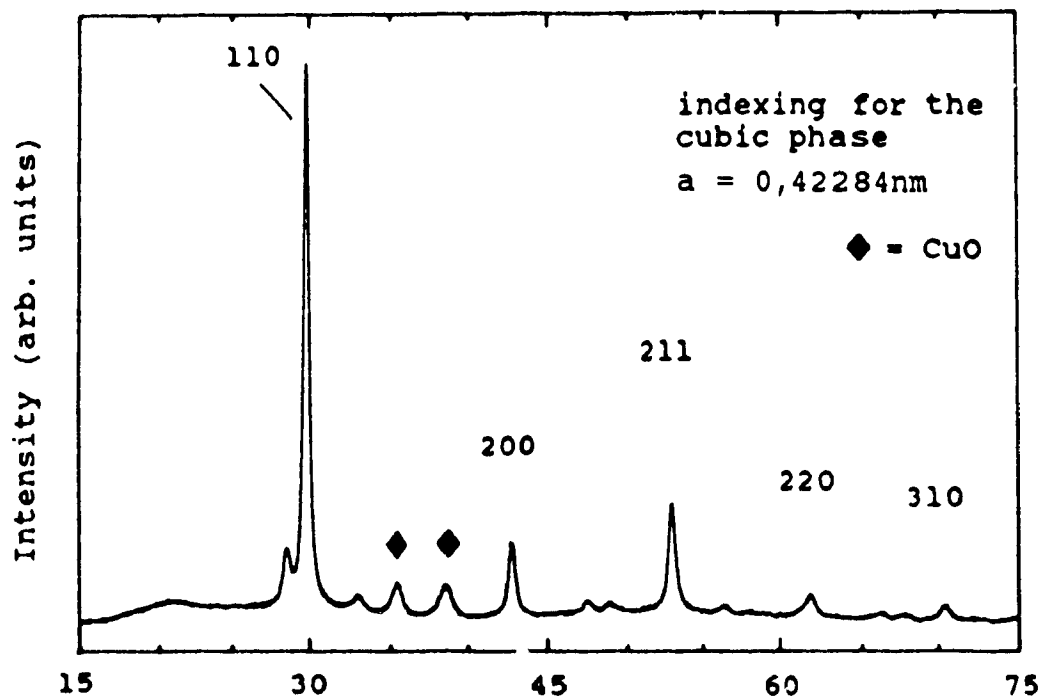


Figure 6-19. X-ray pattern of Bi-Sr-Cu-O milled 20 hours and heated to 700K at 20K/min in argon.

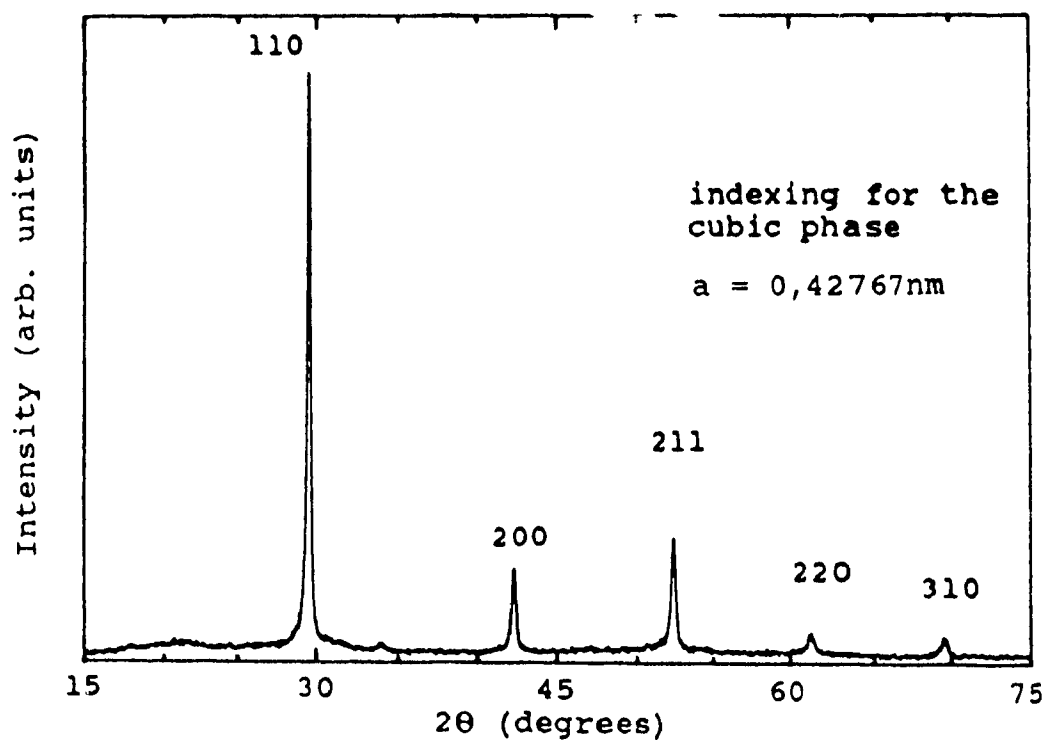


Table 6-5. X-ray peak intensities and lattice parameters for the bcc solid solution formed in various samples.

system	lattice parameter (nm)	experimental X-ray peak intensities						
		110	200	211	220	310	222	321
a) Bi-Ca-O	0,42249	100,0	18,4	28,1	16,1	5,2	1,1	4,4
b) Bi-Sr-Ca-O	0,42767	100,0	17,7	25,8	5,2	5,2	0,0	4,1
c) Bi-Ca-Cu-O	0,42284	100,0	16,1	25,9	4,4	4,1	0,5	3,5
d) Bi-Sr-Ca-Cu-O	0,42543	100,0	26,8	46,7	17,7	10,9	4,1	10,5

The X-ray peak intensities and lattice parameters for the various systems are given. The first observation to make is that when the cubic solid solution contains strontium (b versus a), the lattice parameter is larger (4,2767 versus 4,2249) because the Sr atoms have a larger ionic radius than those of calcium and bismuth (0,112nm for  $\text{Sr}^{+2}$  compared to 0,099nm for  $\text{Ca}^{+2}$  and 0,096nm for  $\text{Bi}^{+3}$ ). The fact that the lattice parameter and the X-ray intensities are practically identical for experiments c and a suggests that Cu is not present in the cubic phase obtained by annealing the Bi-Ca-Cu-O milled sample. Finally it seems that Cu may be involved in the structure of the cubic phase in the case of the quaternary system (d). This conclusion comes from the difference in the lattice parameter and the analysis of X-ray intensities. We hypothesize that the inclusion of copper into the structure brings changes in the oxygen sublattice and that these changes are responsible for the weakening of the 110 reflection with

respect to the reflections at higher angles. Calculations show that changes in the average scattering factor at the  $(0,0,0)$  and  $(1/2,1/2,1/2)$  sites, due to changes in composition, do not bring any major modifications in peak intensities (see table 15 in the appendix). The changes in the observed intensities must therefore come from modifications in the positions of the oxygen atoms. This is to be expected if copper is part of the metastable cubic structure since certain copper-oxygen coordinations are unstable [55].

Therefore the sequence of reaction during the annealing of the milled Bi-Sr-Ca-Cu-O system may be as follow. First, the amorphous phase crystallizes into a Bi-Ca(Sr)-O cubic solid solution of containing copper. In the second transformation, the cubic phase transforms into the 2201 structure, rather than in a Bi-Ca(Sr)-O rhombohedral structure because of the presence of copper.

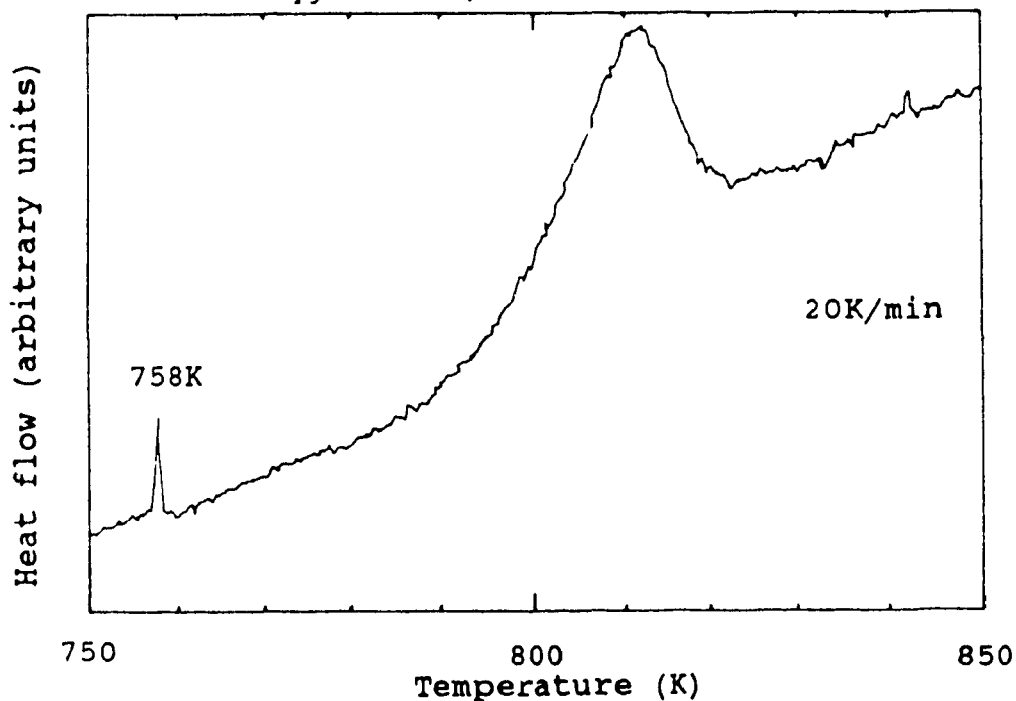
### 6.2.2. Annealing in Oxygen.

Because of possible damage to the DSC we were unable to carry out extensive DSC experiments using oxygen as a purging gas. Nevertheless, some scans were done as shown in figure 6-20. The figure shows a small and very sharp crystallization peak in the same temperature range as the one observed in argon and a large and broad exotherm around 810K which we suspect to be due to the presence of oxygen. Subsequent X-ray diffraction experiments reveal that this broad peak corresponds to the formation of an hexagonal phase. A final transition (above the maximum temperature of our DSC scan) leads to the formation of the 2201 phase.

On figure 6-21, the X-ray patterns of three heated samples are shown. The first one has been heated to 800K at 20K/min, the second one has been annealed at that temperature for 1 hour, and the third one has been further heated to 1000K at 20K/min.

The first diffraction pattern reveals the presence of two phases. The first one is the bcc phase discussed in the previous section, and the second is an hexagonal phase with a structure very close to the bcc structure. The 100 peak of the hexagonal phase is the peak at  $17,63^{\circ}$ . The lattice parameters are  $a = 0,58057\text{nm}$  and  $c = 0,35551\text{nm}$ . The a, b, and c axes are respectively along the  $\langle 1\ 1\ 1 \rangle$ ,  $\langle 1\ 0\ -1 \rangle$ , and  $\langle 0\ 1\ -1 \rangle$  directions of the approximately equivalent cubic lattice. We have not yet found a satisfactory model for the exact crystal structure. Reaction of the cubic phase with oxygen in the temperature range corresponding to the second DSC peak may produce a distortion of the cubic lattice and give rise to the formation of this hexagonal phase. The presence of the 100 peak indicates that there is some ordering among the sites of the metallic atoms in that structure.

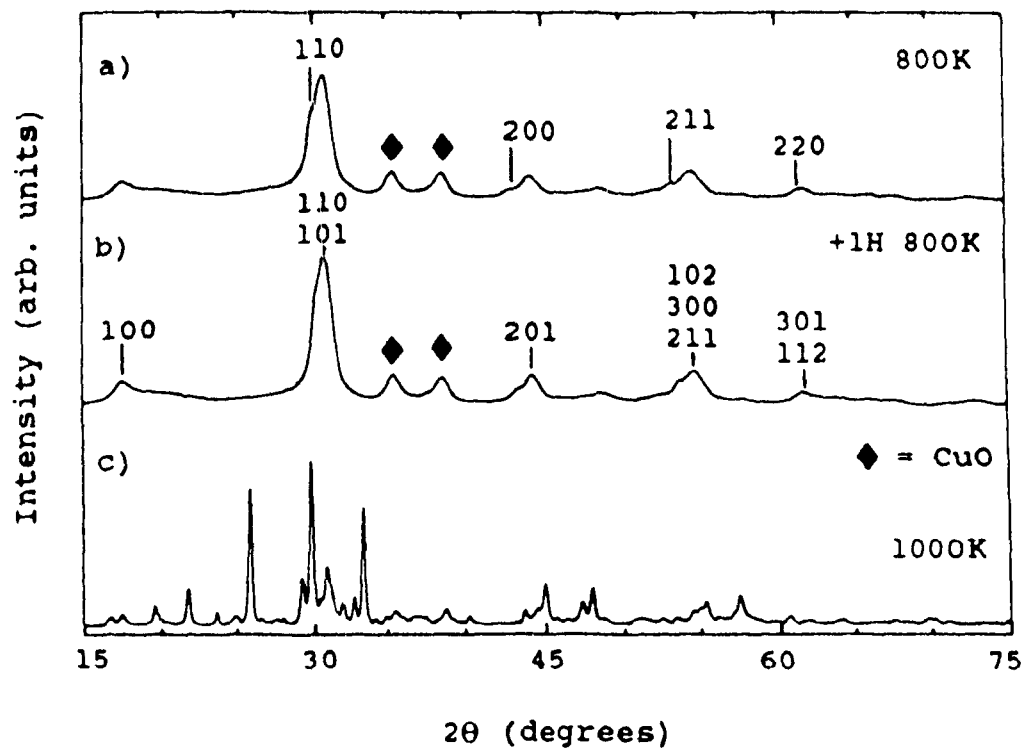
Figure 6-20 DSC scan of the Bi-Sr-Ca-Cu-O sample milled 48 hours in oxygen at 20K/min.



An additional hour at 800K increases the relative amount of the hexagonal phase with respect to the cubic phase. The time scale over which the transformation proceeds is a clear confirmation that this is a diffusional process involving oxygen.

If we then heat the sample to 1000K, we obtain the 2201 structure (figure 6-21c). The presence of oxygen diffusing into the structure has therefore simply added an intermediate step in the sequence of transformations, more precisely: the transformation of the cubic phase into an hexagonal structure. Also, part of the amorphous phase probably transforms directly into the hexagonal phase during the second exothermic reaction, since the enthalpy of the first peak is 1,6J/g, which is less than the crystallization enthalpy of samples treated in argon (3,0J/g). The transformation of the 2201 phase into the 2212 phase is discussed in the next section.

Figure 6-21. X-ray patterns of Bi-Sr-Ca-Cu-O milled 48 hours and heat treated in an oxygen atmosphere.



- a) indexing for the cubic phase  
 b) indexing for the hexagonal phase

### 6.2.3. High-Tc Phase Formation.

There is no other transformation before the melting point of the material. In order to obtain the 2212 phase, it is necessary to hold the material at high temperature in oxygen for some time. The formation of the high-Tc phase (2212) occurs in the first hour when 1125K has been reached. As annealing continues, the crystallite size increases (the X-ray peaks become sharper). After 20 hours at 1125K, the major phase present in the diffraction pattern is the 2212 high-Tc phase as seen on figure 6-22 below. Figure 6-23 is a magnetization experiment. There is a superconducting transition at 108K (see figure 6-24) but the amount of that phase is marginal. In figure 6-24 the moment is positive above 110K because of a small paramagnetic contribution. The main transition has its onset at 82K but the diamagnetic response is important only below 73K. The response of the material reveals that almost all the mass of the material is superconducting, but that interstitial spaces are penetrated by the magnetic field. The ZFC curve is typical of a material in which regions excluding the flux are becoming smaller as the temperature is increased. The curve is flat however below 7K. This suggests that the grains are linked by low-Tc (2201 phase) material. If we calculate precisely the amount of mass which is superconducting by using the theoretical density of the 2212 phase and assuming a fully dense material we obtain 97%. This is an overestimate; our calculation is very approximate and does not account for impurity phases, voids, etc...

### 6.3. Comparison with Materials Prepared by Rapid Solidification.

The amorphous phase we have obtained by ball milling has an X-ray diffraction pattern similar to those of melt-quenched materials. The most intense amorphous halo at 30 degrees is the same, the second one around 50 degrees is also present in some rapidly solidified samples. The main

Figure 6-22. Diffraction pattern of the 85K (2212) phase.

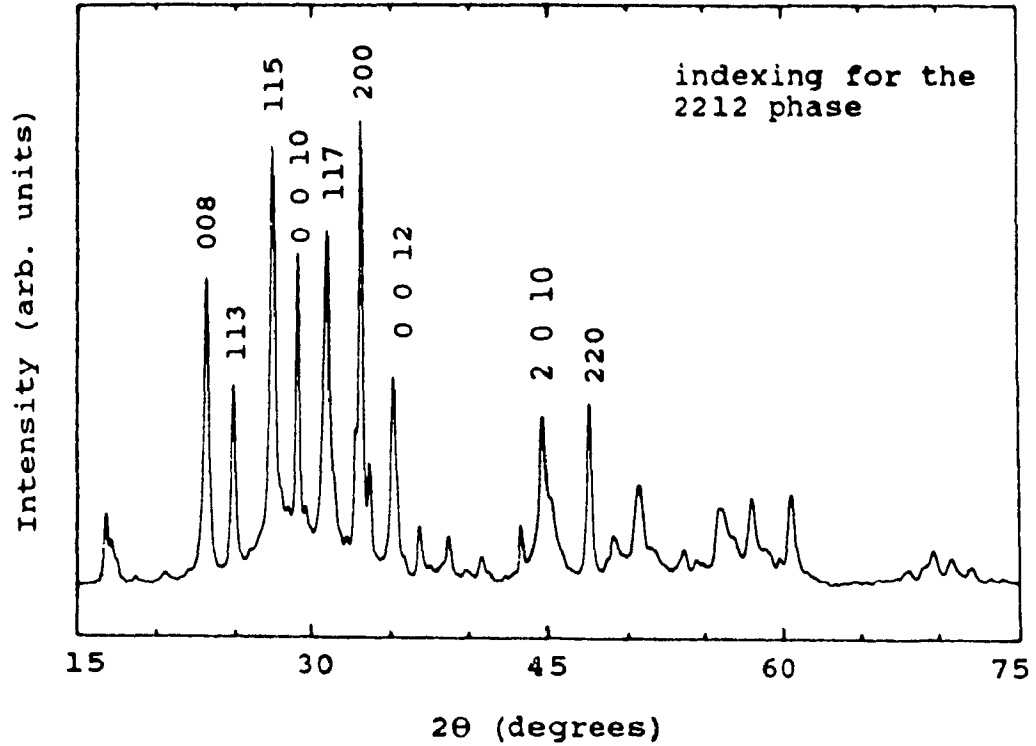


Figure 6-23. Magnetization curve of superconducting sample.

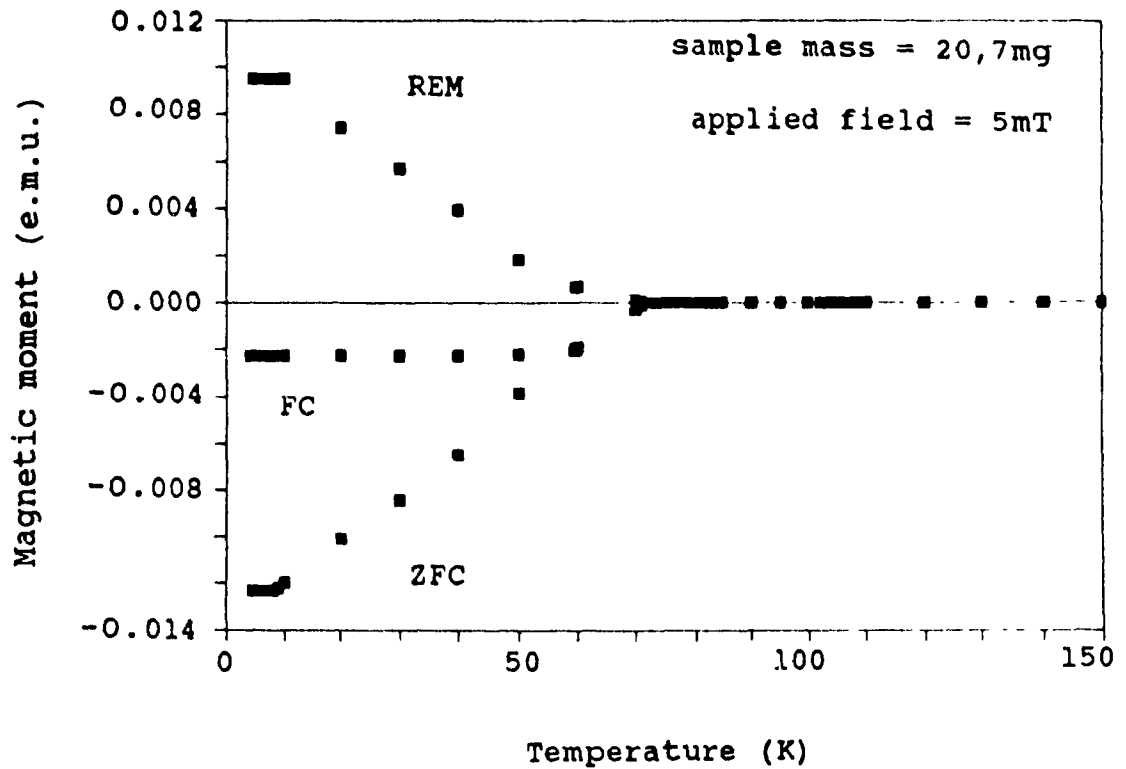
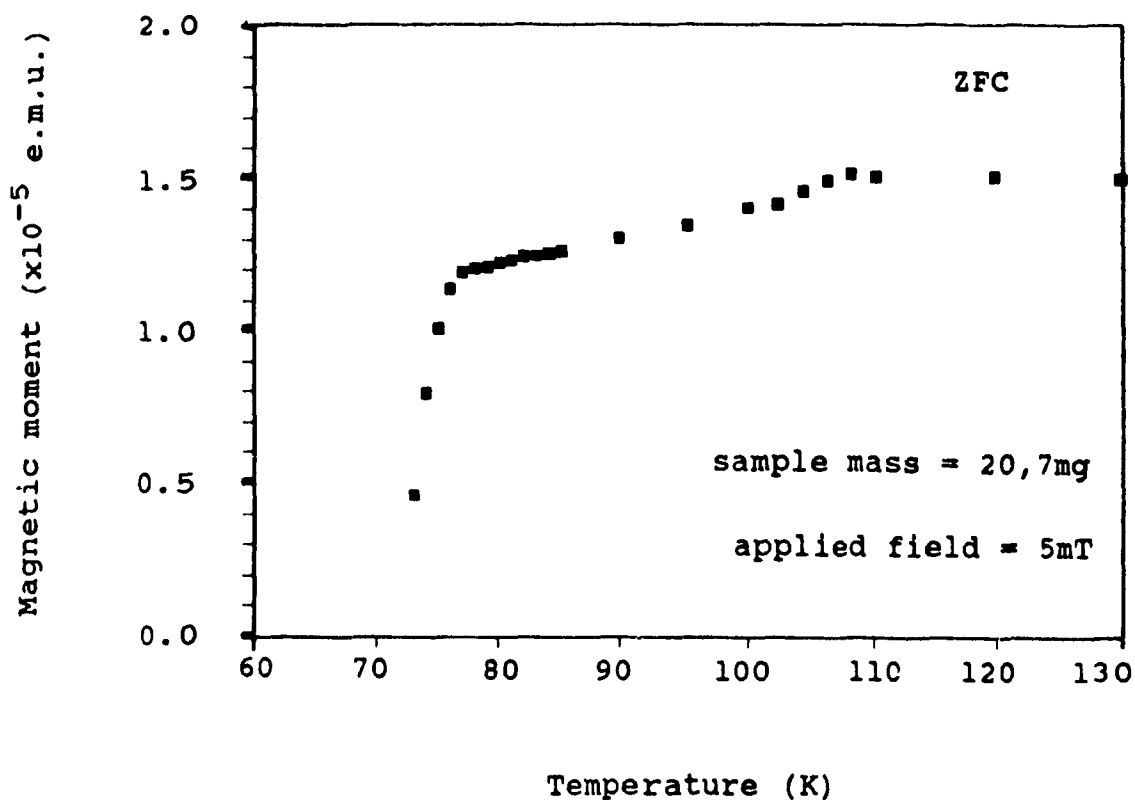


Figure 6-24. Magnetization curve of a superconducting sample (magnified region from the previous figure).



difference lies in the presence of CuO crystallites (48h milled sample).

It is known that during the crystallization of bismuth-based amorphous materials, the 2201 phase is generally the first to crystallize. Then the 2212 phase forms by diffusion of the remaining calcium and copper oxides into the 2201. The 2223 phase forms by same diffusion process. This description is still valid for our material except that the 2201 phase does not form directly from the amorphous matrix but through the formation of an intermediate phase, the bcc solid solution, which is not the same phase as the one reported by Nassau et al. [51].

## Chapter 7

## Conclusion.

The purpose of this work was to study the possibility of making superconducting material from an amorphous precursor prepared by high-energy ball milling. We have succeeded in making such a precursor. Two reactions may lead to the amorphization. First, bismuth, strontium, and calcium oxides form a body-centered cubic solid solution. Then, this phase reacts either with extra strontium oxide or copper oxide to give an amorphous phase. There is some undissolved copper oxide present in the material after milling but it is mainly amorphous.

The amorphization process described in this work could probably be interpreted as a mixture of type III and type II reactions (see section 4.2) [79]. The formation of the metastable bcc solid solution of bismuth and calcium, in the early stage of the process, is typical of type III while the amorphization by reaction with CuO or with an excess SrO is probably of type II. For copper, we know that only certain oxygen coordinations are stable and therefore the inclusion of copper inside the solid solution may destabilize the surrounding bcc lattice during the milling process and lead to the amorphous phase.

It is also found that there is little difference between the material obtained by this technique and materials obtained by rapid solidification, a result similar to those concerning metallic alloys. The main difference is that crystallization does not proceed by direct crystallization of the 2201 but by the crystallization of a bcc (Bi,Sr,Ca)-O solid solution containing copper maybe because of the presence of unreacted embryos of this phase.

Heating in oxygen transforms the metastable cubic phase (as well as part of the amorphous matrix) into a related hexagonal structure before it transforms into the 2201 phase. Subsequent high-temperature annealing in oxygen allows the formation of the 2212 superconducting phase.

It may be possible to use this material to obtain textured superconducting wires by controlling the crystallization process. The cubic phase (Bi-Sr-Ca)-O may also be used, for example by reaction with a copper sheath. It may also be possible to crystallize the 2201 phase directly by using a very high heating rate in order to bypass the growth of the cubic phase.

Apart from the interest of making superconducting materials, this work has also shown the usefulness of high-energy ball milling in making amorphous and metastable structures. The supersaturated solid solution in the Bi-Ca-O system is a good example. This phase is normally formed by thermal treatment above 1075K and has to be rapidly quenched in order to analyse it at room temperature. Ball-milling is therefore a more simple procedure in which the stoichiometry is better controlled.

As a next step in this research it would be interesting to mill the Bi(Pb)-Sr-Ca-Cu-O system.

Appendix

Table 1. Space groups and lattice parameters.

phase	space group	a (nm)	b (nm)	c (nm)	Z
2201	Amaa	0,5362	0,5374	2,4622	2
2212	Fmmm	0,5414	0,5418	3,089	2
2223	I4/mmm	0,3814	0,3814	3,700	2

Table 2. Density.

phase	obs	calc
2201	7.03	7.046
2212		6.452
2223		6.317

Table 3. Atom locations.

phase	atom	site	occupancy	x	y	z
2201	Bi	8l	100%	0.0000	0.2750	0.0660
	Sr	8l	100%	0.5000	0.2470	0.1790
	Cu	4e	100%	0.5000	0.7500	0.2500
	O1	8g	100%	0.7500	0.5000	0.2460
	O2	8l	100%	0.0000	0.2260	0.1450
	O3	8l	100%	0.5000	0.3340	0.0640
2212	Bi1	8i	92.5%	0.0000	0.0000	0.1980
	Sr	8i	100%	0.0000	0.5000	0.1090
	Ca	4a	85%	0.0000	0.5000	0.0000
	Bi2	4a	15%	0.0000	0.5000	0.0000
	Cu	8i	100%	0.0000	0.0000	0.0540
	O1	16j	100%	0.2500	0.2500	0.0510
	O2	8i	100%	0.0000	0.5000	0.1980
	O3	8i	100%	0.0000	0.0000	0.1200
2223	Bi	4e	100%	0.5000	0.5000	0.2200
	Sr	4e	100%	0.0000	0.0000	0.1440
	Cu1	2b	100%	0.5000	0.5000	0.0000
	Cu1	4e	100%	0.5000	0.5000	0.0900
	Ca	4e	100%	0.0000	0.0000	0.0500
	O1	4c	100%	0.5000	0.0000	0.0000
	O2	8g	100%	0.5000	0.0000	0.0870
	O3	4e	100%	0.5000	0.5000	0.1600
	O4	4e	100%	0.5000	0.5000	0.2720

Table 4. Diffraction data for the 2201 phase.

$d_{\text{obs}}$	$I_{\text{obs}}$	$d_{\text{calc}}$	$I_{\text{calc}}$	h	k	l
12.30	2	12.311	12	0	0	2
5.264	3	5.250	6	0	1	1+
4.922	3	4.913		2	1	1
		4.496	<1	0	1	3+
4.100	18	4.104	20	0	0	6
3.756	4	3.751	4	1	1	1
3.624	3	3.631	<1	0	1	5+
3.447	74	3.445	80	1	1	3
3.075	29	3.078	28	0	0	8
3.008	100	3.006	100	1	1	5
2.960	13	2.943	3	0	1	7+
2.688	59	2.681	53	2	0	0+
2.625	4	2.620	4	2	0	2+
2.581	4	2.580	9	1	1	7
2.460	4	2.462	8	0	0	10
		2.438	<1	0	1	9+
2.415	4	2.413		9	1	4
		2.388	1	2	1	1
2.359	3	2.358	1	1	2	2
2.246	3	2.244	2	2	0	6+
		2.238	2	1	2	4+
2.186	4	2.184		8	1	11
		2.157	<1	2	1	5+
2.095	7	2.093		1	2	12
		2.073	<1	1	2	6+
		2.052	3	0	0	12
2.0234	19	2.022	27	2	0	8+
		1.9819	<1	2	1	7
1.927	9	1.9281	14	1	1	11
1.8998	14	1.8979	22	2	2	0
		1.8135	2	2	0	10+
		1.8038	<1	2	1	9+
		1.7866	1	0	3	1+
1.7241	4	1.7226	2	2	2	6
1.6939	5	1.6947	8	1	1	13
		1.6834	<1	0	3	5+
		1.6638	5	1	3	3
		1.6609	6	3	1	3
		1.6307	2	0	2	12+
1.6173	6	1.6154	7	2	2	8
		1.6061	11	1	3	5
1.6064	17	1.6035	11	3	1	5
		1.5963	1	0	3	7+
1.5360	4	1.5389	2	0	0	16
		1.5299	1	1	3	7+
		1.5277	1	3	1	7+
		1.5032	2	2	2	10
		1.3932	2	2	2	12
		1.3518	3	3	1	11+
		1.3435	1	0	4	0
		1.3405	2	4	0	0
		1.3346	3	2	0	16+

d-spacings in angstroms

Table 5. Diffraction data for the 2212 phase.

$d_{\text{obs}}$	$I_{\text{obs}}$	$d_{\text{calc}}$	$I_{\text{calc}}$	h	k	l
15.41	8	1.445	14	0	0	2
5.332	1	5.339		0	1	1
3.855	31	3.861	25	0	0	8
3.803	3	3.801	2	1	1	1
3.586	29	3.589	35	1	1	3
3.335	14	3.346		6	1	1
3.251	92	3.255	100	1	1	5
3.149	3	3.152		8	0	2
3.085	35	3.089	26	0	0	10
3.010	10	3.020		4	1	7+
2.890	75	2.892	80	1	1	7
2.825	1	2.826		2	1	9
2.788	1	2.788		1	0	11
2.707	100	2.707	96	2	0	0+
2.668	8	2.666	11	0	2	2+
2.572	21	2.574	17	0	0	12
		2.556	28	0	2	4+
2.444	12	2.445		2	1	11+
		2.265	3	1	1	11
2.216	1	2.218	4	0	2	8+
2.034	33	2.2036	37	2	0	10+
2.015	10	2.019	7	1	1	13
		1.9306	4	0	0	16
1.9134	38	1.9148	34	2	2	0
1.8623	8	1.8654	8	2	0	12+
1.8122	21	1.8137	13	1	1	15
1.7176	3	1.7177		14	1	3+
		1.7155	4	2	2	8
1.6869	3	1.6890	3	3	1	3+
1.6484	14	1.6509	14	3	1	5+
1.6391	3	1.6416	6	1	1	17
1.6266	3	1.6275	8	2	2	10
		1.5962	13	3	1	7+
1.5737	3	1.5737		8	3	1
		1.5722	3	0	2	16+
		1.5445	4	0	0	20
		1.5364	6	2	2	12
1.5335	12	1.5329	9	1	3	9+
1.3590	1	1.3595	2	2	2	16
1.3525	5	1.3545	4	4	0	0+
		1.3418	4	0	2	20+
1.3151	3	1.3170	4	3	1	15+
		1.2501	2	3	3	5
		1.2464	3	2	0	22+
		1.2405	2	0	4	10+
1.2101	1	1.2108	4	4	2	0+
		1.2022	3	2	2	20
		1.1987	2	0	4	12+
		1.1965	2	3	3	9
		1.1277	2	2	4	10+
		1.0962	2	1	1	27
		0.9513	2	3	1	27+

d-spacings in angstroms

Table 6. Diffraction data for the 2223 phase (calculated values).

d	I	h	k	l
18.500	100	0	0	2
9.250	12	0	0	4
6.167	7	0	0	6
4.625	2	0	0	8
3.794	1	1	0	1
3.700	<1	0	0	10
3.644	1	1	0	3
3.390	17	1	0	5
3.093	38	1	0	7
2.796	42	1	0	9
2.697	40	1	1	0
2.669	16	1	1	2
2.643	12	0	0	14
2.589	2	1	1	4
2.523	2	1	0	11
2.471	<1	1	1	6
2.330	<1	1	1	8
2.313	6	0	0	16
2.281	5	1	0	13
2.179	<1	1	1	10
2.071	2	1	0	15
2.056	1	0	0	18
2.030	2	1	1	12
1.9070	19	2	0	0
1.8970	12	2	0	2
1.8876	9	1	1	14
1.8677	<1	2	0	4
1.8219	<1	2	0	6
1.7555	7	1	1	16
1.7344	<1	1	0	19
1.6896	<1	2	1	3
1.6818	2	0	0	22
1.6621	3	2	1	5
1.6348	2	1	1	18
1.6233	9	2	1	7
1.5995	3	1	0	21
1.5755	11	2	1	9
1.5465	5	2	0	14
1.5213	<1	2	1	11
1.4822	4	1	0	23
1.4713	3	2	0	16
1.4631	2	2	1	13
1.4271	2	1	1	22
1.4029	1	2	1	15
1.3980	1	2	0	18
1.3484	4	2	2	0
1.3449	2	2	2	2
1.3384	<1	1	1	24
1.3343	<1	2	2	4
1.2831	<1	2	1	19
1.2614	2	2	0	22
1.2530	<1	3	0	5
1.2361	1	3	0	7
1.2333	1	0	0	30
1.2255	1	2	1	21
1.2146	2	3	0	9
1.2100	<1	1	0	29
1.2061	3	3	1	0

1.2035	3	3	1	2
1.2011	2	2	2	14
1.1960	1	3	1	4
1.1866	<1	1	1	28
1.1703	3	2	1	23
1.1671	1	3	1	8
1.1649	1	2	2	16
1.1608	<1	3	0	13
1.1391	1	1	0	31
1.1275	<1	2	2	18
1.1232	<1	3	1	12
1.1216	<1	1	1	30
1.1178	<1	2	1	25
1.0972	2	3	1	14
1.0694	1	3	1	16
1.0520	1	2	2	22
1.0472	<1	3	2	5
1.0402	<1	3	1	18
1.0373	1	3	2	7
1.0356	1	2	0	30
1.0310	<1	3	0	21
1.0278	<1	0	0	36
1.0244	2	3	2	9
1.0217	1	2	1	29
1.0187	<1	1	0	35
0.9974	<1	3	0	23
0.9915	<1	3	2	13
0.9887	<1	2	0	32
0.9801	1	3	1	22
0.9779	2	2	1	31
0.9673	<1	1	0	37
0.9604	<1	1	1	36
0.9535	1	4	0	0
0.9514	<1	3	2	17
0.9179	<1	4	1	5
0.9158	<1	1	1	38
0.9112	1	4	1	7
0.9101	<1	2	2	30
0.9069	<1	3	2	21
0.9047	1	2	0	36
0.9025	1	4	1	9
0.9006	<1	3	0	29
0.8990	<1	3	3	0
0.8969	1	4	0	14
0.8908	<1	3	1	28
0.8838	1	3	2	23
0.8815	1	4	0	16
0.8797	<1	4	1	13
0.8702	<1	3	0	31
0.8672	<1	2	0	38
0.8623	1	3	1	30
0.8606	<1	3	2	25
0.8528	1	4	2	0
0.8511	1	3	3	14
0.8492	<1	4	2	4
0.8379	<1	3	3	16
0.8374	<1	1	1	42
0.8295	<1	4	0	22
0.8190	<1	4	1	21
0.8174	<1	2	2	36
0.8116	1	4	2	14
0.8086	<1	3	3	20

d-spacings in angstroms

Table 7. Summary of rapid solidification studies.

Composition, techniques and resulting amorphous samples.

reference	composition Bi:Sr:Ca:Cu	quenching technique	cooling rate (K/sec)	X-ray pattern halo's position	crystalline phases
Komatsu et al. [35]	1:1:1:2	splat quenching		30	
Komatsu et al. [36]	1.5:1:1.5:2	splat quenching		30	
Minami et al. [50]	1:1:1:2	twin roller	$10^6$	30	CaO
Inoue et al. [28]	1:1:1:2 1.3:1:1:2	melt-spinner		30	
Garzon et al. [18]	1.5:1:1:2	splat quenching		20, 30	
Shimomura et al. [69]	1:1:1:2	twin roller		30	unidentified phase(s)
Kanai et al. [33]	1:1:1:2	liquid nitrogen		30	Cu <sub>2</sub> O+unid. phase(s)
Yoshimura et al. [86]	2:2:1:2	rapid melting +twin roller	$10^5$	20, 30, 50	CaO
Abe et al. [1]	1:1:1:2	pumping in glass tubes		30	unidentified phase(s)
Zheng et al. [90]	4:3:3:4	splat quenching		20, 30	
Liu et al. [39]	1:1:1:2	splat quenching	$10^3-10^5$	Sr <sub>0.9</sub> Bi <sub>1.1</sub> O <sub>2.55</sub> CaCO <sub>3</sub>	
Oka et al. [54]	2:2:1:2 4:3:3:6	ice water			
Tatsumisago et al. [73]	1.5:1:1:2 2.7:1:1:2 1.5:1:1:2 2.7:1:1:2	twin roller twin roller splat quenching	$10^5$ $10^5$ $10^2$ $10^2$		
Hinks et al. [26]	2:2:2:3	splat quenching			
Yoshimura et al. [87]	2:2:2:3	rapid melting +twin roller		20, 30, 50	CaO
Chauduri et al. [9]	4:3:3:4	splat quenching		20, 30	

Shi et al. [68]	2:2:2:3 2:2:3:4 2:2:4:5	splat quenching			
Zeng et al. [89]	1.5:1.5:1:2 1.5:1.5:1:2 2:1.5:1.5:2	splat quenching		30 30 30	
Shi et al. [67]	2:2:2:3 2:2:3:4 2:2:4:5	splat quenching		30 30 30	
Takei et al. [72]	2:2:1:2	splat quenching		30	
Nassau et al. [51]	2:2:1:2 2:2:1:2 4:3:3:4 4:3:3:4 2:2:2:3 2:2:2:3	twin roller	10 <sup>7</sup>	30 30 30 30 30 30	
Gonçalves et al. [21]	2:2:2:3	splat quenching			
Zhiyi et al. [92]	1:1:1:2	splat quenching		30	
Tohge et al. [74]	2:2:2:3	twin roller	10 <sup>6</sup>	30	CaO

---

Table 8. Summary of rapid solidification studies (continued).

## Thermal analysis.

reference	technique	T <sub>G</sub> (K)	T <sub>x</sub> (K)	other exo peaks (K)	endo (K)	rate (K/min)
Komatsu et al. [35]						
Komatsu et al. [36]	DTA	700	765	904	1041, 1156	5
Minami et al. [50]	DTA	663	717	823(broad)		10
Inoue et al. [28]	DSC	680 <680	725 730			40 40
Garzon et al. [18]	DSC		728			10
Shimomura et al. [69]						
Kanai et al. [33]	DTA in air		783		983, 1053 1148, 1193, 1243	5
Yoshimura et al. [86]	DTA	700	749, 779		1133	
Abe et al. [1]						
Zheng et al. [90]	DTA	707	751		>1106	10
Liu et al. [39]						
Oka et al. [54]	DTA		703 708	773(broad) 773(broad)		10 10
Tatsumisago et al. [73]	DSC in helium	679 652 684 660	725 718 739 730			20 20 20 20
Hinks et al. [26]	DTA in oxygen		723	843, 1075	1050, 1160, 1173	10
Yoshimura et al. [87]	DTA in air	683	750	785		10
Chauduri et al. [9]	DTA	747				



Table 9. Summary of rapid solidification studies (end).

Resistivity measurements.					
reference	treatment (°C)	T <sub>C</sub> (onset) (K)	T <sub>C</sub> (K)	T <sub>C</sub> (zero) (K)	J <sub>C</sub> (77K) A/cm <sup>2</sup>
Komatsu et al. [35]	800 24 hours in oxygen	110		80	102
Komatsu et al. [36]	820 24 hours in oxygen +quenching in liquid nitrogen	83		65	
Minami et al. [50]	850 2 hours	88			
Inoue et al. [28]					
Garzon et al. [18]	820 1 hour in oxygen +quenching in air	85			
Shimomura et al. [69]	880 6 hours	90		60	220 (4.2K)
Kanai et al. [33]	840 5 hours in air heating and cooling 300 <sup>0</sup> /min	120	80		
Yoshimura et al. [86]	850 36 hours in air	86.8		66.7	
Abe et al. [1]	840 maximum (temperature gradient 30 <sup>0</sup> /mm 0.1mm/min)			62	
Zheng et al. [90]	800 in air	100		45	
Liu et al. [39]	860 2 hours in air	107			
Oka et al. [54]					
Tatsumisago et al. [73]					
Hinks et al. [26]	830 12 hours	110		80	

Yoshimura et al. [87]	880 1 hour in air	111		
Chauduri et al. [9]	800 12 hours in air +slow cooling	100	85	1.5
Shi et al. [68]	870 in air 16 days 16 days 10 days	110 110 110	80 80 100	
Zeng et al. [89]	813 824 823 130 hours in air +liquid nitrogen	98 101 90	72 90 55	
Shi et al. [67]	870 in air 12 hours 10 days	110	85 105	
Takei et al. [72]	800	84	80	55
Nassau et al. [51]				
Gonçalves et al. [21]	820 72 hours in air		95.5	1
Zhiyi et al. [92]	810 860 920 30 minutes in air +rapid cooling	107 107 95		
Tohge et al. [74]	860 4 hours in air	96	86	

---

Table 10. Diffraction data for sample milled 48 hours and heated to 800K at 20K/min in argon.

angle	d	intensity	phase	h	k	l
29,66	3,0097	100,0	cubic	1	1	0
42,49	2,1258	26,8	cubic	2	0	0
52,66	1,7368	46,7	cubic	2	1	1
61,57	1,5050	17,7	cubic	2	2	0
69,88	1,3450	10,9	cubic	3	1	0
78,18	1,2217	4,1	cubic	2	2	2
85,30	1,1370	10,5	cubic	3	2	1

d-spacings in angstroms

cubic = body-centered cubic phase (see section 5.2.3)

Table 11. Diffraction data for sample milled 48 hours and heated to 1000K at 20K/min in argon.

angle	d	intensity	phase	h	k	l
21,79	4,0753	10,5	2201	0	0	6
23,65	3,7589	2,0	2201	1	1	1
25,82	3,4477	56,5	2201	1	1	3
29,19	3,0568	24,6	2201	0	0	8
29,74	3,0016	100,0	2201	1	1	5
32,16	2,7810	3,6	unidentified			
33,27	2,6907	70,1	2201	2	0	0+
34,15	2,6234	2,8	2201	2	0	2+
34,82	2,5744	6,5	2201	1	1	7
35,53	2,5246	20,5	CuO	1 0	1 0	1 2
36,86	2,4365	16,5	2201	0	0	10
37,30	2,4087	16,3	CaO	1	1	1
38,72	2,3236	25,1	CuO	1 2	1 0	1 0
40,14	2,2446	4,8	2201	2	0	6+
44,51	2,0339	5,6	2201	superlattice reflection		
44,86	2,0188	43,5	2201	2	0	8
45,41	1,9956	2,4	2201	2	1	7
47,35	1,9183	29,5	2201	1	1	11
47,79	1,9016	33,8	2201	2	2	0
48,75	1,8664	7,7	CuO	2	0	2
50,66	1,8004	20,3	unidentified			
53,11	1,7230	2,3	2201	2	2	6
53,79	1,7028	12,4	unidentified			
54,41	1,6849	10,9	2201	1	1	13
55,12	1,6648	17,4	2201	3	1	3
57,12	1,6112	39,9	2201	2	2	8

57,32	1,6061	26,1	2201	3	1	5
58,06	1,5873	7,0	2201	0	3	7+
59,95	1,5417	7,4	unidentified			
60,46	1,5299	5,9	2201	0	0	16
61,65	1,5032	6,6	2201	2	2	10
64,07	1,4522	2,3				
64,94	1,4348	0,4				
66,06	1,4132	14,4				
67,30	1,3901	7,6				
68,08	1,3761	10,1				
69,73	1,3475	30,2				
70,94	1,3274	5,1				
74,21	1,2768	3,7				
75,38	1,2599	20,8				
77,79	1,2268	22,0				
79,67	1,2025	18,2				
80,48	1,1924	5,4				
86,98	1,1192	11,4				
91,37	1,0765	7,0				
96,69	1,0309	17,4				
99,11	1,0122	13,1				

---

d-spacings in angstroms

no standard is available for d-spacings below 1,5000

Table 12. Diffraction data for sample milled 48 hours and heated to 800K at 20K/min in oxygen.

angle	d	intensity	phase	h	k	l
17,63	5,0279	10,2	hexagonal	1	0	0
29,88	2,9876	14,3	cubic	1	1	0
30,71	2,9089	100,0	hexagonal	1 1	1 0	0 1
35,43	2,5315	12,6	CuO	$\bar{1}$ 0	1 0	1 2
38,53	2,3347	16,2	CuO	1 2	1 0	1 0
42,78	2,1120	2,2	cubic	$\bar{2}$	0	2
44,08	2,0526	18,4	hexagonal	2	0	1
53,44	1,7130	11,0	cubic	2	1	1
54,65	1,6780	19,5	hexagonal	1 3 2	0 0 1	2 0 1
61,54	1,5056	6,5	cubic hexagonal	2 3 1	2 0 1	0 1 2

d-spacings in angstroms

hexagonal = hexagonal phase

Table 13. Diffraction data for sample milled 48 hours and heated to 1000K at 20K/min in oxygen.

angle	d	intensity	phase	h	k	l
7,17	12,3187	6,6	2201	0	0	2
16,80	5,2729	7,8	2201	0	1	1+
17,55	5,0492	9,2	2201	superlattice reflection		
19,54	4,5392	10,1	2201	0	1	3
19,79	4,4825	5,2	2201	1	0	3
21,75	4,0827	23,9	2201	0	0	6
23,70	3,7511	7,2	2201	1	1	1
24,91	3,5715	10,6	2201 2212	0 1	1 1	5+ 3
25,87	3,4411	80,8	2201	1	1	3
26,62	3,3458	5,2	2212	superlattice reflection		
27,51	3,2396	15,6	2212	1	1	5
27,97	3,1873	4,0	unidentified			
29,17	3,0589	26,3	2201	0	0	8
29,78	2,9976	100,0	2201	1	1	5
30,37	2,9407	18,2	2201	0	1	7+
30,79	2,9015	28,1	2212	1	1	7
31,04	2,8787	32,8	(Sr,Ca) <sub>14</sub> Cu <sub>24</sub> O <sub>41</sub>	2	4	0
31,90	2,8031	12,4	unidentified			
32,73	2,7339	13,3	2212	2	0	0+
33,38	2,6821	65,1	2201	2	0	0+
34,21	2,6189	2,4	2201	2	0	2+
34,73	2,5809	4,2	2212	0	0	12
34,88	2,5701	4,3	2201	1	1	7
35,47	2,5287	17,0	CuO	T 0	1 0	1 2
35,96	2,4954	0,9	unidentified			

36,64	2,4506	5,5	2201 2212	0 0	0 10	superlattice reflection
37,02	2,4263	2,4	2201			superlattice reflection
37,34	2,4062	3,7	CaO	1	1	1
38,66	2,3271	18,6	CuO	1	1	1
			2201	2	0	0
				1	2	2
40,24	2,2393	6,3	2201	2	0	6+
43,52	2,0778	7,5	2201			superlattice reflection
44,40	2,0386	25,1	2212	2	0	10+
44,94	2,0154	28,6	2201	2	0	8+
			2212	1	1	13
45,76	1,9812	0,8	2201	2	1	7
46,51	1,9509	2,0	unidentified			
47,37	1,9175	18,3	2201	1	1	11
			2212	2	2	0
47,96	1,8953	22,9	2201	2	2	0
48,65	1,8700	4,6	CuO	2	0	2
50,96	1,7905	21,5	unidentified			
52,35	1,7462	5,4	unidentified			
53,30	1,7173	5,1	2201	2	2	6
54,40	1,6852	8,0	2201	1	1	13
54,95	1,6696	19,1	2201	1	3	3
55,34	1,6587	10,5	2201	3	1	3
			2212	3	1	5+
56,12	1,6375	7,0	unidentified			
57,22	1,6086	15,0	2201	2	2	8
57,50	1,6015	14,3	2201	3	1	5
58,01	1,5886	21,7	2201	0	3	7+
59,52	1,5518	3,7	unidentified			
60,56	1,5276	8,1	2201	0	0	16
			2212	1	3	9+
61,85	1,4988	6,8				

63,93	1,4550	10,7
67,47	1,3870	2,0
69,73	1,3475	6,8
70,18	1,3399	2,8
71,05	1,3257	3,4
79,98	1,1986	2,4
80,87	1,1876	7,7
84,28	1,1481	3,1
89,24	1,0966	9,5

---

d-spacings in angstroms

Table 14. Diffraction data for sample milled 48 hours and annealed 20 hours at 1125K in oxygen.

angle	d	intensity	phase	h	k	l
5,75	15,3573	40,9	2212	0	0	2
16,63	5,3264	12,3	2212	superlattice reflection		
16,97	5,2205	11,1	unidentified			
17,32	5,1157	3,3	unidentified			
18,56	4,7767	3,6	unidentified			
20,52	4,3246	3,0	unidentified			
23,14	3,8406	90,9	2212	0	0	8
24,86	3,5786	47,3	2212	1	1	3
25,92	3,4346	0,7	unidentified			
27,22	3,2734	8,3	unidentified			
27,48	3,2431	100,0	2212	1	1	5
27,99	3,1851	11,8	unidentified			
28,45	3,1347	7,2	2212	superlattice reflection		
29,13	3,0630	54,7	2212	0	0	10
29,65	3,0105	3,7	2212	superlattice reflection		
30,81	2,8997	20,8	(Sr,Ca) <sub>14</sub> Cu <sub>24</sub> O <sub>41</sub>	2	4	0
31,01	2,8815	98,4	2212	1	1	7
31,46	2,8413	8,1	unidentified			
31,83	2,8091	1,2	unidentified			
32,33	2,7668	13,8	unidentified			
32,78	2,7298	18,7	unidentified			
33,14	2,7010	94,1	2212	2	0	0+
			(Sr,Ca) <sub>14</sub> Cu <sub>24</sub> O <sub>41</sub>	3	1	1
33,70	2,6574	17,4	2212	0	2	2+
35,20	2,5475	60,7	2212	0	0	12
35,49	2,5273	4,7	CuO	1	1	1
				0	0	2

35,92	2,4980	1,6	unidentified			
36,94	2,4314	14,0	2212	superlattice reflection		
37,52	2,3951	5,6	unidentified			
38,42	2,3411	7,3	unidentified			
38,73	2,3230	4,7	unidentified			
38,84	2,3167	2,4	CuO	1 2	1 0	1 0
39,79	2,2635	1,6	unidentified			
40,66	2,2171	3,0	unidentified			
40,85	2,2072	5,2	2212	0	2	8+
41,26	2,1862	1,8	(Sr,Ca) <sub>14</sub> Cu <sub>24</sub> O <sub>41</sub>	4	4	0
43,48	2,0796	9,1	unidentified			
44,72	2,0248	22,8	2212	2	0	10+
44,95	2,0150	76,1	unidentified			
45,20	2,0044	2,4	2212	1	1	13
47,58	1,9095	48,6	2212	2	2	0
48,73	1,8671	0,3	CuO	2	0	2
49,19	1,8507	14,1	2212	2	0	12+
50,62	1,8018	38,3	2212	1	1	15
51,47	1,7740	7,4	unidentified			
52,98	1,7269	0,5	unidentified			
53,55	1,7099	7,4	2212	superlattice reflection		
54,46	1,6834	1,7	2212	3	1	3+
54,88	1,6715	1,2	unidentified			
55,99	1,6410	41,4	2212	3	1	5+
56,73	1,6213	13,4	2212	2	2	10
57,90	1,5913	31,8	2212	3	1	7+
58,80	1,5691	14,8	2212	superlattice reflection		
59,72	1,5471	2,4	unidentified			
60,54	1,5281	32,7	2212	1	3	9+

67,89	1,3794	6,2
68,97	1,3605	3,7
69,59	1,3498	14,8
70,86	1,3287	12,5
72,12	1,3086	5,5
79,35	1,2065	7,0
80,40	1,1934	7,9

---

Table 15. Calculated X-ray intensities from a bcc structure for various chemical compositions<sup>1</sup>.

occupancy of the (0,0,0) and the (1/2,1/2,1/2) equivalent site		calculated X-ray peak intensities				
		110	200	211	220	310
Bi	100%	100	20	43	14	10
Ca	100%	100	18	36	11	7
Bi	50%					
Ca	50%	100	19	42	13	9
Bi	33%					
Sr	33%					
Ca	33%	100	19	41	13	9
Bi	25%					
Sr	25%					
Ca	25%					
Cu	25%	100	19	41	13	9

<sup>1</sup> Using the procedure described by Warren [78], neglecting the effect of thermal vibrations, and using a polarization factor applicable to our experimental apparatus.

## Bibliography

- [1] Abe Y., Hosono H., Hosoe H., Iwase J., Kubo Y., Appl. Phys. Lett., 1341, 53 (1988)
- [2] Awano M., Kani K., Komada Y., Takagi H., Kuwahara Y., L254, 29 (1990)
- [3] Bardeen J., Cooper L.N., Schrieffer J.R., Phys. Rev. 1175, 108 (1975)
- [4] Batalla E. and Zwartz E.G., J. Mater. Res., 1802, 5 (1990)
- [5] Bednorz J.G. and Muller K.A., Z. Phys. B, 189, 64 (1986)
- [6] Benjamin J.S. and Volin T.E., Metall. Trans., 1929, 5 (1974)
- [7] Bruning R., Altounian Z., Strom-Olsen J.O., and Shultz L., Mater. Sci. Eng., 317, 97 (1988)
- [8] Cava R.J., Scientific American, 42, 263 (1990)
- [9] Chaudhuri B.K., Som K., and Sen Gupta S.P., J. Mater. Sci. Lett., 520, 8 (1989)
- [10] Colmenero J., Ilarraz J., and Barandiaran J.M., Thermochem. Acta, 381, 35 (1980)
- [11] Conflant P., Boivin J.-C., and Thomas D., J. Solid State Chem., 133, 18 (1976)
- [12] Cooper L.N., Phys. Rev., 1189, 104 (1956)
- [13] Davis R.M., McDermott B., and Kock C.C., Metall. Trans. A, 2867, 19A (1988)
- [14] Davis R.M. and Koch C.C., Scripta Metallurgica, 305, 21 (1987)
- [15] Duwez P., Willens R.H., and Klement W., Jr., J. Appl. Phys., 1136, 31 (1960)
- [16] File J. and Mills R.G., Phys. Rev. Lett., 93, 10 (1963)
- [17] Frolich H., Phys. Rev., 815, 79 (1950)
- [18] Garzon F.H., Beery J.G., Raistrick I.D., Appl. Phys. Lett., 805, 53 (1988)
- [19] Gessinger G.H., Metall. Trans. A, 1203, 7A (1976)
- [20] Ginzburg V.L. and Landau L.D., Sov.Phys. JETP, 1064, 20, (1950)
- [21] Gonçalves A.P., Santos I.C., Almeida M., Figueiredo M.O., Costa F., Vieira J.M., Alves J.M., and Godinho M.M., Physica C, 273, 159 (1989)
- [22] Grader G.S., Gyorgy E.M., Gallagher P.K., O'Bryan H.M., Johnson D.W., Jr., Sunshine S., Zahurak S.M., Jin S., Sherwood R.C., Phys. Rev. B, 757, 38 (1988)

- [23] Green S.M., Jiang C., Mei Y., Luo H.L., and Politis C., Phys. Rev. B, 5016, 38 (1988)
- [24] Guillermo R., Conflant P., Boivin J.-C., and Thomas D., Rev. Chim. Min., 153, 15 (1978)
- [25] Hellstern E., Schultz L., and Eckert J., J. Less Common Metals, 93, 140 (1988)
- [26] Hinks D.G., Soderholm L., Capone D.W., II, Dabrowski B., Mitchell A.W., and Shi D., Appl. Phys. Lett., 423, 53 (1988)
- [27] Hitachi, private communication
- [28] Inoue A., Kimura H., Matsuzaki K., Tsai A.-P., and Masumoto T, Jpn. J. Appl. Phys., L941, 27 (1988)
- [29] Jin S., Tiefel T.H., Sherwood R.C., Davis M.E., van Dover R.B., Kammlott G.W., Fastnacht R.A., and Keith H.D., Appl. Phys. Lett., 2074, 52 (1988)
- [30] Jin S., Tiefel T.H., Sherwood R.C., van Dover R.B., Davis M.E., Kammlott G.W., and Fastnacht R.A., Phys. Rev. B, 7850, 37 (1988)
- [31] Kamerlingh Onnes H., Akad van Wetenschappen (Amsterdam) 14, 113, 818 (1911)
- [32] Kanai T., Kamo T., and Matsuda S.-P., Jpn. J. Appl. Phys, L412, 29 (1990)
- [33] Kanai T., Kumagai T., Soeta A., Suzuki T., Aihara K., Kamo T., Matsuda S., Jpn. J. Appl. Phys., L1435, 27 (1988)
- [34] Koch C.C., Cavin O.B., McKamey C.G., and Scarbrough J.O., Appl. Phys. Lett., 1017, 43 (1983)
- [35] Komatsu T., Imai K., Sato R., Matusita K., and Yamashita T., Jpn. J. Appl. Phys., L533, 27 (1988)
- [36] Komatsu T., Stao R., Imai K., Matusita K., and Yamashita T., Jpn. J. Appl. Phys., L550, 27 (1988)
- [37] Lavallée F., master thesis, Ecole Polytechnique de Montréal, Montréal, 1991
- [38] Lee C.L., Chen J.-J., Wen W.-J., Perng T.-P., Wu J.-M., Wu T.-B., and Chin T.-S., J. Mater. Res., 1403, 5 (1990)
- [39] Liu P., Knutson M., Liu Z., Olsson E., and Dunlop G.L., Supercond Sci. Technol., 254, 1 (1989)
- [40] Love E.H., "A Treatise on the Mathematical Theory of Elasticity", 4th ed., Dover, New York, NY, 1944, pp. 193-200
- [41] Maeda H., Tanaka Y., Fukutomi M., and Asano T., Jpn. J. Appl. Phys., L209, 27 (1988)
- [42] Massalski T.B., Metall. Trans. A, 1295, 20A (1989)
- [43] Mathers D.P. and Snyder R.L., Powder Diffraction, 8, 5 (1990)
- [44] Maurice D.R. and Courtney T.H., Metall. Trans. A, 289, 21A (1990)

- [45] McCarron E.M., III, Subramanian M.A., Calabrese J.C., and Harlow R.L., *Mat. Res. Bull.*, 1355, 23 (1988)
- [46] McKittrick J., McHenry M.E., Standley P., Heremans C., Prasanna T.R.S., Kalonji G., O'Handley R.C., *Mat. Res. Soc. Proc.*, 567, 99 (1988)
- [47] Meissner W. and Oschenfeld R., *Naturwissenschaften*, 787, 21 (1933)
- [48] Michel C., Hervieu M., Borel M.M., Grandin A., Deslandes F., Provost J., and Raveau B., *Z. Phys. B*, 421, 68 (1987)
- [49] Miller P.J., Coffey C.S., and DeVost V.F., *J. Appl. Phys.*, 913, 59 (1986)
- [50] Minami T., Akamatsu Y., Tatsumisago M., Tohge N., and Kowada Y., *Jpn. J. Appl. Phys.*, L777, 27 (1988)
- [51] Nassau R., Miller A.E., Gyorgy E.M., and Siegrist T., *J. Mater. Res.*, 1330, 4 (1989)
- [52] Nishi Y., Manabe T., Kameyama H., Moriya S., Kataragi T., Uchida, Kawakami M., *J. Mater. Sci. Lett.*, 801, 9 (1990)
- [53] Ogushi T. and Osono Y., *Appl. Phys. Lett.*, 1167, 48 (1986)
- [54] Oka Y., Yamamoto N., Kitaguchi H., Oda K., and Takada J., *Jpn. J. Appl. Phys.*, L213, 28 (1989)
- [55] Phillips J.C., "Physics of High-Tc superconductors", Academic Press, San Diego, 1989
- [56] Politis C., *Physica B*, 286, 135 (1985)
- [57] Roth R.S., Rawn C.J., Bendersky L.A., *J. Mater. Res.*, 46, 5 (1990)
- [58] Salama K., Selvamanickam V., Gao L., and Sun K., *Appl. Phys. Lett.*, 2352, 54 (1989)
- [59] Scherrer P., *Nachr. Gottinger Gesell.*, 98 (1918); *Zsigmondys Kolloidchemie*, 3rd Ed.
- [60] Schulz R., Trudeau M.L., Dussault D., and Van Neste A., *Proc. of the Int. Symp. on Solid State Reaction, Grenoble, February 1990, "Multilayer Amorphisation by Solid State Reaction and Mechanical Alloying"*, Ed. by A.R. Yavary and P.J. Desré, *Colloque de Physique* no 4, tome 51, Supplement to the *J. de Physique*, Fasc. 14, C4, 1990, p. 259
- [61] Schulz R., Trudeau M.L., Huot J.-Y., Van Neste A., *Phys. Rev. Lett.*, 2849, 62 (1989)
- [62] Schulz R., Trudeau M.L., and Van Neste A., *Proc. of the 7th Int. Conf. on Rapidly Quenched Materials, Stockholm, August 1990, Mat. Sci. Eng.*, A134, 1354 (1991)
- [63] Schwarz R.B. and Johnson W.L., *Phys. Rev. Lett.*, 415, 51 (1983)
- [64] Schwarz R.B. and Koch C.C., *Appl. Phys. Lett.*, 146, 49 (1986)

- [65] Schwarz R.B., Petrich R.R., and Saw C.K., *J. Non-Cryst. Solids*, 281, 76 (1985)
- [66] Shi D., Boley M.S., Chen J.G., Zu M., Vandervoort K., Liao Y.X., Zangvil A., Akujieze J., Segre C., *Appl. Phys. Lett.*, 699, 55 (1989)
- [67] Shi D., Tang M., Boley M.S., Hash M., Vandervoort K., Claus H., Lwin Y.N., *Phys. Rev. B*, 2247, 40 (1989)
- [68] Shi D., Tang M., Vandervoort K., and Claus H., *Phys. Rev. B*, 9091, 39 (1989)
- [69] Shimomura S., Takahashi K., Ohta M., Watanabe A., Seido M., Hosono F., *L1890*, 27 (1988)
- [70] Siegrist T., Schneemeyer L.F., Sunshine S.A., and Waszczak J.V., *Mat. Res. Bull.*, 1429, 23 (1988)
- [71] Sunshine S.A., Siegrist T., Schneemeyer L.F., Murphy D.W., Cava R.J., Batlogg B., van Dover R.B., Fleming R.M., Glarum S.H., Nakahara S., Farrow R., Krajewski J.J., Zahurak S.M., Waszczak J.V., Marshall J.H., Marsh P., Rupp L.W., Jr., Peck W.F., *Phys. Rev. B*, 893, 38 (1988)
- [72] Takei H., Koike M., Takeya H., Suzuki K., and Ichihara M., *Jpn. J. Appl. Phys.*, L1193, 28 (1989)
- [73] Tatsumisago M., Angell C.A., Tsuboi S., Akamatsu Y., Tohge N., and Minami T., *Appl. Phys. Lett.*, 2268, 54 (1989)
- [74] Tohge N., Tsuboi S., Tatsumisago M., and Minami T., *Jpn. J. Appl. Phys.*, L1742, 28 (1989)
- [75] Tinkham M., "Introduction to Superconductivity", Robert E. Krieger Publishing Co., Malabar, 1980
- [76] Torardi C.C., Subramanian M.A., Calabrese J.C., Gopalakrishnan J., McCarron E.M., Morissey K.J., Askew T.R., Flippen R.B. Chowdhry U., and Sleight A.W., *Phys. Rev. B*, 225, 38 (1988)
- [77] Trudeau M.L., Schulz R., Dussault D., and Van Neste A., *Phys. Rev. Lett.*, 99, 64 (1990)
- [78] Warren B.E., "X-ray Diffraction", Dover Publications Inc., New York, 1990, pp. 251-275
- [79] Weeber A.W. and Bakker H., *Physica B*, 93, 153 (1988)
- [80] Weeber A.W., van der Meer K., Bakker H., de Boer F.R., Thijsse B.J., and Jongste J.F., *J. Phys. F.*, 1897, 16 (1986)
- [81] Weeber A.W., Wester A.J.H., Haag W.J., and Bakker H., *Physica B*, 349, 145 (1987)
- [82] Worthington T.K., Gallagher W.J., and Dinger T.R., *Phys. Rev. Lett.*, 1160, 59 (1987)
- [83] Wu M.K., Ashburn J.R., Torng C.J., Hor P.H., Meng R.L., Gao L., Huang Z.J., Wang Y.Q., and Chu C.W., *Phys. Rev. Lett.*, 908, 58 (1987)

- [84] Yermakov A.E., Yurchikov E.E., and Barionov V.A., Fiz. Metal. Metalloved., 1184, 52 (1981)
- [85] Yermakov A.E., Barionov V.A., and Yurchikov E.E., Fiz. Metal. Metalloved., 935, 54 (1982)
- [86] Yoshimura M., Sung T.-H., Nakagawa Z., and Nakamura T., Jpn. J. Appl. Phys., L1877, 27 (1988)
- [87] Yoshimura M., Sung T.-H., Nakagawa Z., and Nakamura T., J. Mater. Sci. Lett., 687, 8 (1989)
- [88] Zandbergen H.W., Groen P., Van Tendeloo G., Van Landuyt J., and Amelinckx S., Solid State Comm., 397, 66 (1988)
- [89] Zeng R.J., Cable M., and Harris E.A., Supercond. Sci. Technol., 47, 2 (1989)
- [90] Zheng H. and Mackenzie J.D., Phys. Rev. B, 7166, 38 (1988)
- [91] Zheng H., Xu R., and Mackenzie J.D., J. Mater. Res., 911, 4 (1989)
- [92] Zhiyi L. and Persson M., Supercond. Sci. Technol., 198, 1 (1988)
- [93] Ziman J.M., "Principles of the Theory of Solids", Cambridge, New York, 1964, p. 242